

LANGLEY RESEARCH CENTER
3 1176 00520 4111

~~CONFIDENTIAL~~

copy
RM A52E06

6



RESEARCH MEMORANDUM

THE EFFECT OF AN OPERATING PROPELLER ON THE AERODYNAMIC
CHARACTERISTICS AT HIGH SUBSONIC SPEEDS OF A MODEL
OF A VERTICAL-RISING AIRPLANE HAVING AN UNSWEPT
WING OF ASPECT RATIO 3

By Fred B. Sutton and Donald A. Buell

Ames Aeronautical Laboratory
Moffett Field, Calif.

CLASSIFICATION CHANGED

To. UNCLASSIFIED

Naca Re. Abs & Effectue
By authority of RN-120 Date 9-13-57
NA 10-9-37

CLASSIFIED DOCUMENT

This material contains information affecting the National Defense of the United States within the meaning
of the espionage laws, Title 18, U.S.C., Secs. 770 and 771, the transmission or revelation of which in any
manner to an unauthorized person is prohibited by law.

NATIONAL ADVISORY COMMITTEE
FOR AERONAUTICS

WASHINGTON

November 15, 1954

~~CONFIDENTIAL~~

~~CONFIDENTIAL~~

NATIONAL ADVISORY COMMITTEE FOR AERONAUTICS

RESEARCH MEMORANDUM

THE EFFECT OF AN OPERATING PROPELLER ON THE AERODYNAMIC
CHARACTERISTICS AT HIGH SUBSONIC SPEEDS OF A MODEL
OF A VERTICAL-RISING AIRPLANE HAVING AN UNSWEPT
WING OF ASPECT RATIO 3

By Fred B. Sutton and Donald A. Buell

SUMMARY

An investigation was conducted in the Ames 12-foot pressure wind tunnel to determine the effect of an operating propeller on the aerodynamic characteristics of a model of a vertical-rising airplane having an unswept wing with an aspect ratio of 3. Wind-tunnel tests were conducted through a range of power coefficients at angles of attack up to 16° and at Mach numbers from 0.50 to 0.92. The Reynolds number was constant at 1.7 million.

Lift, longitudinal force, pitch, and roll characteristics, determined with and without power, are presented for the complete model and for various combinations of model components. Results of an investigation to determine the characteristics of the dual-rotating propeller used on the model are given also.

INTRODUCTION

The large thrust available with turbine-propeller propulsion systems has made possible the construction of fighter-type airplanes capable of vertical take-off and relatively high subsonic forward speeds. The investigation discussed herein was made of a model of such an airplane. The airplane configuration was aerodynamically conventional with the exception of an interdigitated tail on which all the movable control surfaces were located. Longitudinal, lateral, and directional control were achieved by appropriate combinations of movements of these four control surfaces.

Tests were conducted through an angle-of-attack range at several power coefficients (including propeller windmilling) to determine the effect of the operating propeller on the lift, drag, and pitching-moment characteristics of the model. The effect of windmilling propellers on

~~CONFIDENTIAL~~

the effectiveness of the longitudinal and lateral control surfaces was also investigated. Data are presented in this report without analysis and they pertain only to model characteristics in near horizontal flight attitudes and at comparatively high speeds.

NOTATION

The results of the investigation are presented in the form of standard NACA coefficients of forces and moments and are referred to the conventional stability axes. The coefficients and symbols used are defined as follows:

C_L lift coefficient, $\frac{\text{lift}}{qS}$

C_l rolling-moment coefficient measured about the center of gravity, $\frac{\text{rolling moment}}{qbS}$

C_m pitching-moment coefficient measured about the center of gravity, $\frac{\text{pitching moment}}{q\bar{c}S}$

C_P power coefficient, $\frac{P}{\rho n^3 D^5}$

C_T thrust coefficient, $\frac{T}{\rho n^2 D^4}$

C_X longitudinal-force coefficient, $\frac{X}{qS}$

c_{ld} propeller-blade-section design lift coefficient

b wing span, ft

b' propeller-blade width, ft

c wing chord, ft

\bar{c} mean aerodynamic wing chord, $\frac{\int_0^{b/2} c^2 dy}{\int_0^{b/2} c dy}$, ft

C.G. center-of-gravity location
(See fig. 1.)

D propeller diameter, ft

h maximum thickness of propeller-blade section, ft

- J propeller advance-diameter ratio, $\frac{V}{nD}$
- M free-stream Mach number
- n propeller rotational speed, rps
- P model-motor shaft power, ft-lb/sec
- R propeller-tip radius, ft
- r propeller-blade-section radius, ft
- q free-stream dynamic pressure, $\frac{1}{2} \rho V^2$, lb/sq ft
- S wing area, sq ft
- T propeller thrust, lb
- V free-stream velocity, ft/sec
- X longitudinal force, parallel to stream and positive in a thrust direction, lb
- y lateral distance from plane of symmetry, ft
- α angle of attack, deg
- β propeller-blade angle, deg
- δ control-surface deflection with respect to a section of the fixed surface taken perpendicular to the hinge line of the movable surface, deg
- δ_a aileron deflection, positive when lift is decreased on the right tail surface and increased on the left tail surface. (The control surfaces were deflected differentially to the same angular magnitude.)
- δ_e elevator deflection, positive to increase lift on tail
- η propeller efficiency, $\frac{C_T J}{C_P}$
- ρ free-stream mass density of air, slugs/cu ft

MODEL AND APPARATUS

The investigation was conducted in the Ames 12-foot pressure wind tunnel using a 1/10-scale model of the Lockheed XFV-1 airplane supplied by the Lockheed Aircraft Corporation. The model had an unswept wing with an aspect ratio of 3.07 and a taper ratio of 0.327. The wing employed NACA 65A206 sections. The prototype-airplane contours were slightly modified at the base of the model fuselage to accommodate a sting-type model support. Figure 1 and table I present dimensions and details of the model and figure 2 shows the model mounted in the tunnel test section.

The six-blade dual-rotating propeller employed on the model had an activity factor per blade of 140 (defined as $A.F. = \frac{100,000}{16} \int_{0.5}^{1.0} b' \left(\frac{r}{R}\right)^3 d\left(\frac{r}{R}\right)$) and was designed by the Curtiss-Wright Corporation specifically for vertical-take-off airplanes. Figure 3 presents propeller plan-form and blade-form curves.

The model, including the propeller, was constructed of aluminum alloy with the exception of the fuselage air-intake ducts which were sealed off and faired with a lead alloy. Model control-surface deflections were simulated with interchangeable control surfaces machined to predetermined angles. The model-propeller blades could be adjusted manually to any desired angle. The surfaces of the wing, body, and tail were filled, painted, and polished smooth.

Model power was supplied by two water-cooled induction motors mounted in tandem in the model fuselage. Each motor developed a maximum of 36 horsepower at 12,000 revolutions per minute. A continuous speed control for the two motors was obtained by the use of a variable-frequency power supply common to both motors. Each component of the dual-rotating propeller was directly driven by one of the model motors. Propeller speed was measured by means of a tachometer on the front motor (rear propeller) used in conjunction with an electronic frequency-measuring device. It was assumed that both motors turned at the same speed.

A sting-type model-support system was used with a wire-resistance strain-gage balance of the flexure-pivot type enclosed in the model fuselage to measure lift, longitudinal force, side force, pitching moment, rolling moment, and yawing moment. Angle of attack was measured visually by means of a cathetometer.

TESTS AND PROCEDURES

Test Ranges

The characteristics of the model were investigated over a Mach number range of 0.50 to 0.92; Reynolds number was constant at 1.7 million. Several power conditions were investigated at various propeller-blade angles through an angle-of-attack range of -4° to $+8^{\circ}$ at each Mach number.

A summary of the power-on tests for several model configurations is presented in table II. The power coefficients could not be exactly duplicated for the different model configurations as the tunnel temperatures and model-motor efficiencies could not be accurately predetermined. The power-coefficient values presented in table II are the averages of the values measured through an angle-of-attack range.

Propeller Calibration

Propeller calibrations were made by testing the propeller in combination with the model fuselage less the pilot's cab (fig. 4). Forces were measured through Mach number, angle-of-attack, model power, and propeller-blade-angle ranges which included the test ranges of the power-on model investigation. The propeller thrust coefficient was determined from the following relation:

$$C_T = \frac{T}{\rho n^2 D^4} = \frac{J^2 S}{2D^2} C_{X_p}$$

where

$$C_{X_p} = C_{X_{\text{propeller operating}}} - C_{X_{\text{propeller off}}}$$

The shaft power of the model motors was determined by measuring the input power to the motors and applying corrections for the motor losses. Interference effects between the body and the propeller were neglected and the efficiencies presented are the propulsive efficiencies of the propeller-body combination.

CORRECTIONS

Tunnel-Wall Interference

Corrections for the induced effects of the tunnel walls resulting from lift on the model were made according to the methods of reference 1. The corrections added to the angle of attack and longitudinal-force coefficient were as follows:

$$\Delta\alpha = 0.2078 C_L$$

$$\Delta C_X = -0.00363 C_L^2$$

No corrections were made to the pitching-moment coefficients as calculations by the method of reference 1 indicated the corrections to be negligible.

The effects of wind-tunnel-wall constraint on the model-propeller slipstream were evaluated by the method of references 2 and 3. These effects were indicated to be negligible.

The effects of constriction of the flow by the tunnel walls were evaluated by the method of reference 4. The following table shows the magnitude of the corrections:

<u>Corrected Mach number</u>	<u>Uncorrected Mach number</u>	<u>$\frac{q_{corrected}}{q_{uncorrected}}$</u>
0.500	0.500	1.001
.700	.699	1.002
.800	.798	1.003
.850	.847	1.004
.900	.894	1.006
.920	.912	1.008

Sting Interference

In order to correct partially the longitudinal-force data for sting interference, the pressure was measured at the base of the model fuselage and the drag data were adjusted to correspond to a base pressure equal to the static pressure of the free stream.

RESULTS

Figures 5 through 10 show the characteristics of the dual-rotating propeller. Because of the small thrust available at Mach numbers of 0.90 and 0.92, only one power condition in addition to propeller wind-milling was investigated at these Mach numbers. The fairing of propeller-performance curves for these conditions (indicated by broken lines) is based on propeller-performance data obtained at lower Mach numbers. Figures 11 through 16 show the effect of power on the aerodynamic characteristics of the model fuselage. The effects of power on the aerodynamic characteristics of the complete model are shown in figures 17 through 22, and power effects on the aerodynamic characteristics of the model with the tail removed are presented in figure 23. Figure 24 shows longitudinal control-effectiveness data for several elevator deflections and one combination of elevator and aileron deflections. Roll characteristics of the model are presented in figure 25 for one aileron deflection and for a combination of aileron and elevator deflections. Figure 26 presents aerodynamic characteristics for several combinations of model components with the propeller removed, and figure 27 shows the aerodynamic characteristics for the body alone, the body and cab, and the body and tail.

Ames Aeronautical Laboratory
National Advisory Committee for Aeronautics
Moffett Field, Calif., May 6, 1952

REFERENCES

1. Silverstein, Abe, and White, James H.: Wind-Tunnel Interference with Particular Reference to Off-Center Positions of the Wing and to the Downwash at the Tail. NACA Rep. 547, 1935.
2. Glauert, H.: The Elements of Aerofoil and Airscrew Theory. American ed., The Macmillan Company, N.Y., 1943, pp. 222-226.
3. Young, A. D.: Note on the Application of the Linear Perturbation Theory to Determine the Effect of Compressibility on the Wind Tunnel Constraint on a Propeller. R.A.E. TN No. Aero. 1539, Nov. 1944.
4. Herriot, John G.: Blockage Corrections for Three-Dimensional-Flow Closed-Throat Wind Tunnels, with Consideration of the Effect of Compressibility. NACA Rep. 995, 1950. (Formerly NACA RM A7B28)

TABLE I.- GEOMETRIC CHARACTERISTICS OF THE MODEL

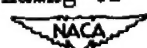
Wing		
Span, in.	33.00	
Root chord, in.	16.20	
Tip chord, in.	5.30	
Mean aerodynamic chord, in.	11.65	
Aspect ratio	3.07	
Taper ratio	0.327	
Area, sq ft	2.46	
Dihedral of wing reference plane through 40-percent chord, deg	-5.0	
Incidence, root and tip, deg	1.0	
Length, wing-tip armament pods, in.	16.80	
Diameter, wing-tip armament pods, in.	1.80	
Airfoil section, root and tip	NACA 65A206	
Tail		
Span, in.	14.70	
Root chord, in.	8.50	
Tip chord, in.	3.20	
Mean aerodynamic chord, in.	6.25	
Aspect ratio	3.55	
Taper ratio	0.376	
Total area, 4 surfaces, sq ft	1.69	
Total area, 4 fixed surfaces, sq ft	1.36	
Total area, 4 movable surfaces, sq ft	0.32	
Incidence (angle in vertical plane) between fuselage reference line and intersection of all chord planes, deg	-4.0	
Sweepback angle, quarter chord, deg	30.0	
Airfoil section, root and tip	NACA 65A007	



TABLE II.- SUMMARY OF THE MODEL POWER-ON TESTS

Mach no.	Tunnel density altitude, ft	Propeller blade angle, deg at 0.75 r/R sta.	Complete model configuration			Tail-off model configuration			Simulated yaw configuration		
			C _{pav}	Equivalent full-scale hp ¹	Fig. no.	C _{pav}	Equivalent full-scale hp ¹	Fig. no.	C _{pav}	Equivalent full-scale hp ¹	Fig. no.
.50	22,100	50	0.84	2950	17(a)	--	--	--	--	--	--
.50	22,100	50	.56	1650	17(a)	--	--	--	--	--	--
.50	22,100	55	1.25	2700	17(b)	1.27	2700	23(a)	1.13	2300	25
.50	22,100	55	.94	1650	17(b)	1.02	1850	23(a)	--	--	--
.70	31,500	50	.64	4100	18(a)	--	--	--	--	--	--
.70	31,500	55	.86	3100	18(b)	.89	3150	23(b)	.81	2950	25
.70	31,500	55	.79	2750	18(b)	.88	3050	23(b)	--	--	--
.70	31,500	60	1.32	2750	18(c)	--	--	--	--	--	--
.70	31,500	60	1.13	2150	18(c)	--	--	--	--	--	--
.80	35,100	50	.42	3150	19(a)	--	--	--	--	--	--
.80	35,100	55	.76	3350	19(b)	.81	3650	23(c)	.69	3200	25
.80	35,100	55	.66	2800	19(b)	.73	3150	23(c)	--	--	--
.85	36,500	55	.78	3700	20(a)	.73	3650	23(d)	.65	3450	25
.85	36,500	60	1.09	3150	20(b)	--	--	--	--	--	--
.85	36,500	60	.97	2700	20(b)	--	--	--	--	--	--
.90	37,800	55	--	--	--	.74	4250	23(e)	.63	4050	25
.90	37,800	60	1.03	3300	21	--	--	--	--	--	--
.92	38,200	55	--	--	--	.69	4150	23(f)	.53	3500	25
.92	38,200	60	.98	3300	22	--	--	--	--	--	--

¹Equivalent full-scale horsepower was calculated for assumed airplane altitudes corresponding to the tunnel-density altitudes and a model scale of 1/10.



10

NACA RM A52E06

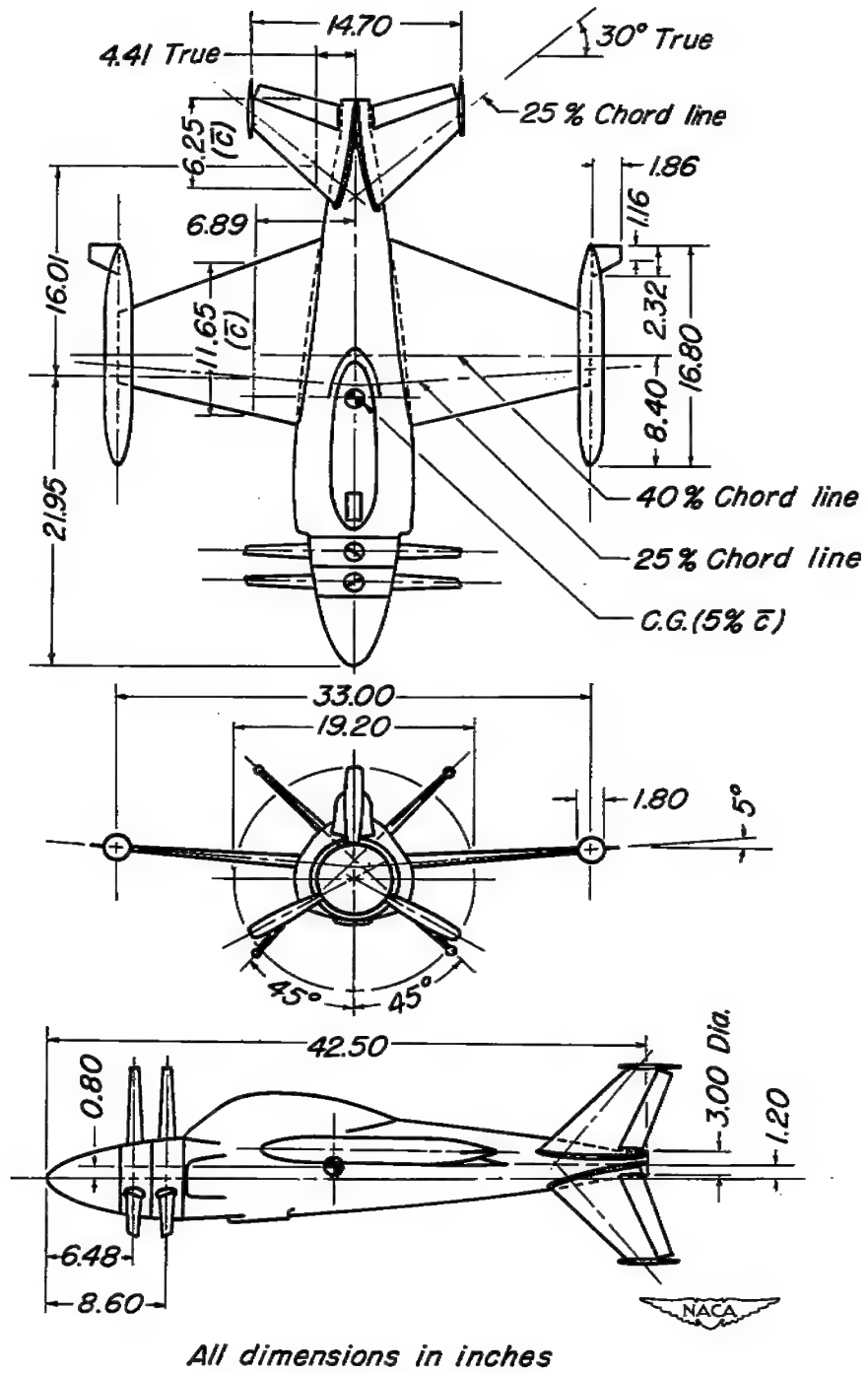


Figure 1.— Three-view drawing of the model.

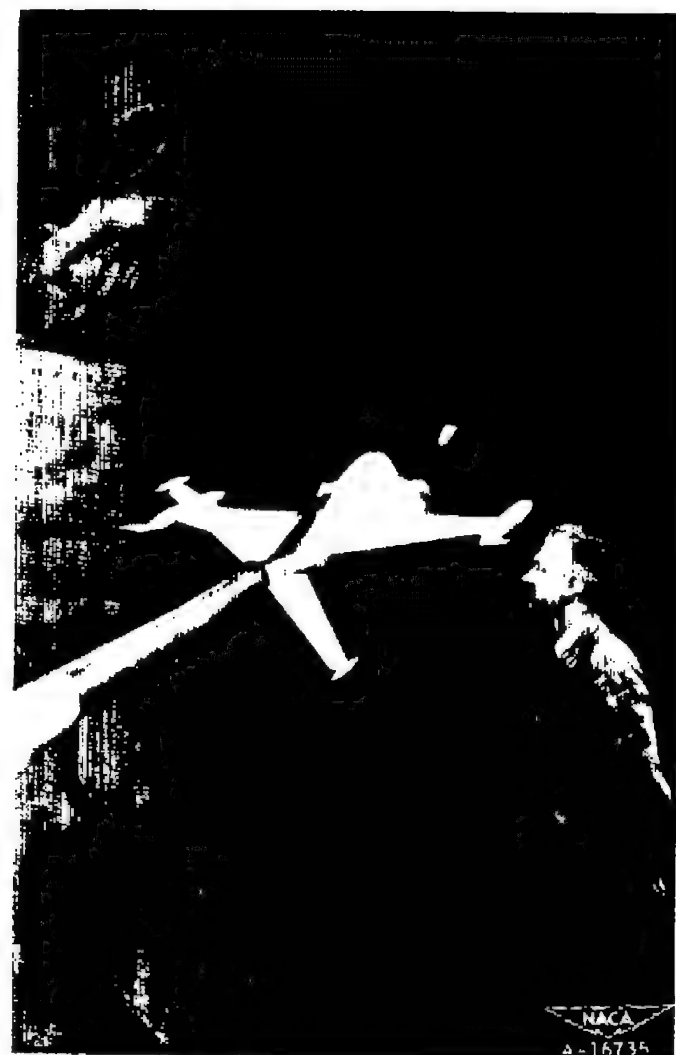
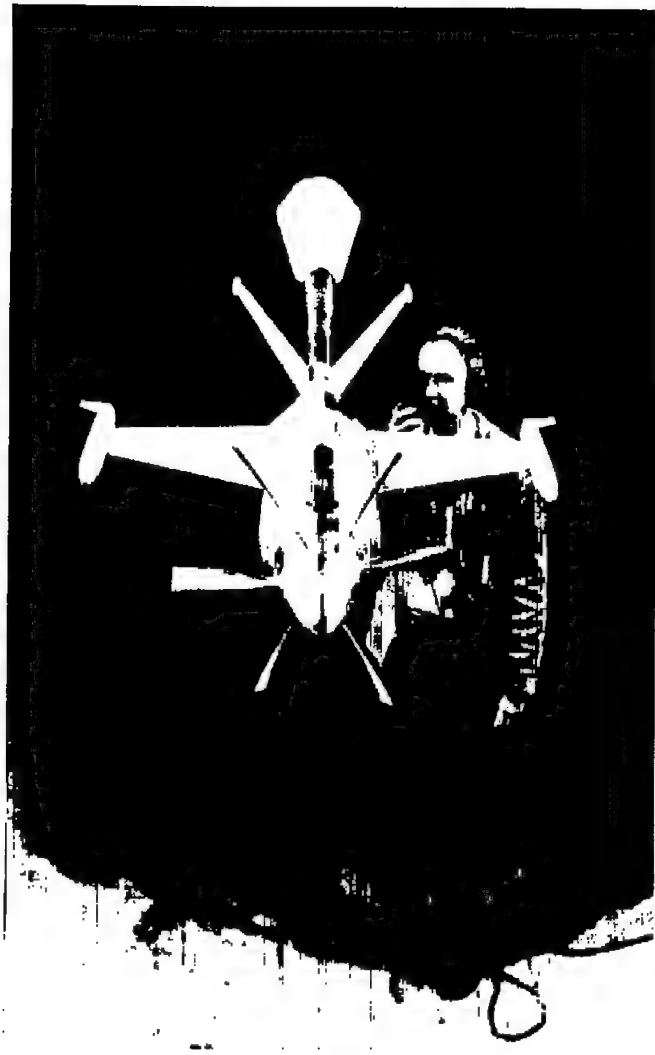


Figure 2.- The model in the Ames 12-foot pressure wind tunnel.

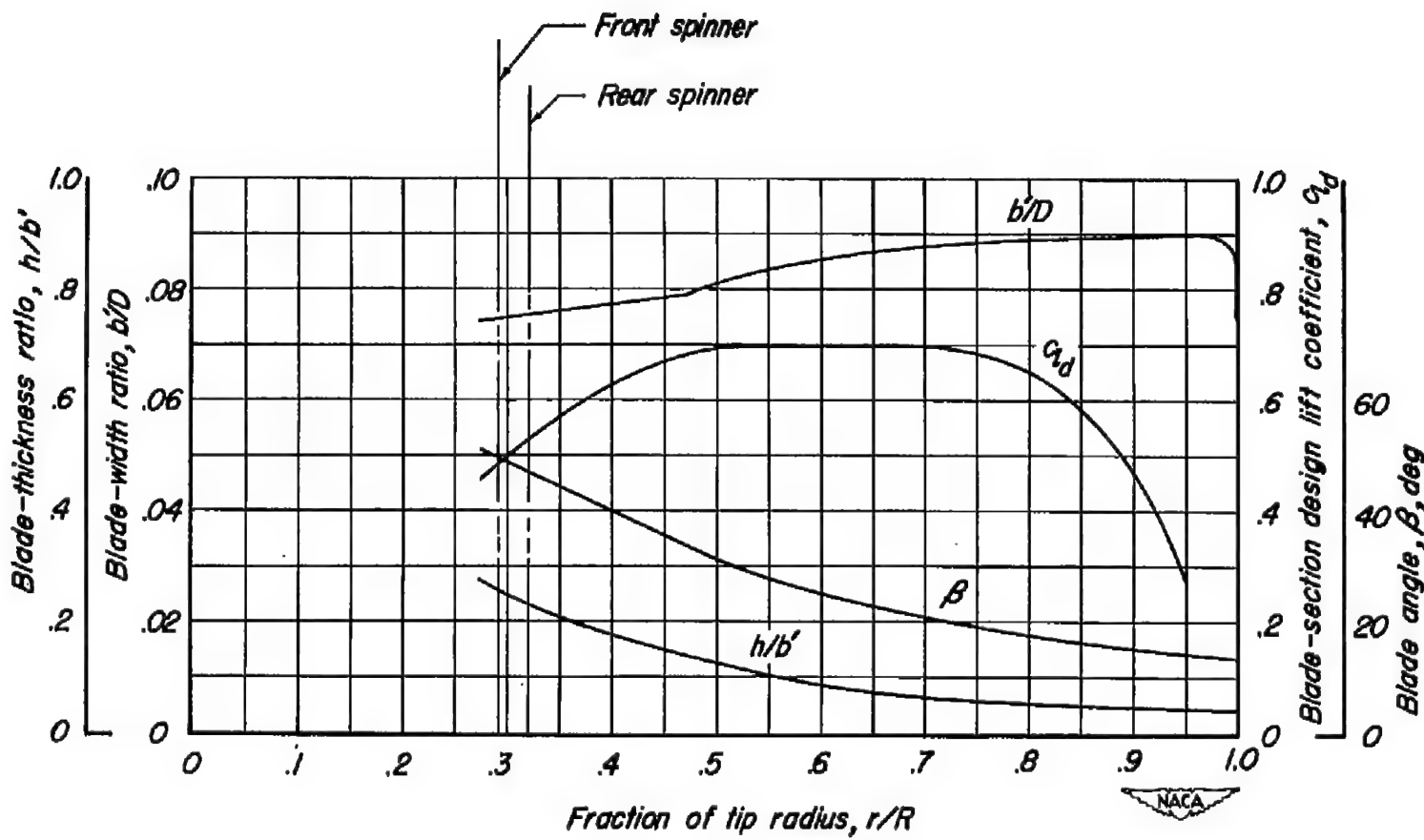


Figure 3.—Plan-form and blade-form curves for the dual-rotating propeller.

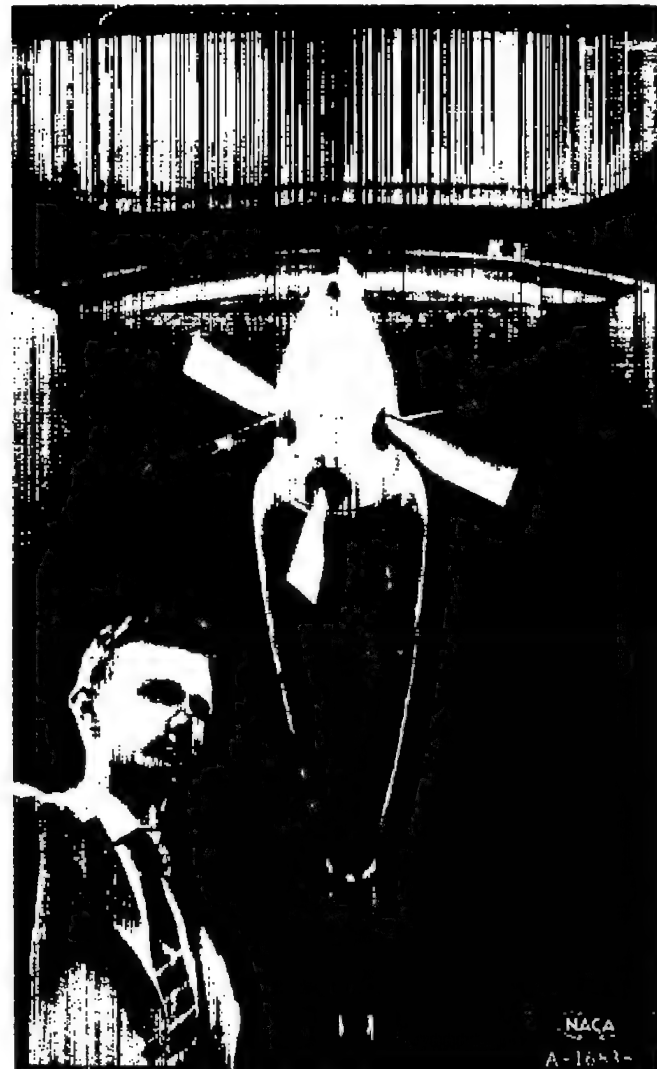


Figure 4.- The model propeller in the Ames 12-foot pressure wind tunnel.

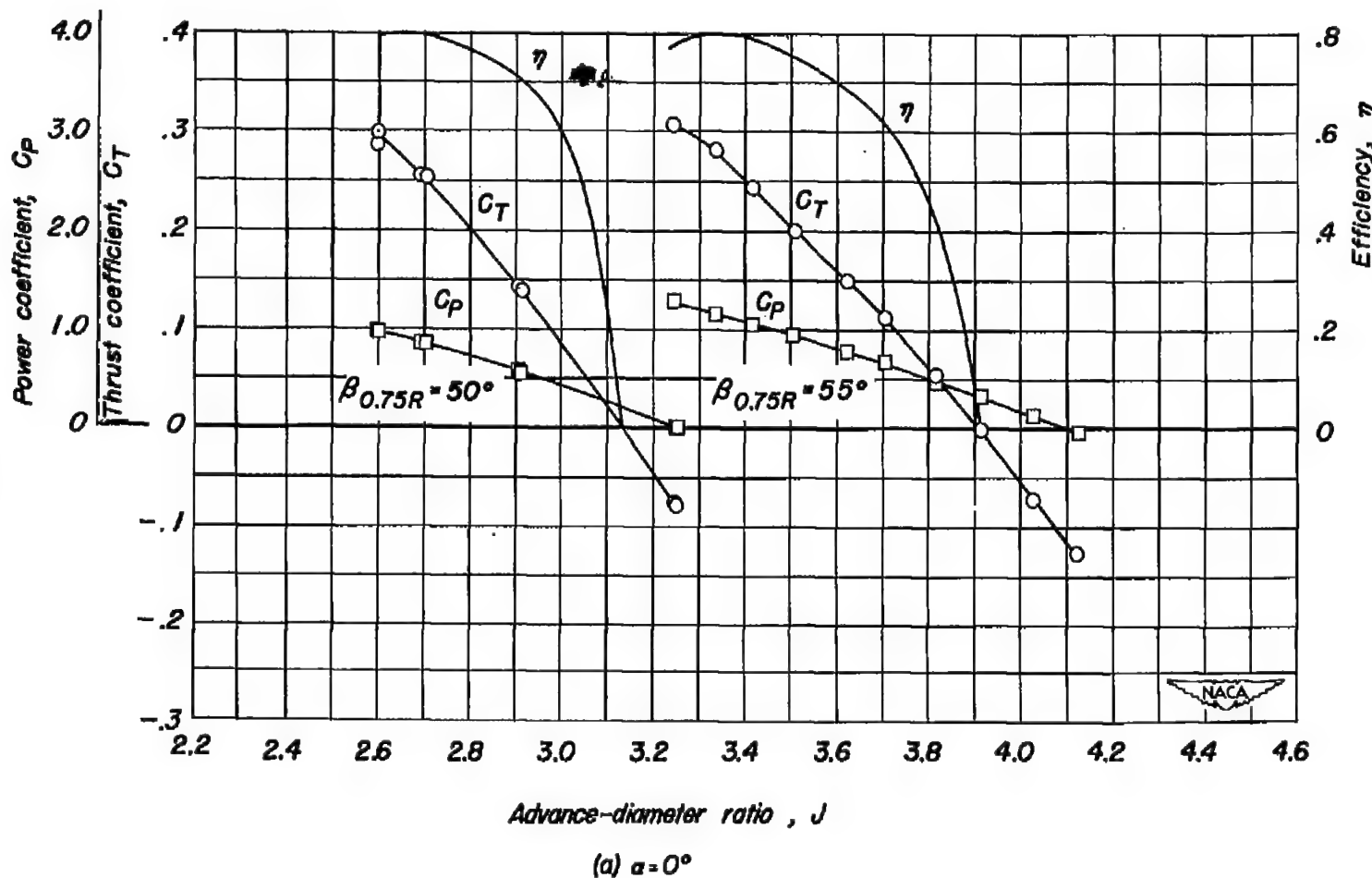


Figure 5.—Characteristics of the dual-rotating propeller; $M=0.50$

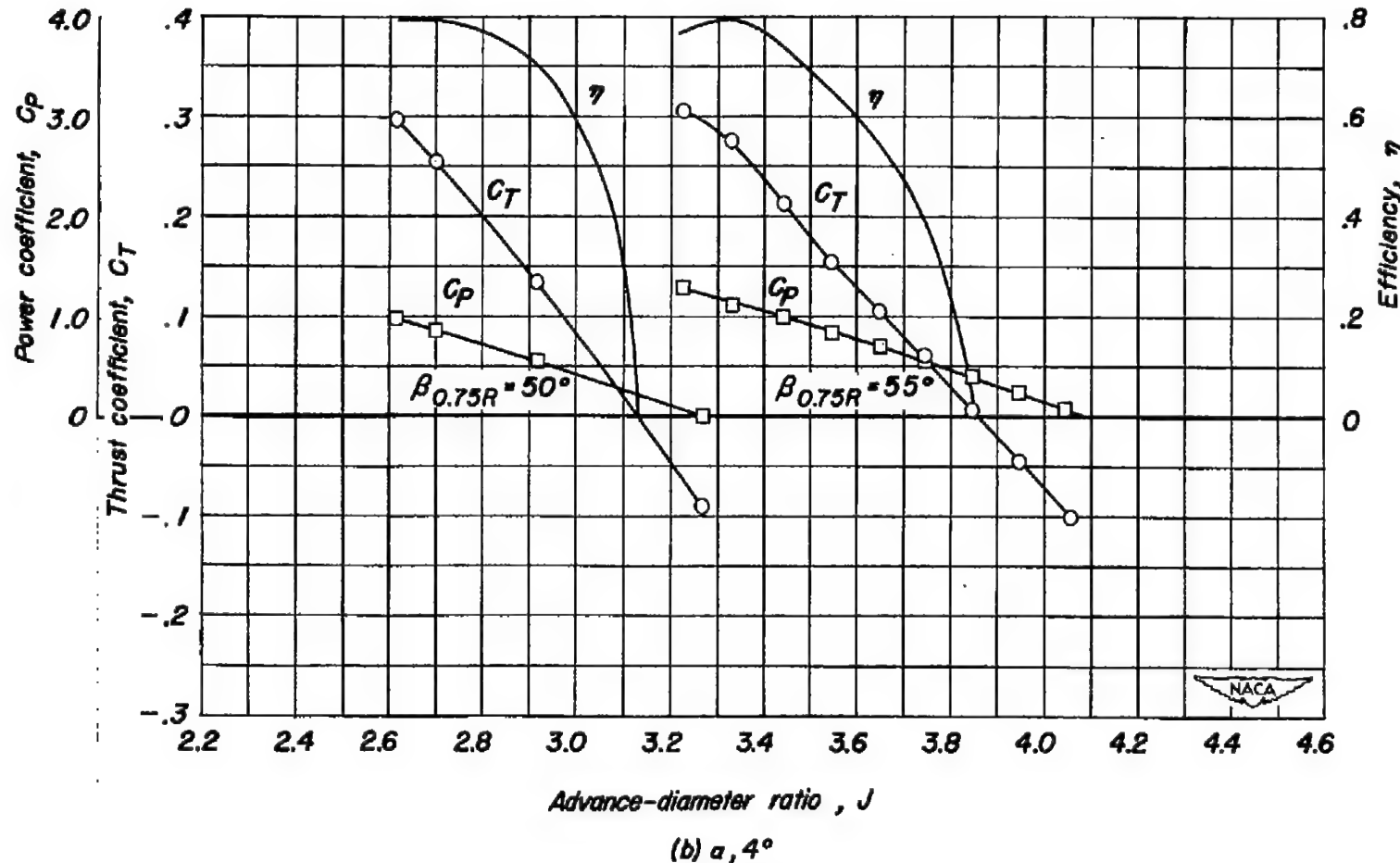
(b) $\alpha, 4^\circ$

Figure 5.- Continued.

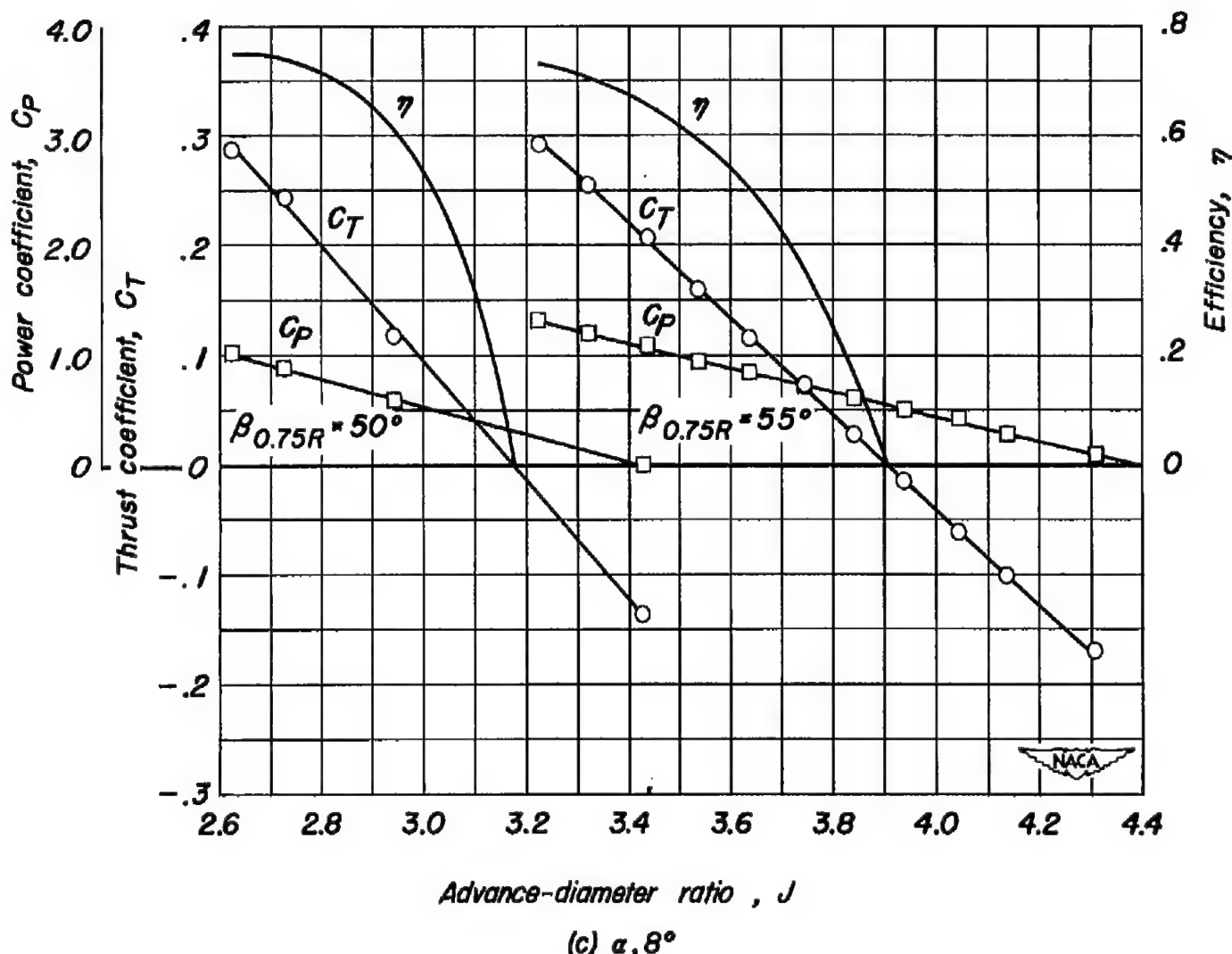


Figure 5.- Continued.

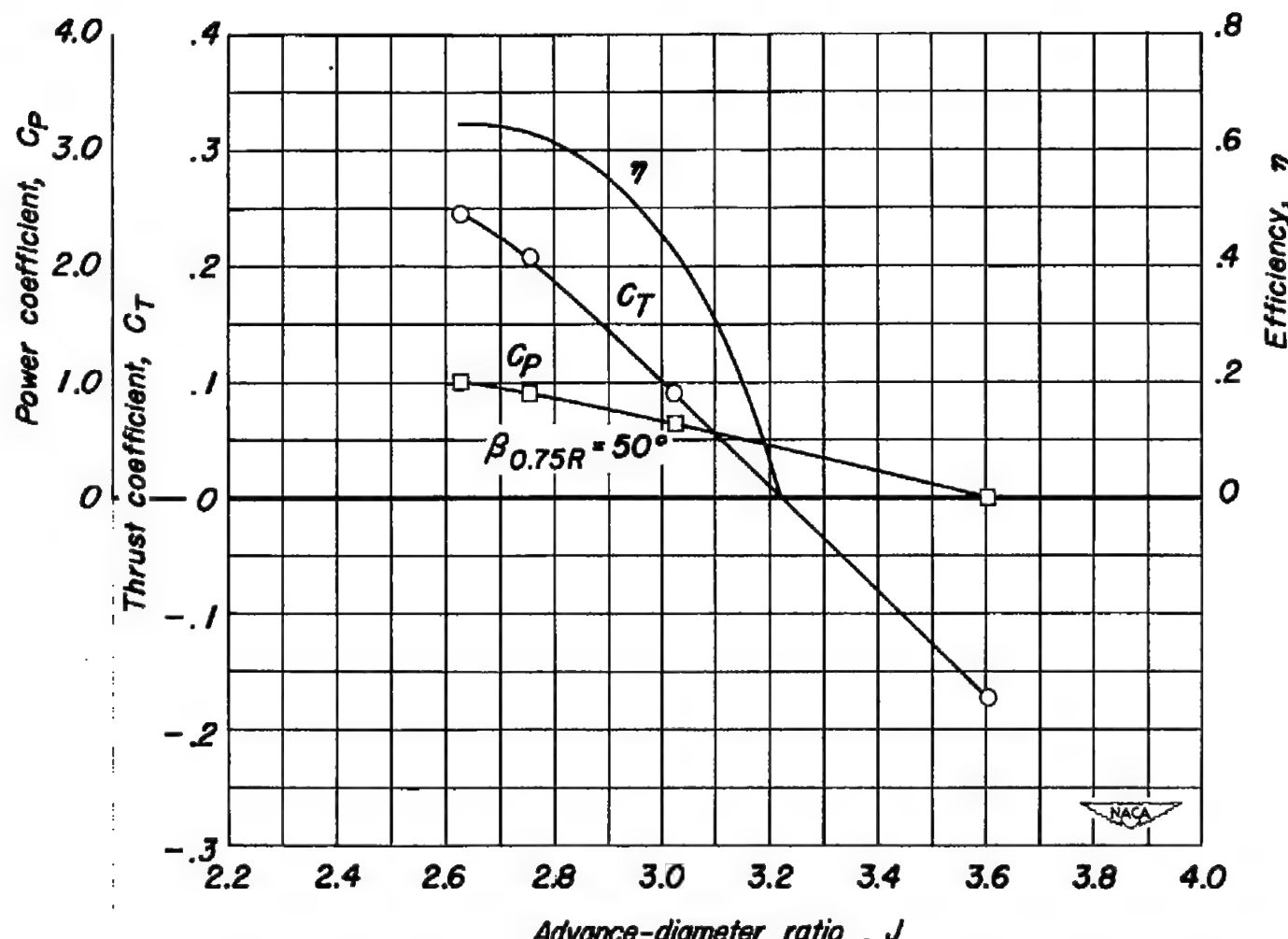
(d) $\alpha, 12^\circ$

Figure 5.- Continued:

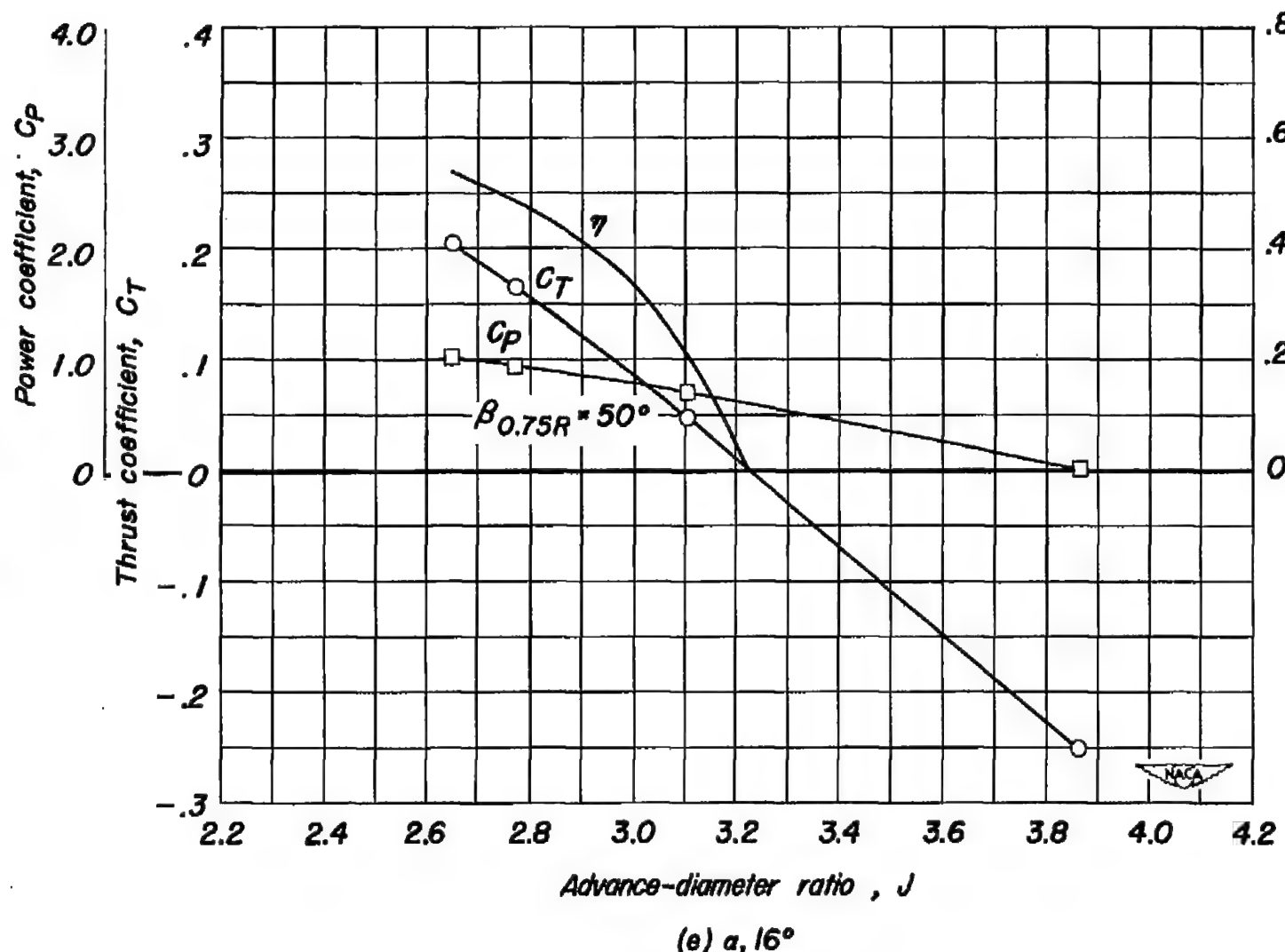


Figure 5.- Concluded.

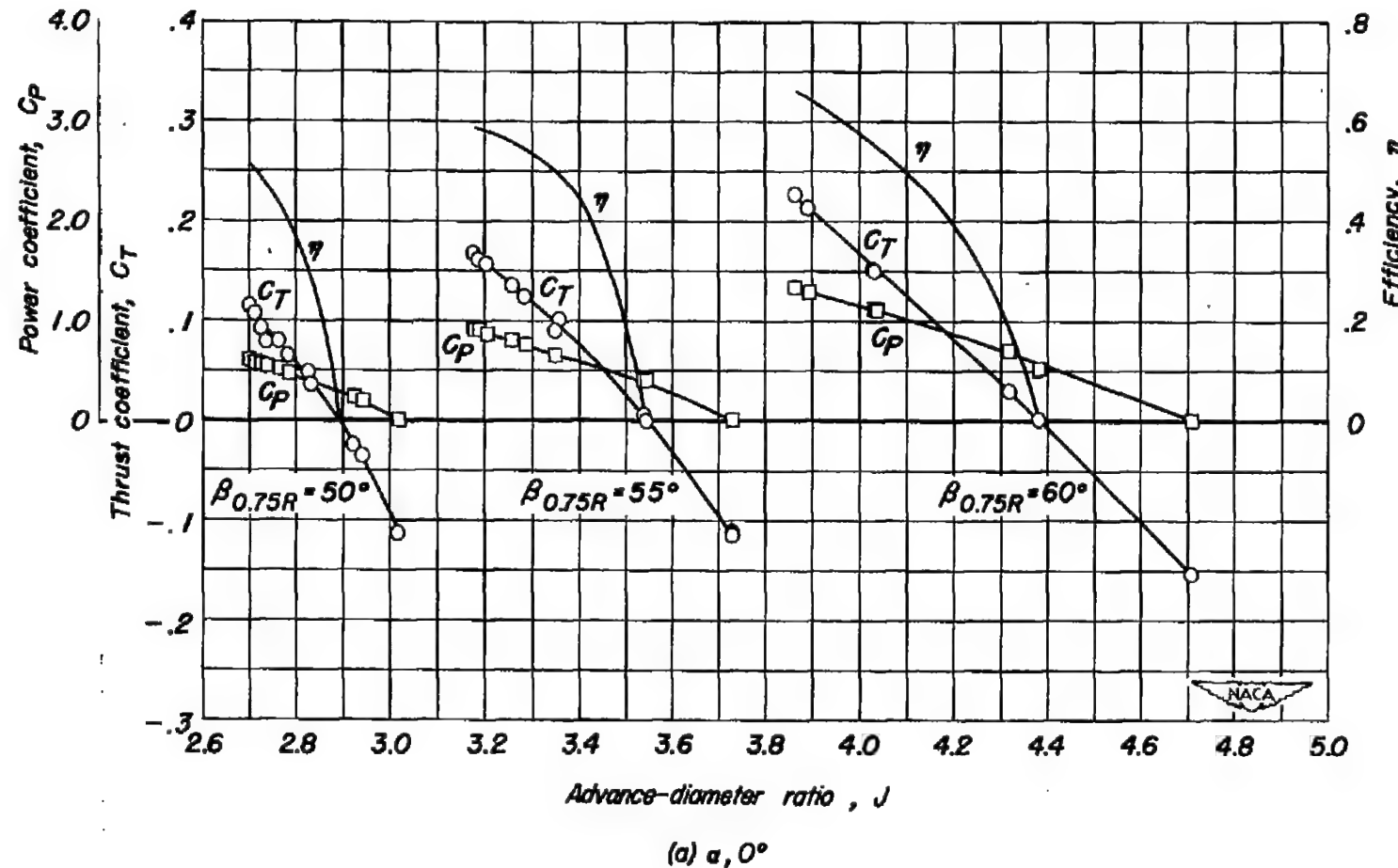


Figure 6.—Characteristics of the dual-rotating propeller. $M, 0.70$.

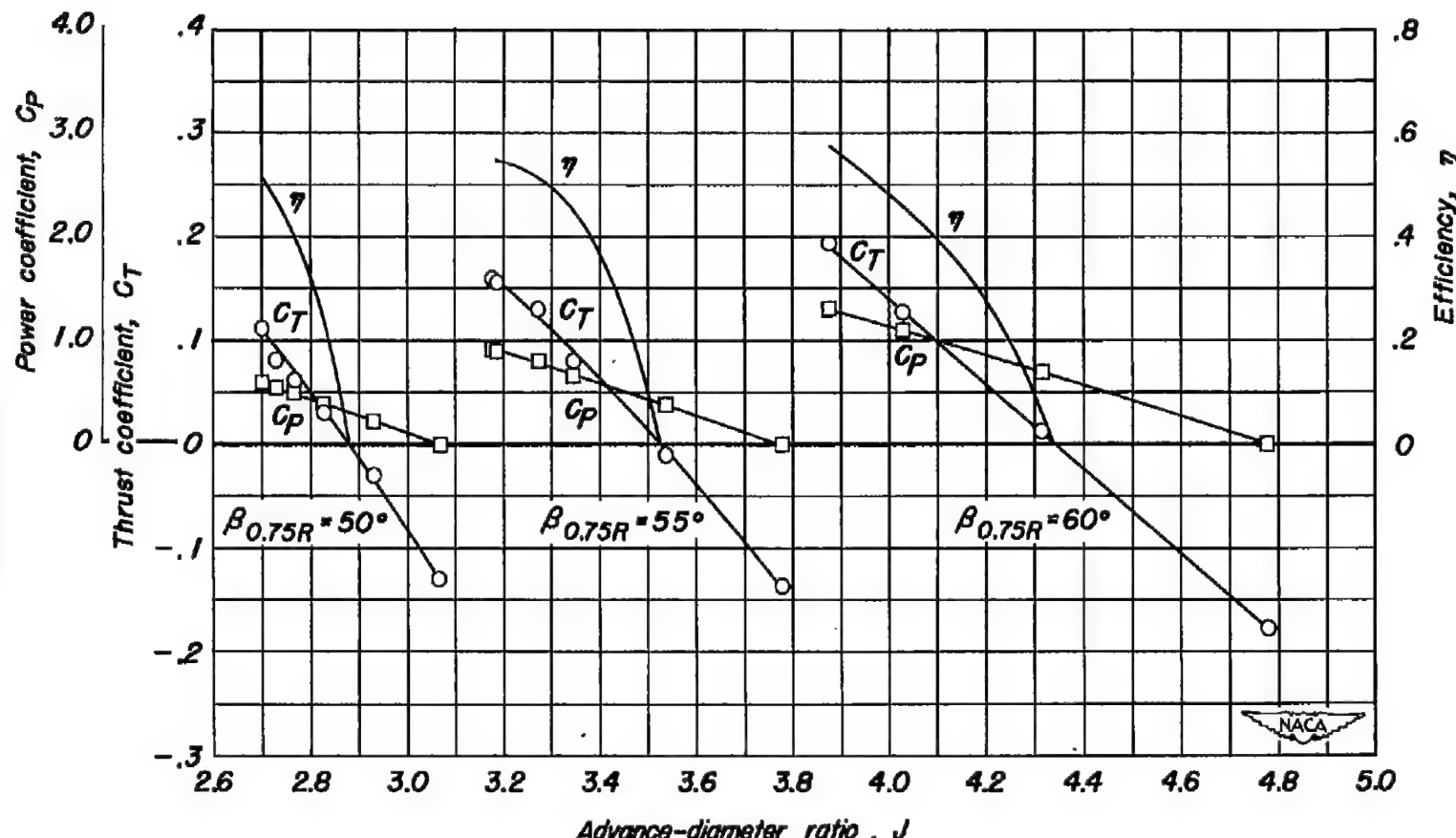


Figure 6.- Continued.

(b) $a, 4^\circ$

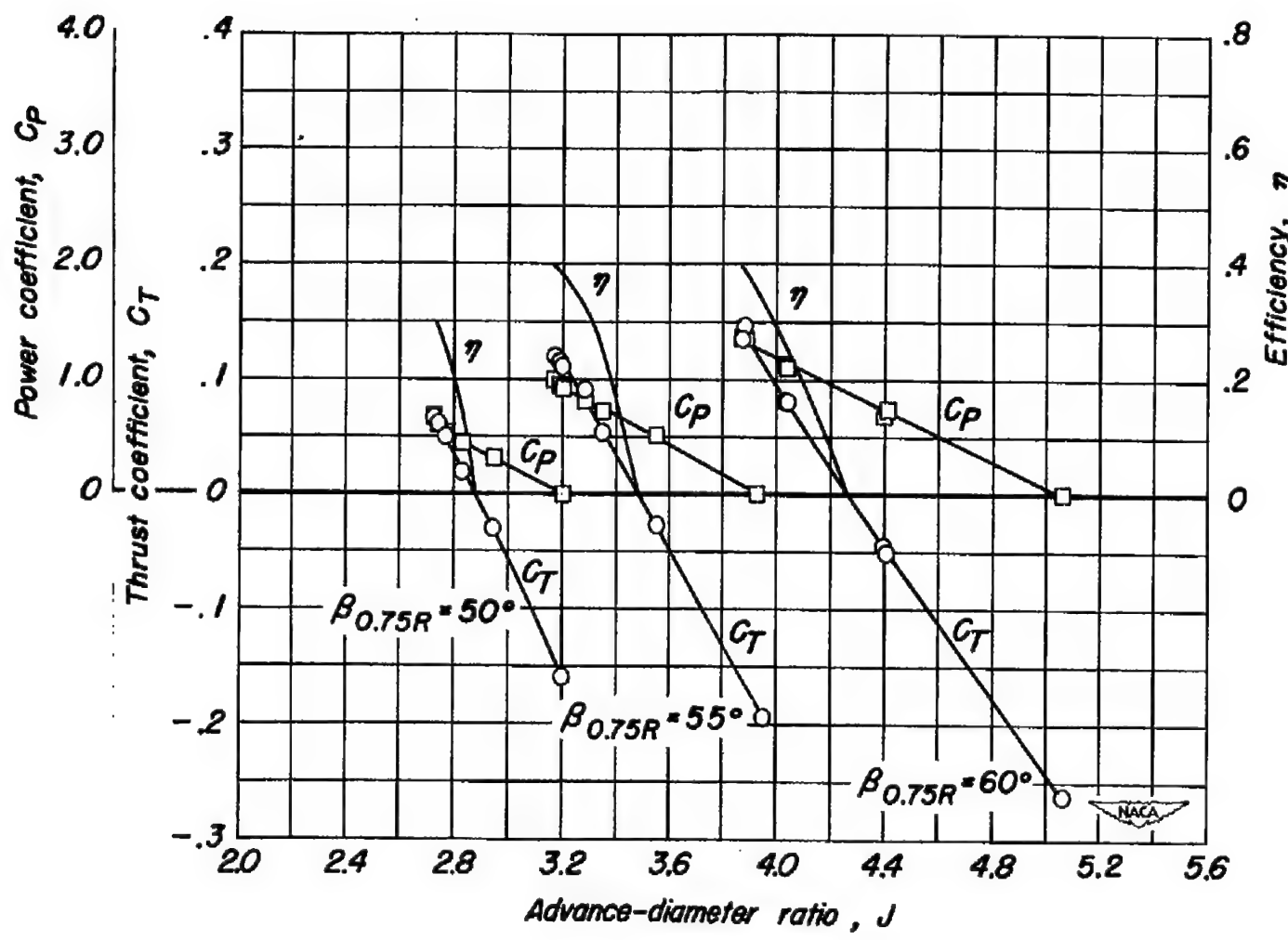
(c) $\alpha, 8^\circ$

Figure 6.- Continued.

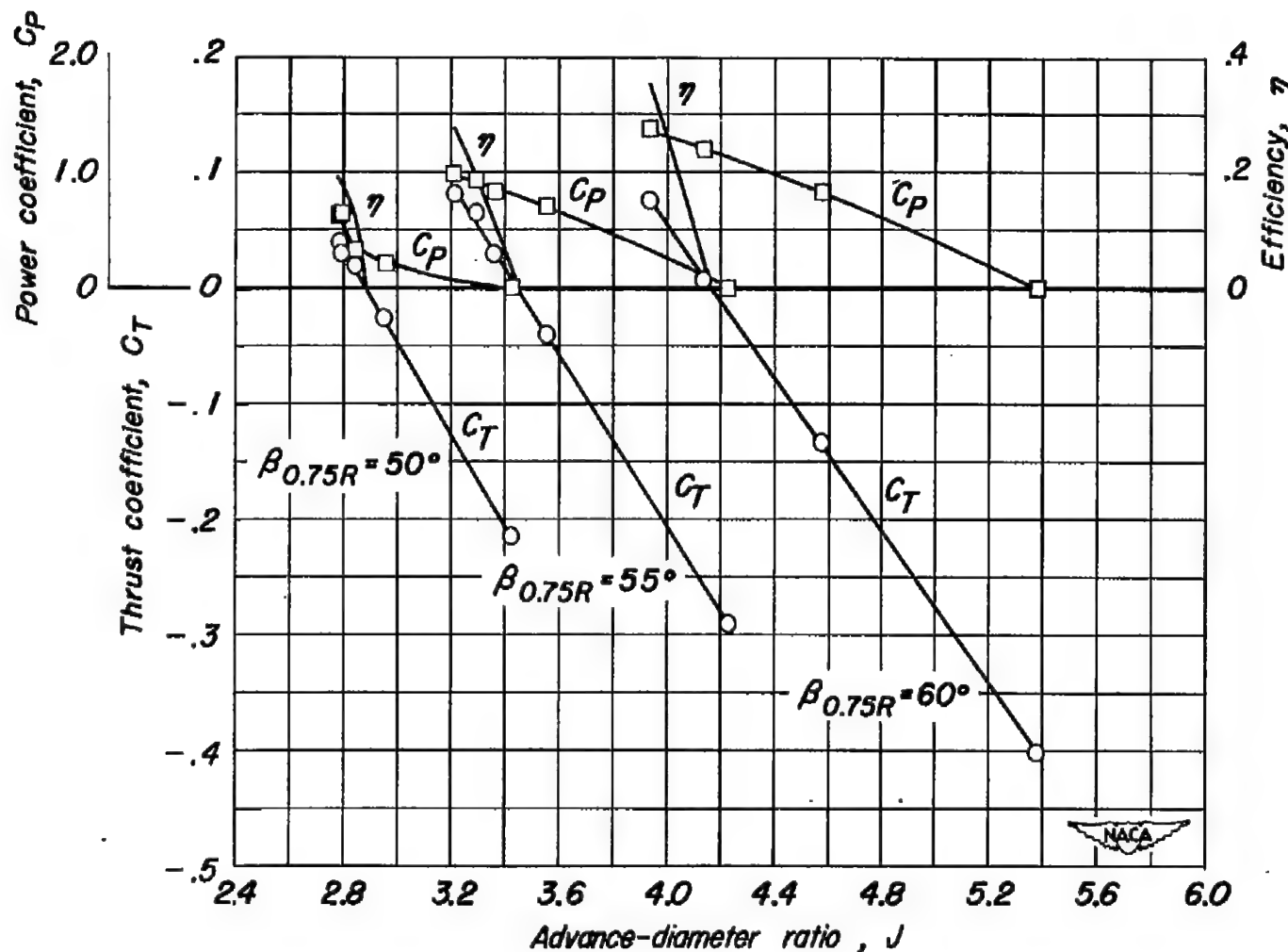
(d) $\alpha, 12^\circ$

Figure 6.- Concluded.

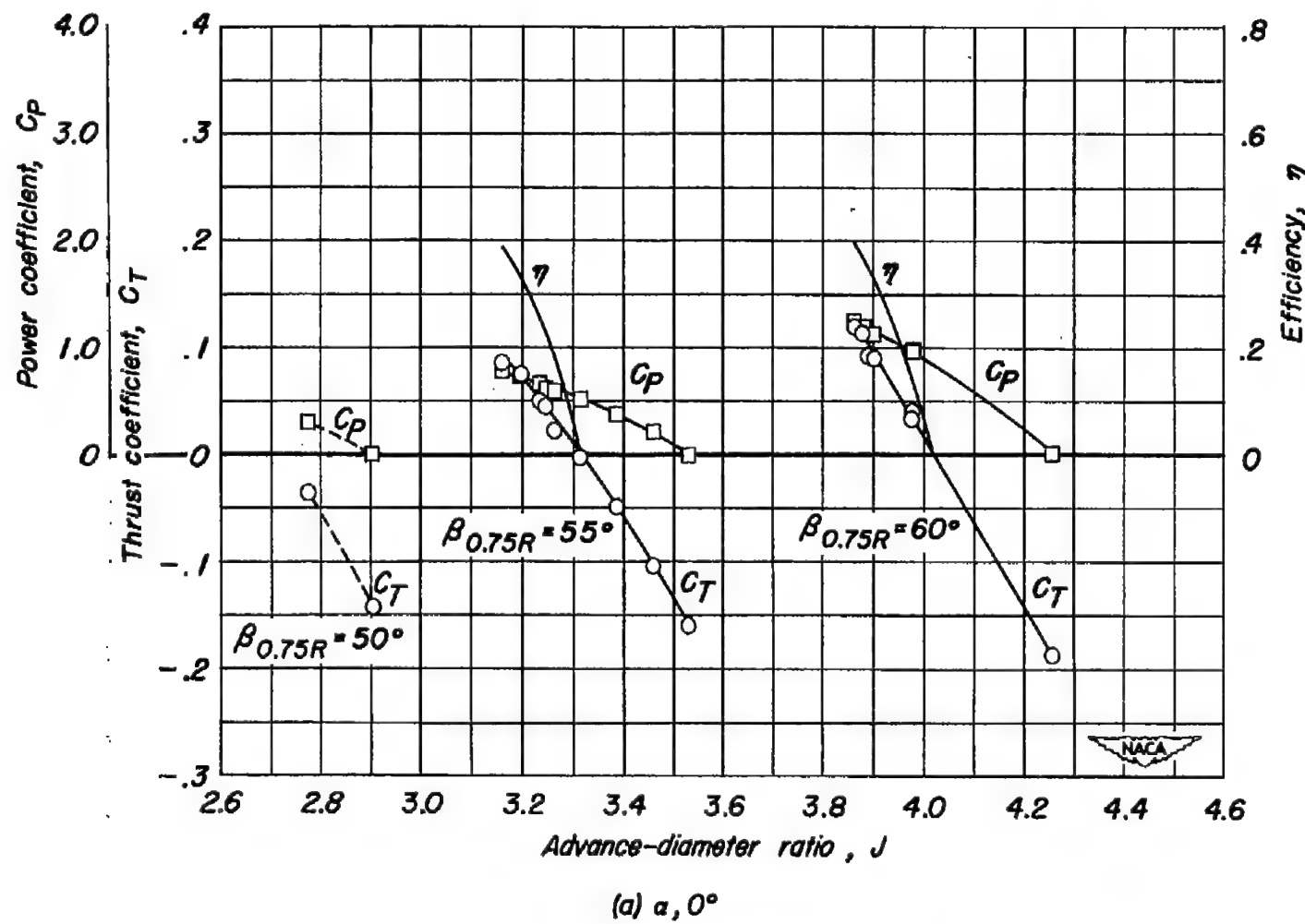


Figure 7.—Characteristics of the dual-rotating propeller. $M, 0.80$.

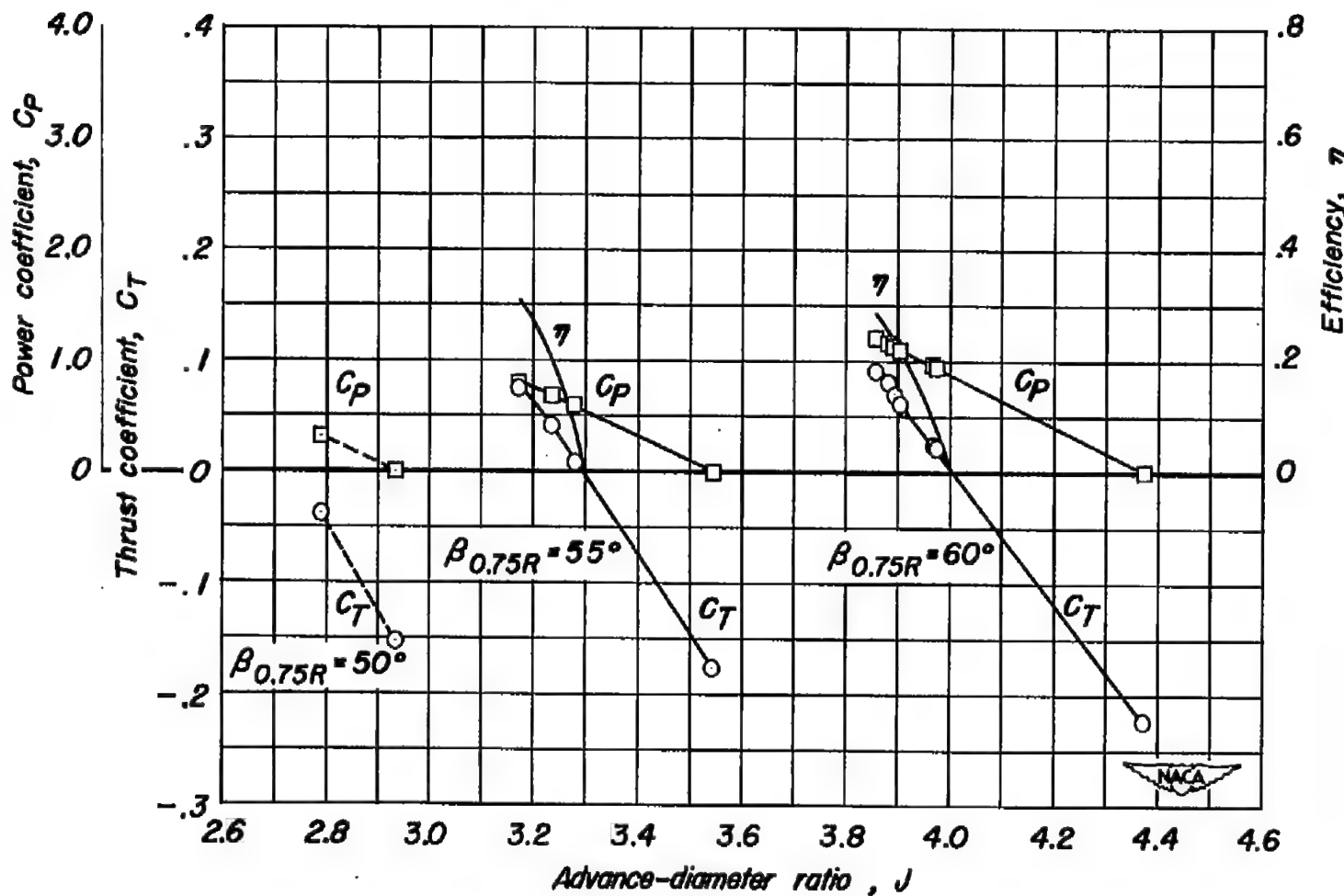
(b) $\alpha, 4^\circ$

Figure 7.- Continued.

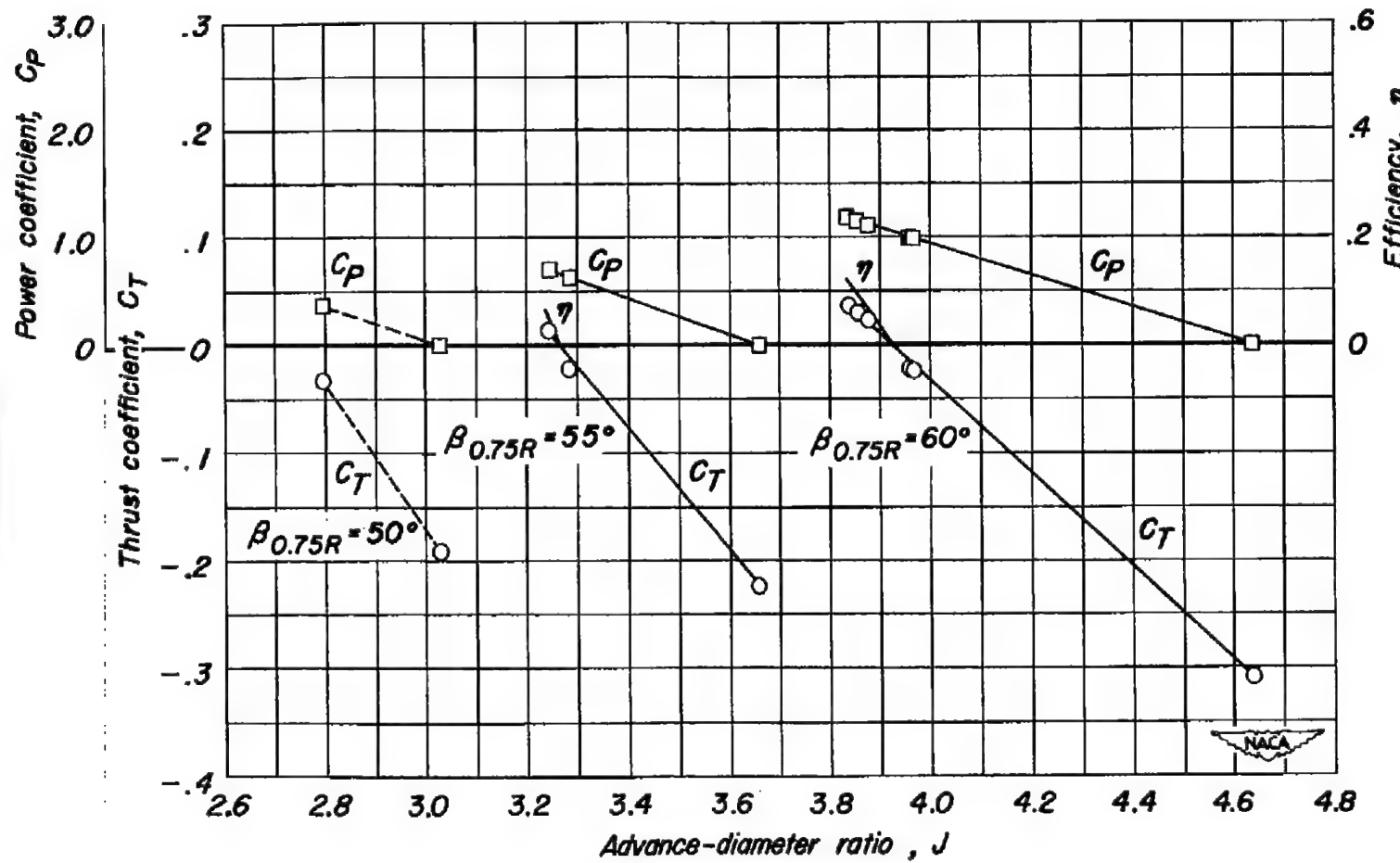
(c) $\alpha, 8^\circ$

Figure 7.- Concluded.

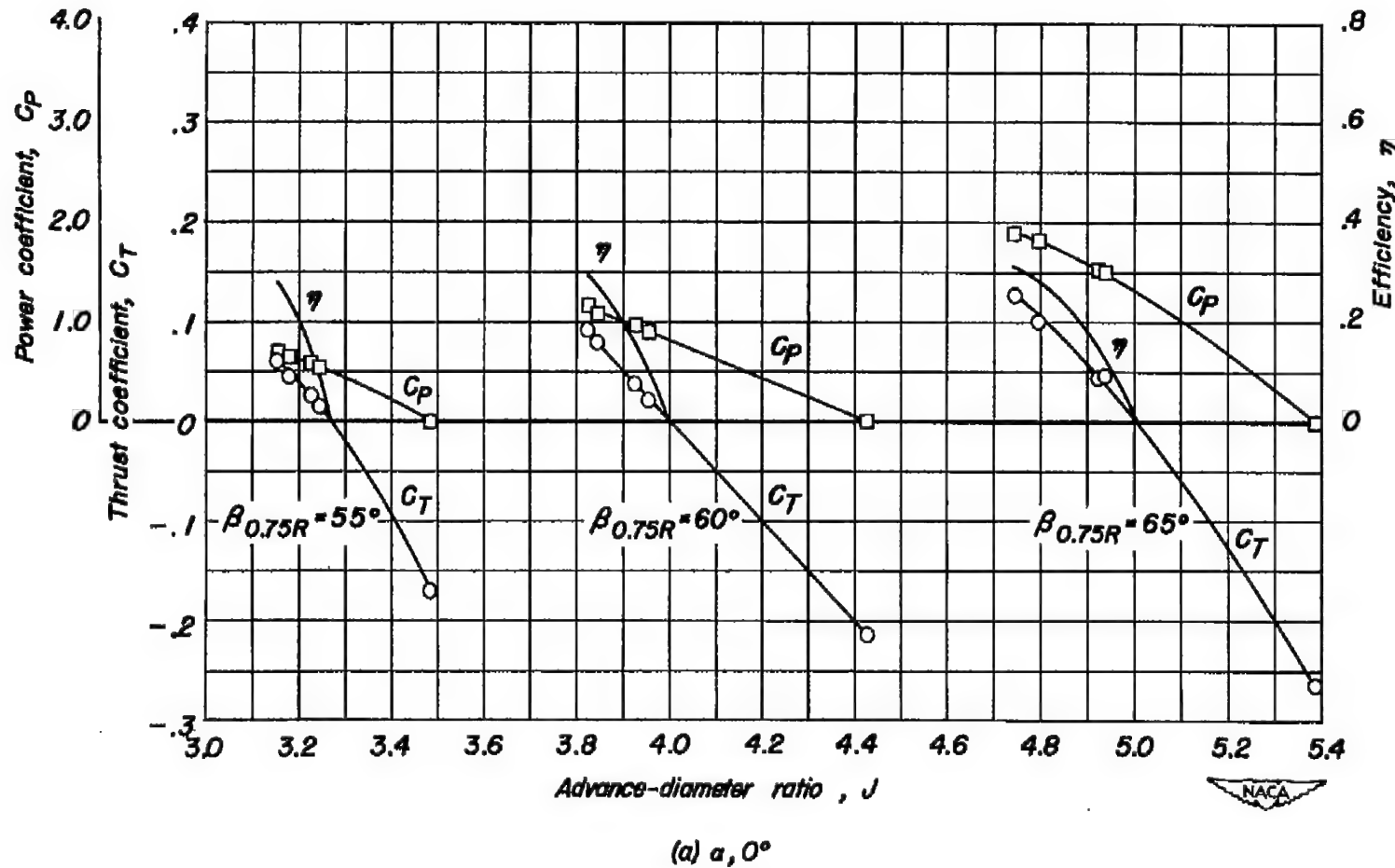


Figure 8.—Characteristics of the dual-rotating propeller. $M, 0.85$.

(a) $\alpha, 0^\circ$

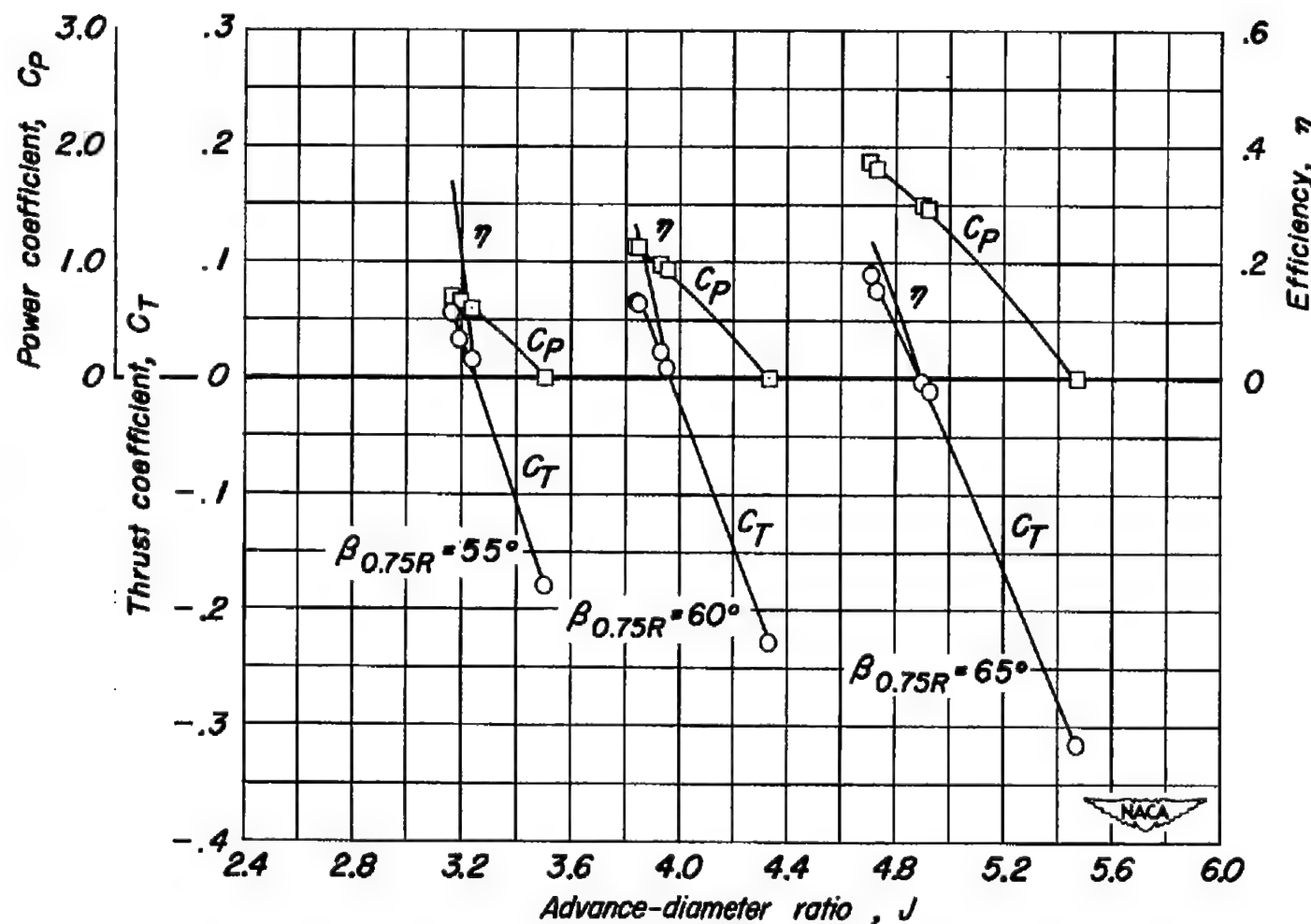
(b) $a, 4^\circ$

Figure 8.- Continued.

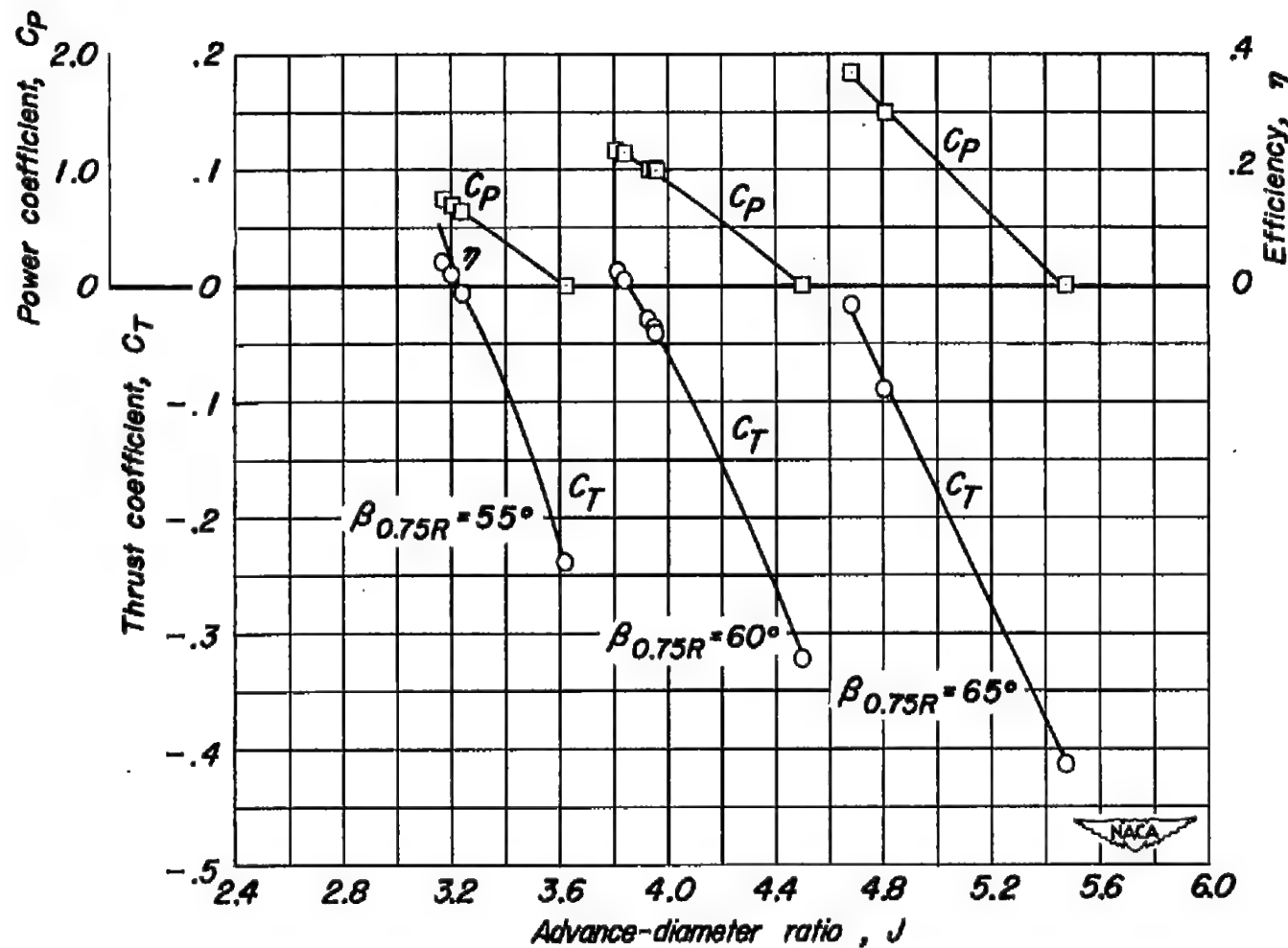
(c) $\alpha, 8^\circ$

Figure 8.- Concluded.

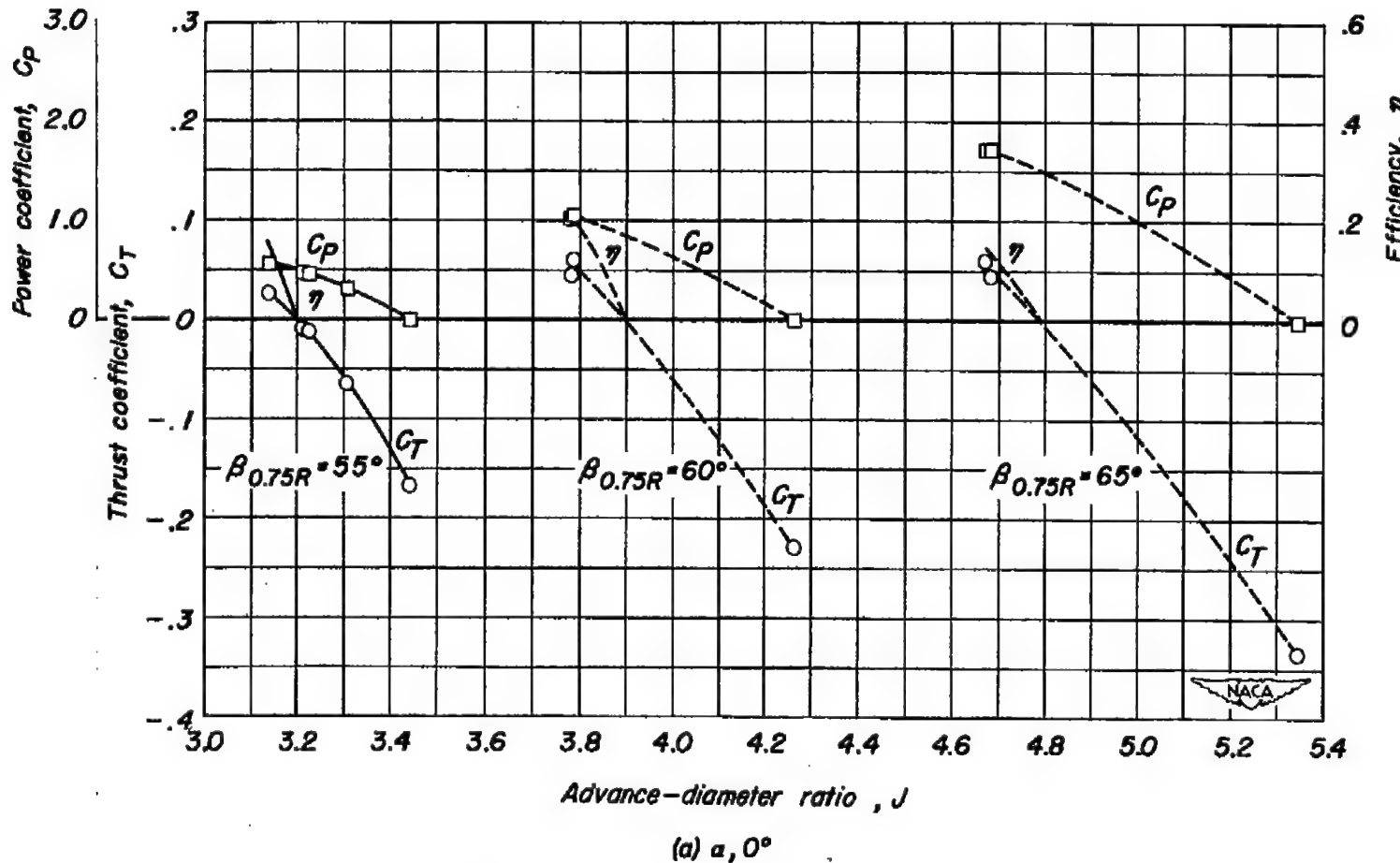


Figure 9.—Characteristics of the dual-rotating propeller. $M, 0.90$.

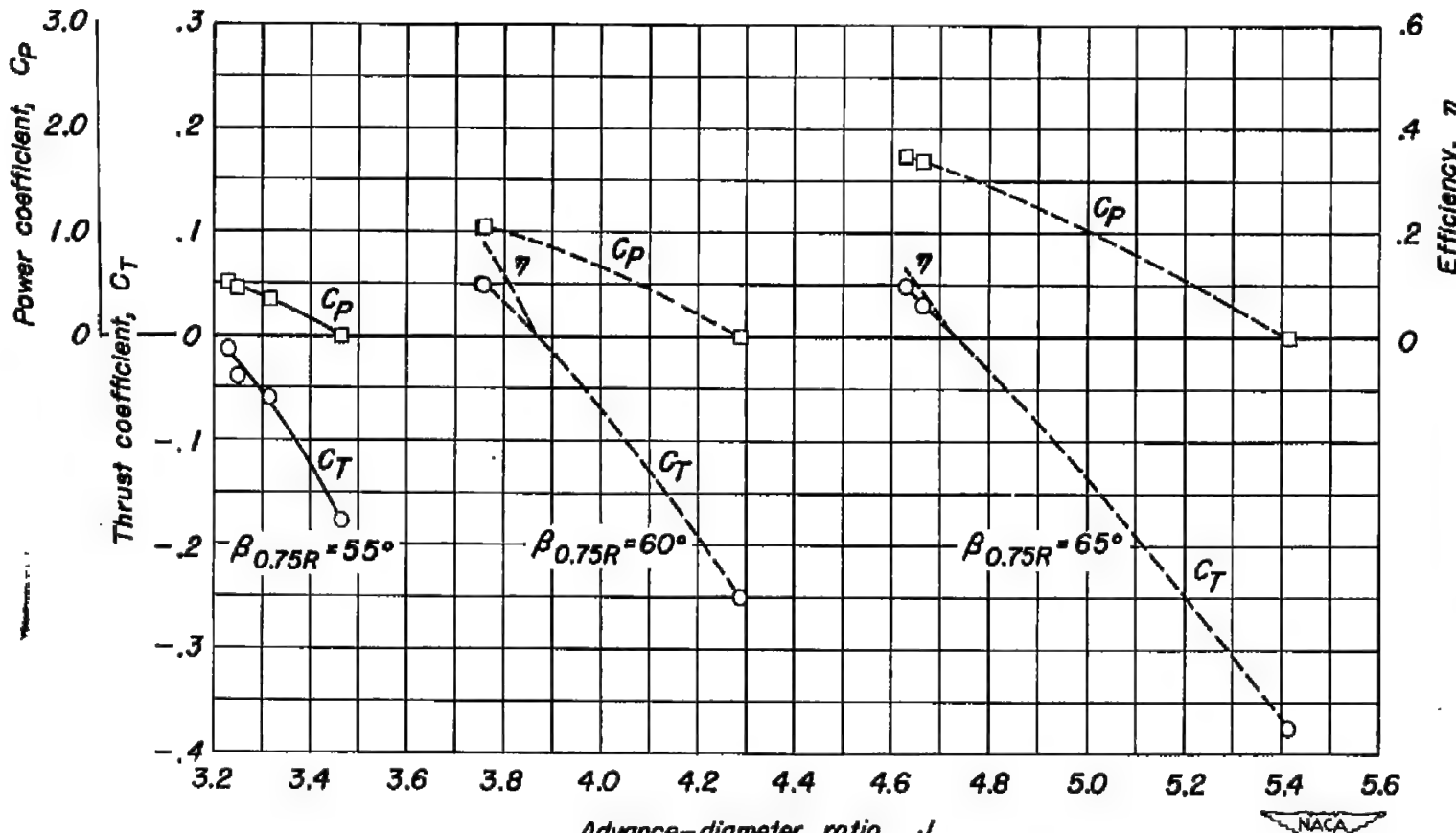
(b) $\alpha, 4^\circ$

Figure 9.- Continued.



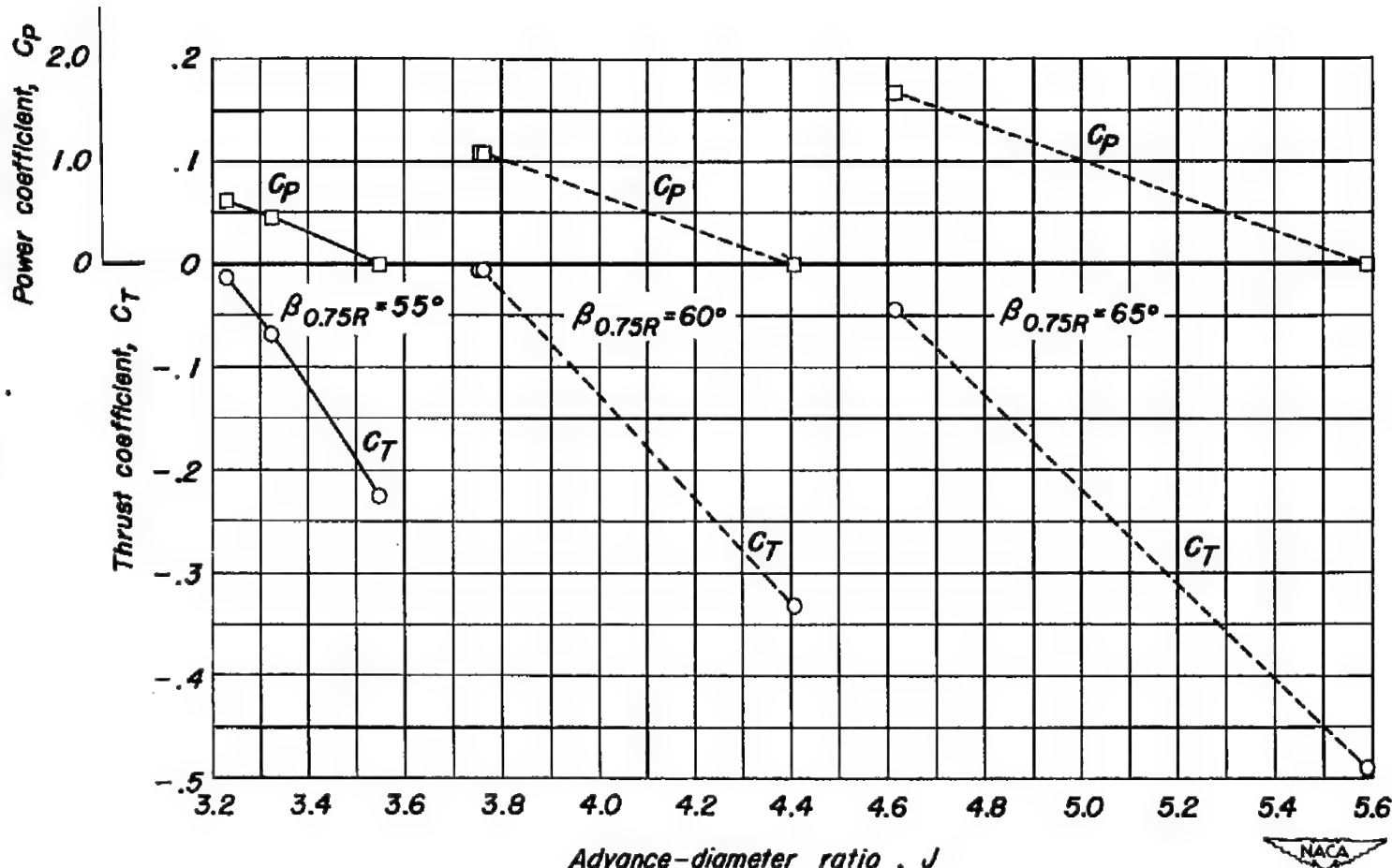
(c) $\alpha, 8^\circ$

Figure 9:- Concluded.



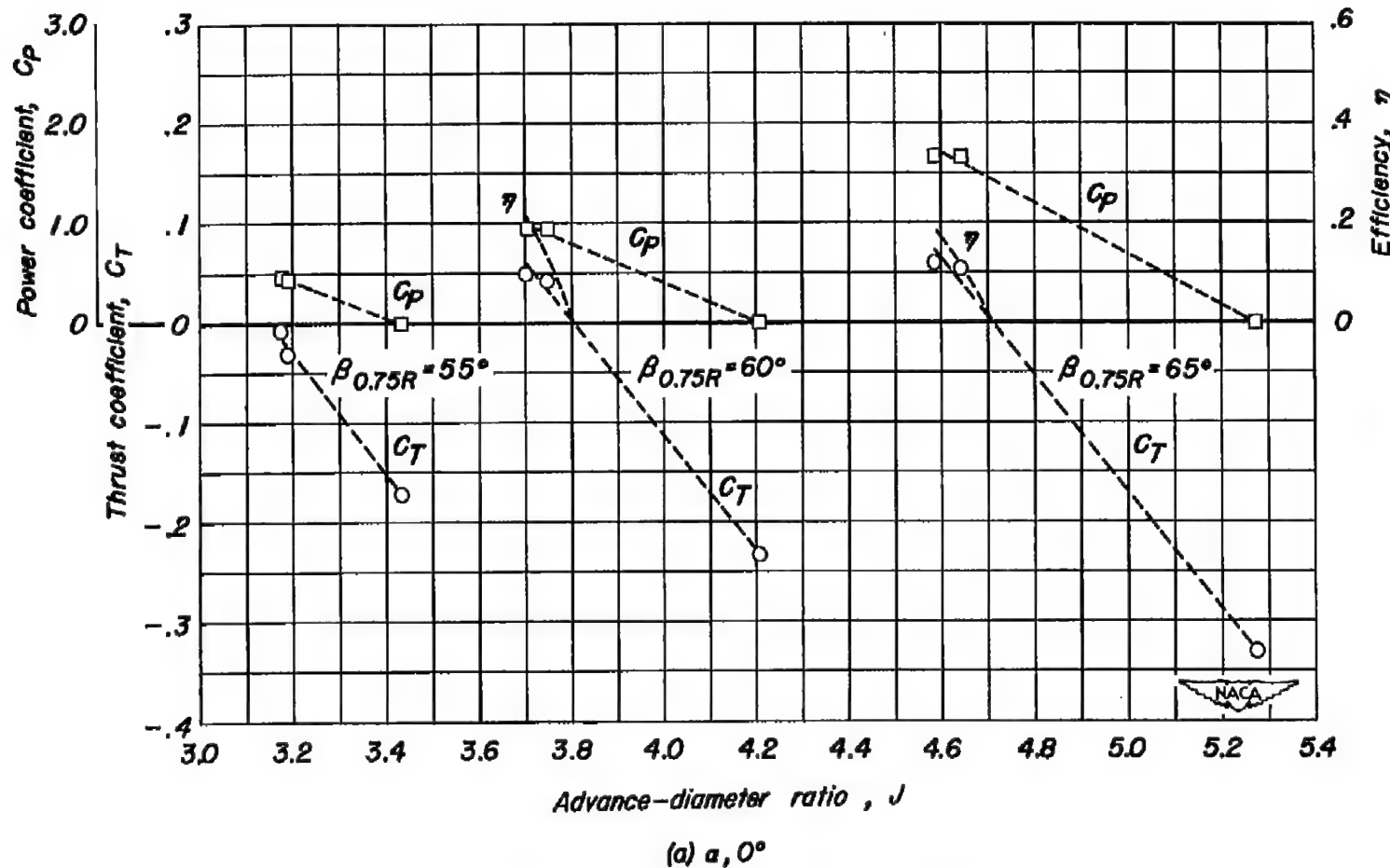


Figure 10.— Characteristics of the dual-rotating propeller. $M, 0.92$.

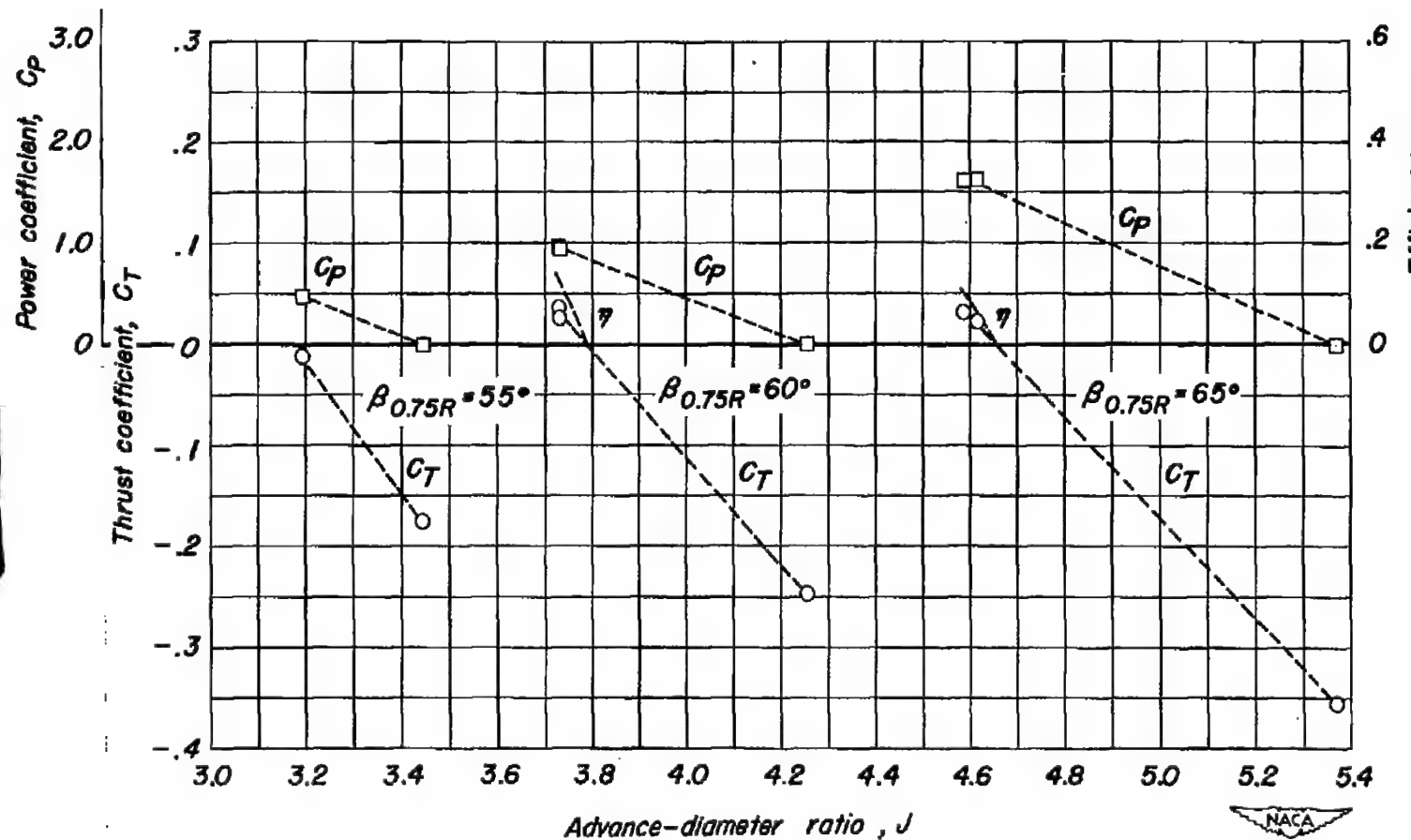
(b) $\alpha, 4^\circ$

Figure 10.- Continued.

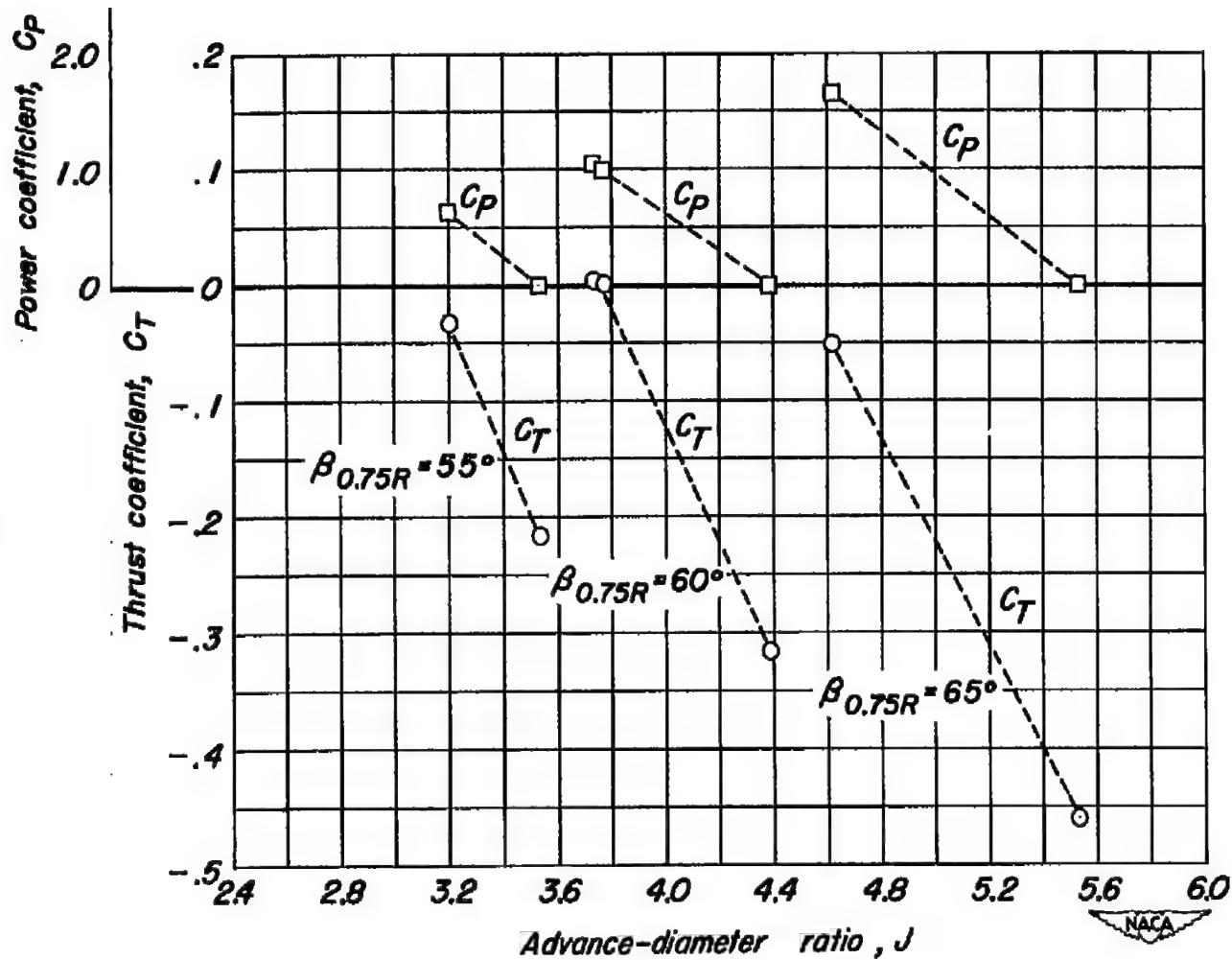
(c) $\alpha, 8^\circ$

Figure 10.- Concluded.

CONFIDENTIAL

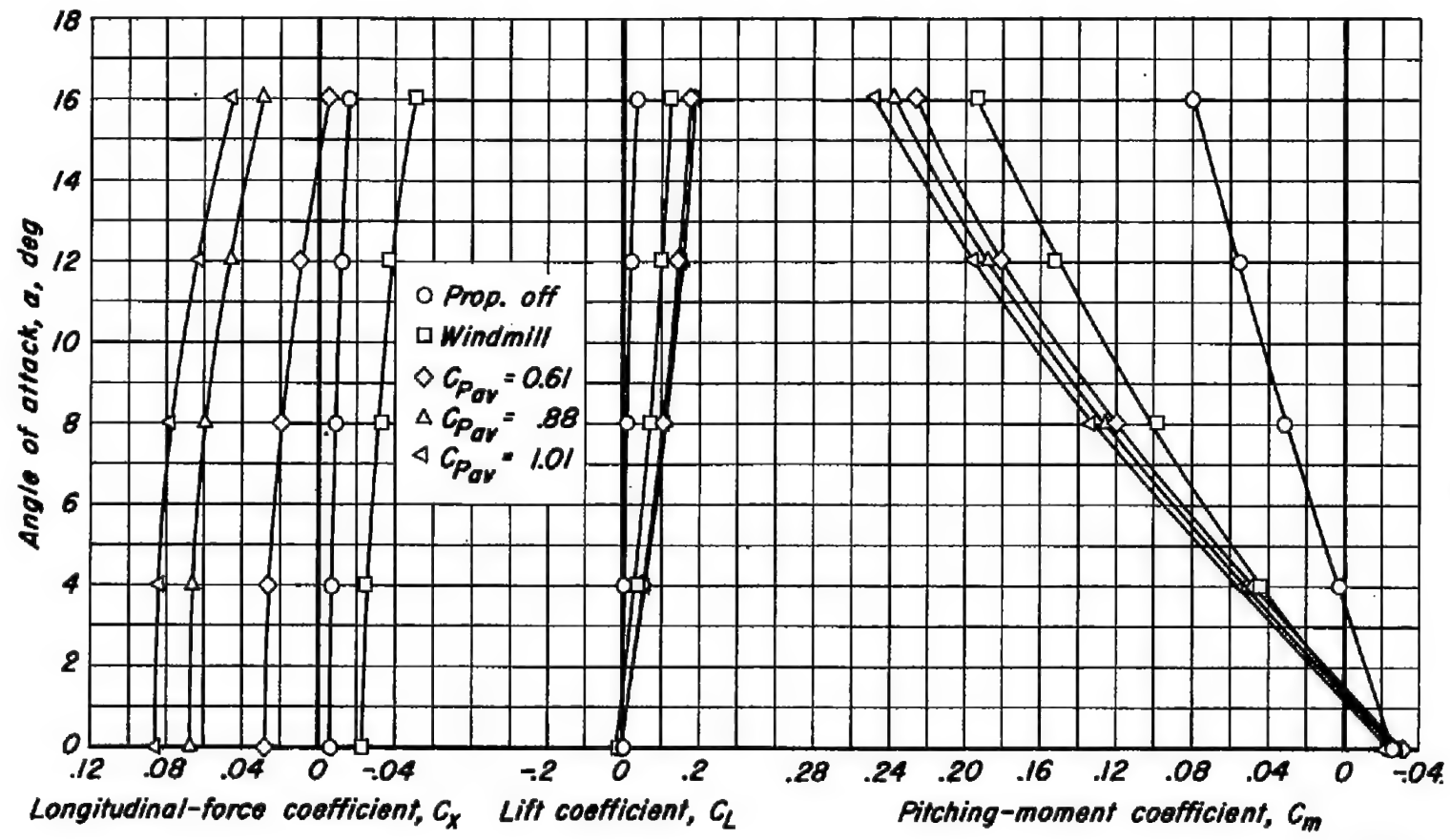
(a) $\beta_{0.75R}, 50^\circ$ 

Figure 11.-The effect of power on the longitudinal characteristics of the model fuselage. $M, 0.50$.

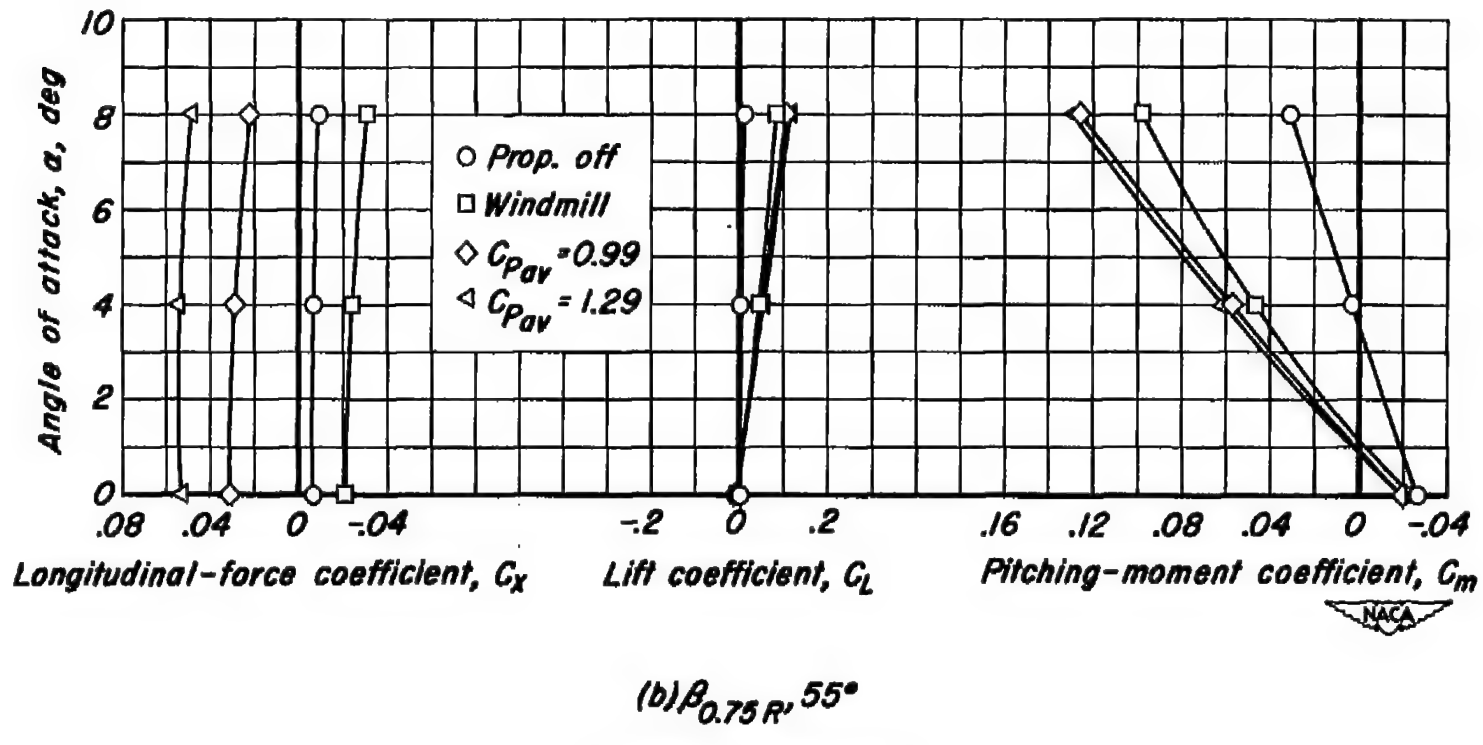
(b) $\beta_{0.75 R}, 55^\circ$

Figure 11.-Concluded.

CONTINUATION

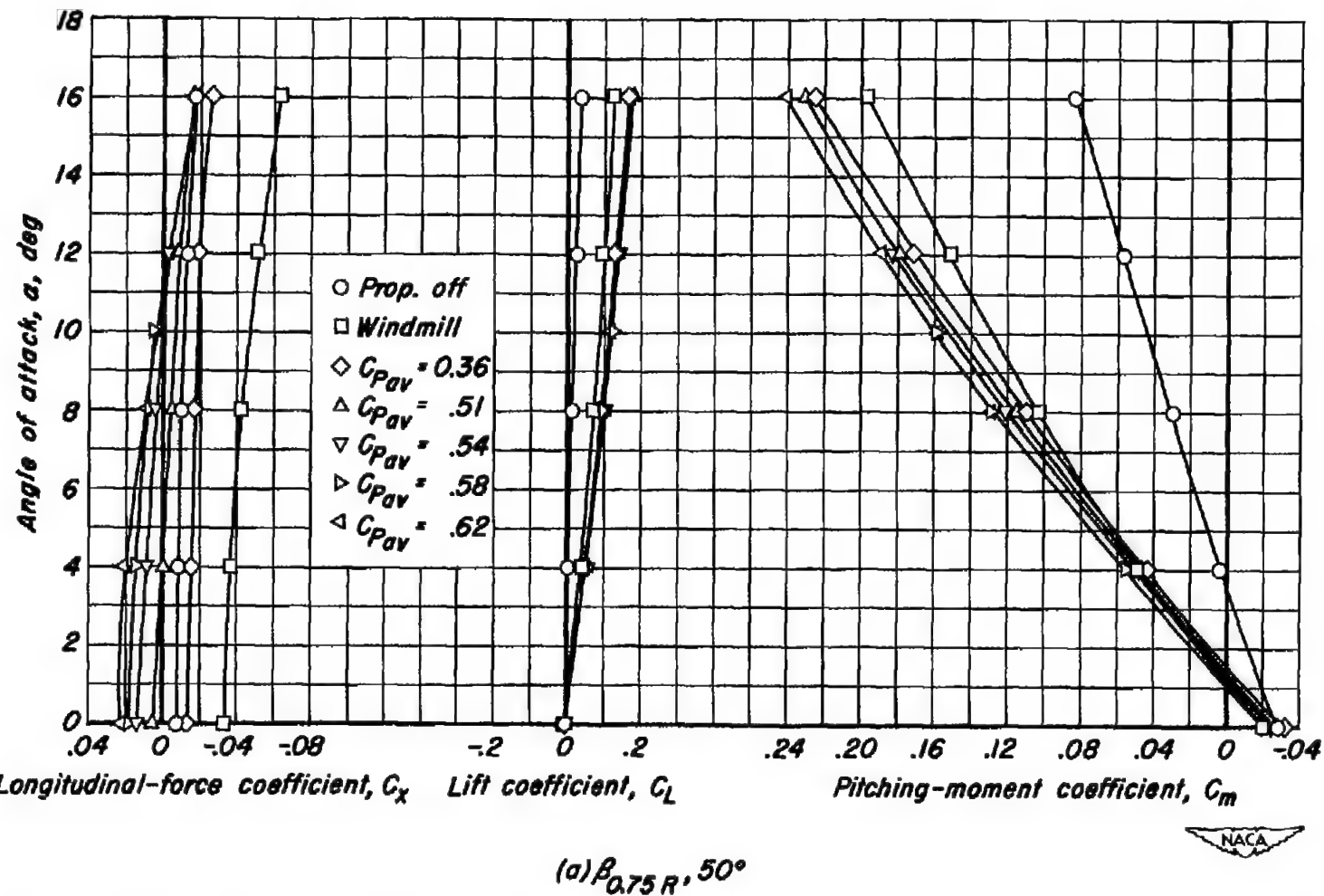


Figure 12.- The effect of power on the longitudinal characteristics of the model fuselage. $M, 0.70.$

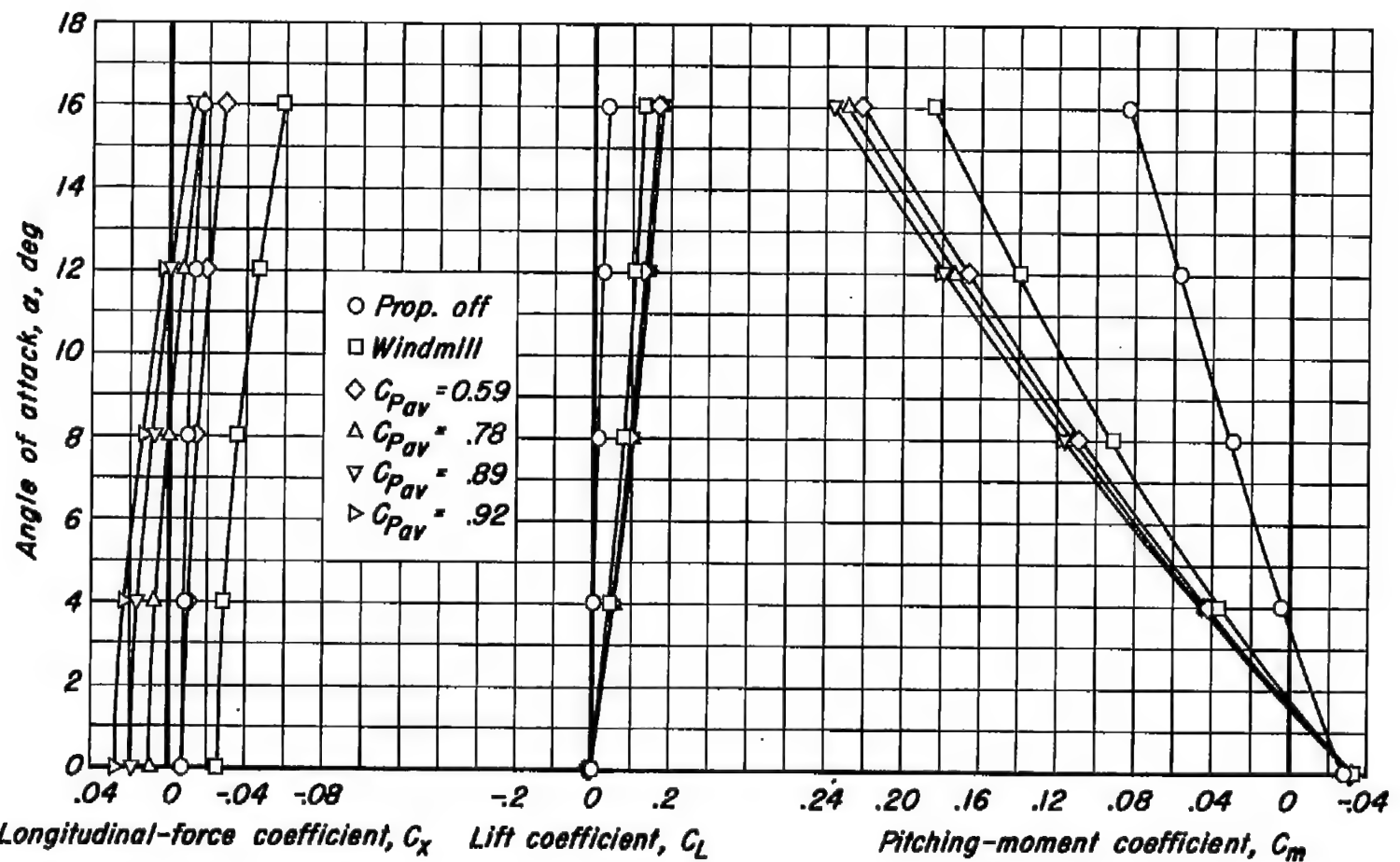
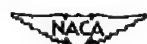
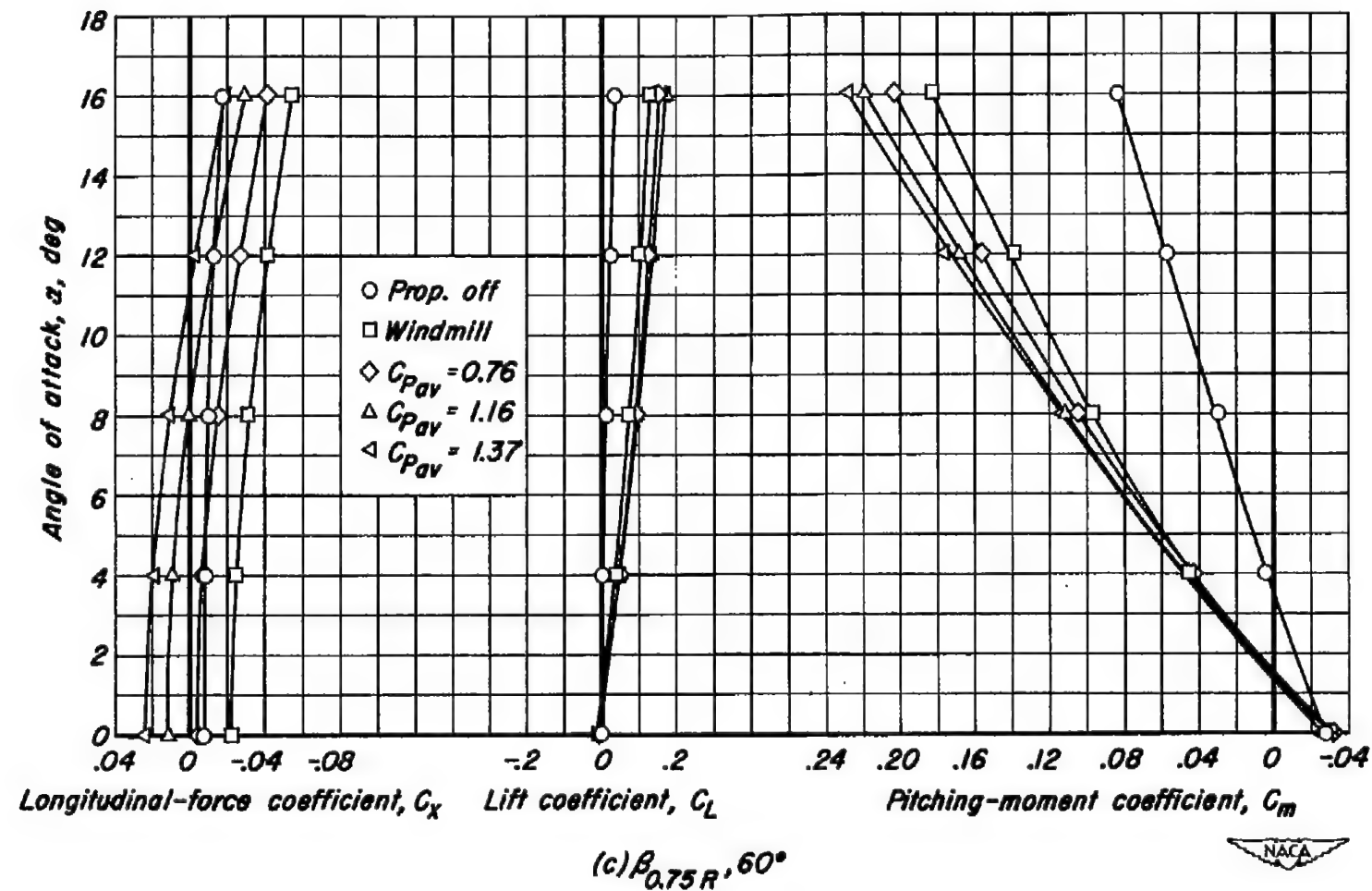
(b) $\beta_{0.75R}, 55^\circ$

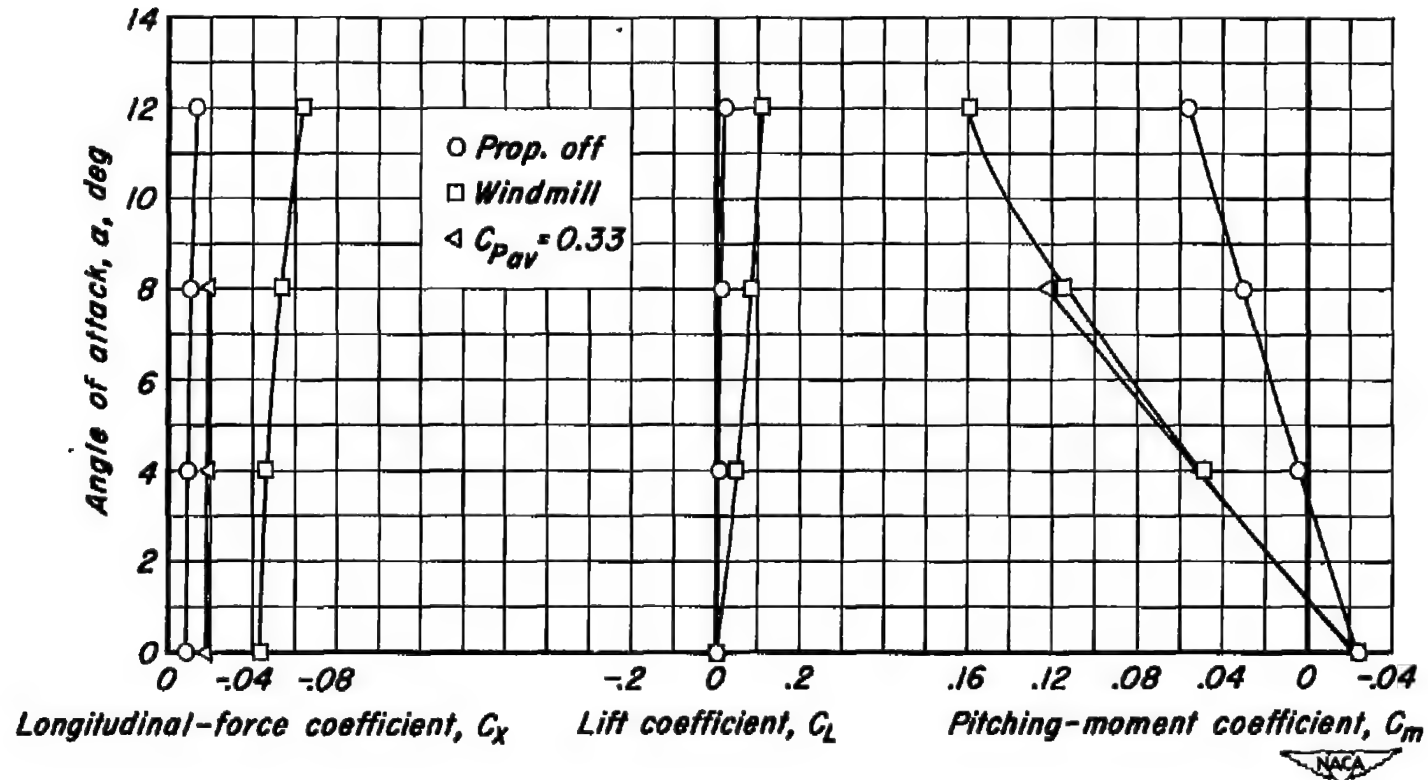
Figure 12.-Continued.





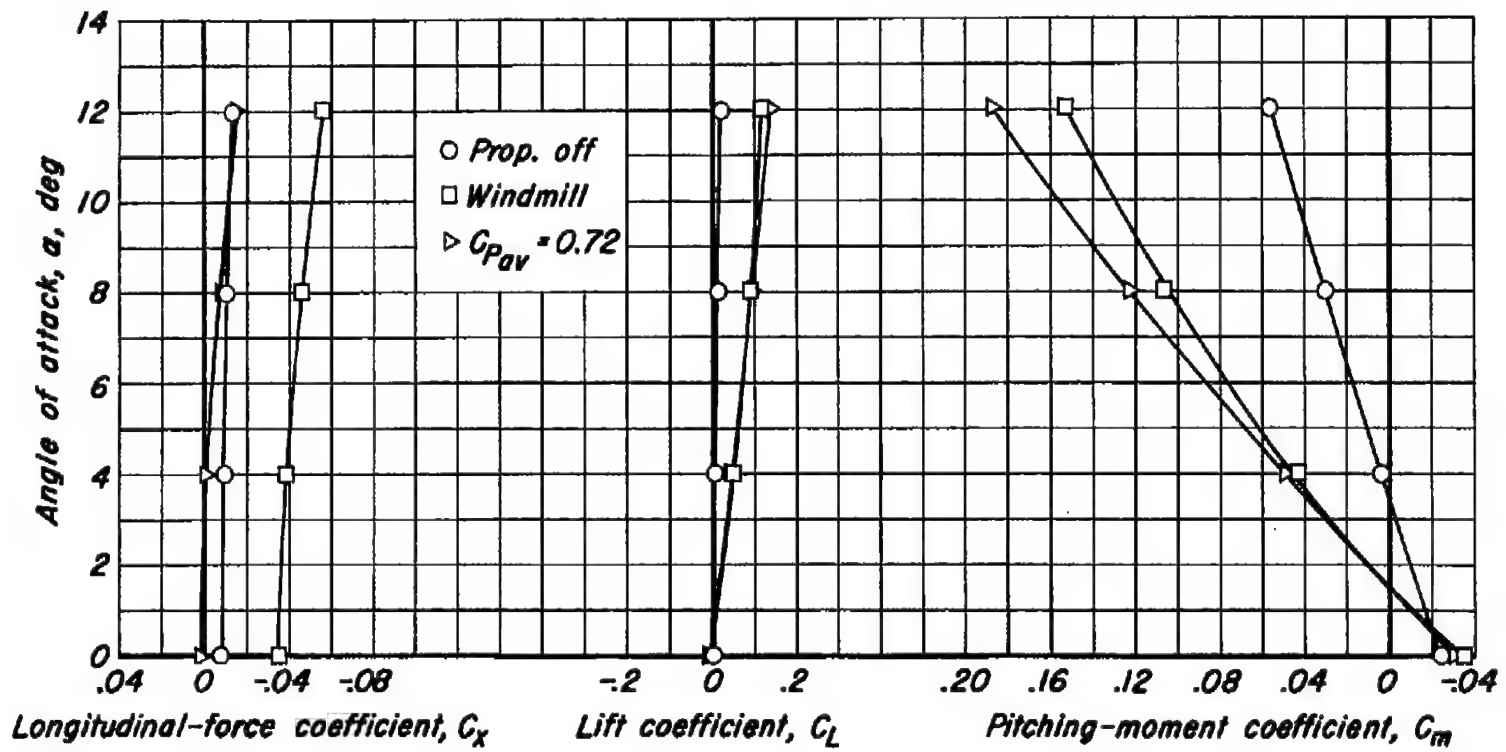
(c) $\beta_{0.75R}, 60^\circ$

Figure 12.-Concluded.



(a) $\beta_{0.75R}, 50^\circ$

Figure 13.-The effect of power on the longitudinal characteristics of the model fuselage. M, 0.80.



(b) $\beta_{0.75R}, 55^\circ$

Figure 13.-Continued.

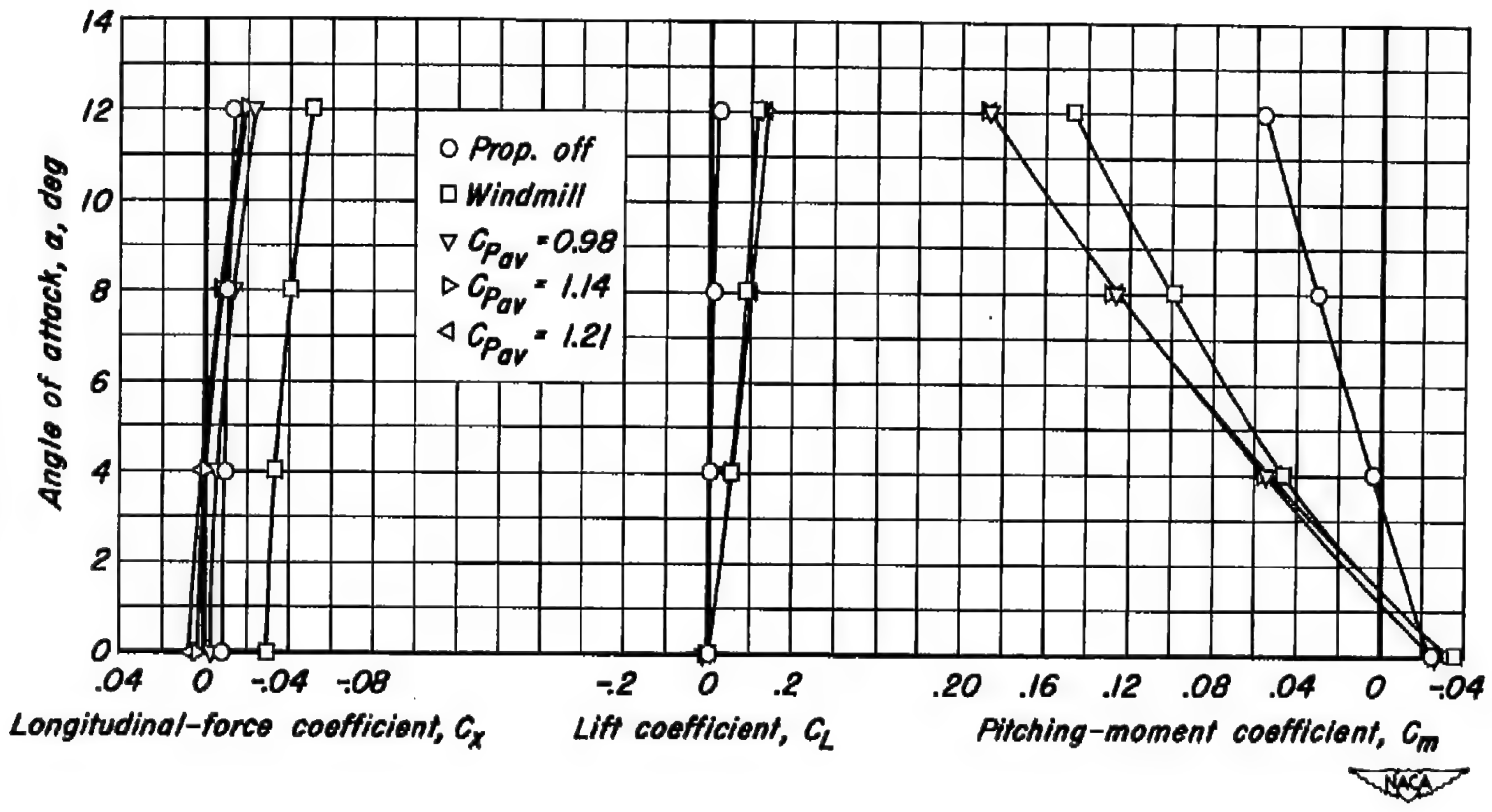
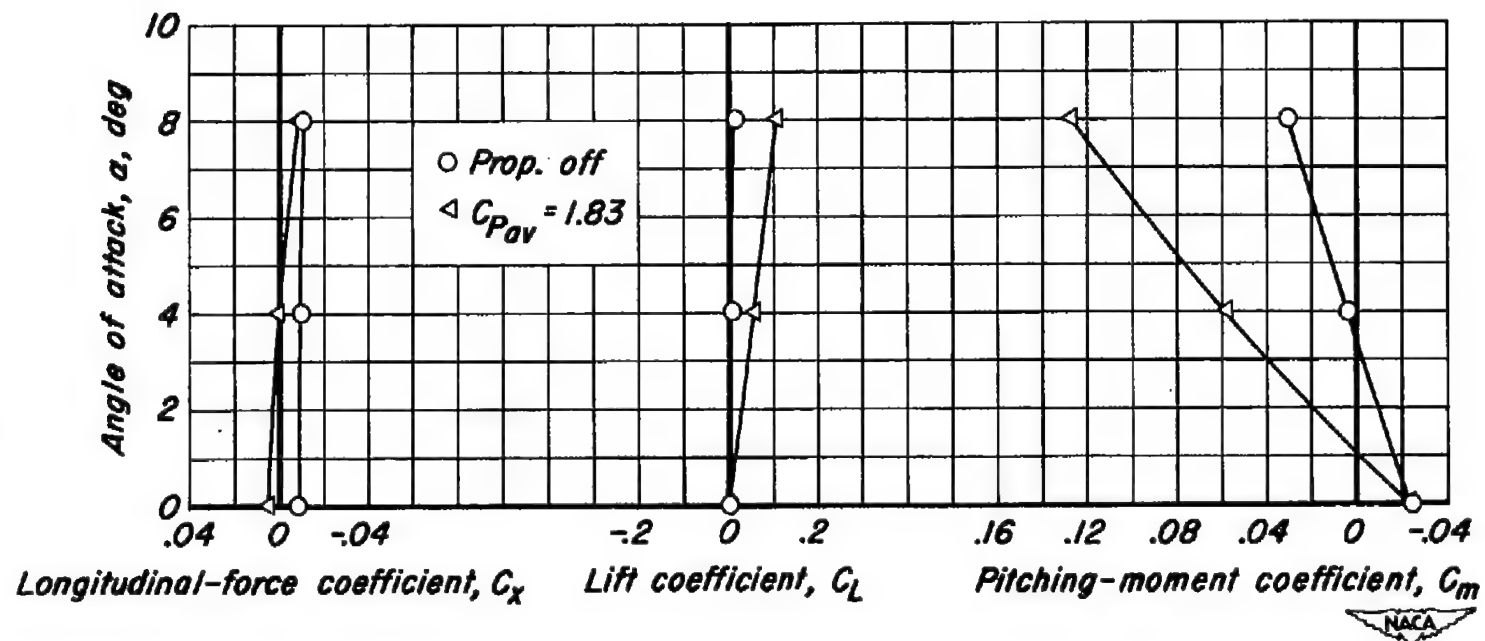
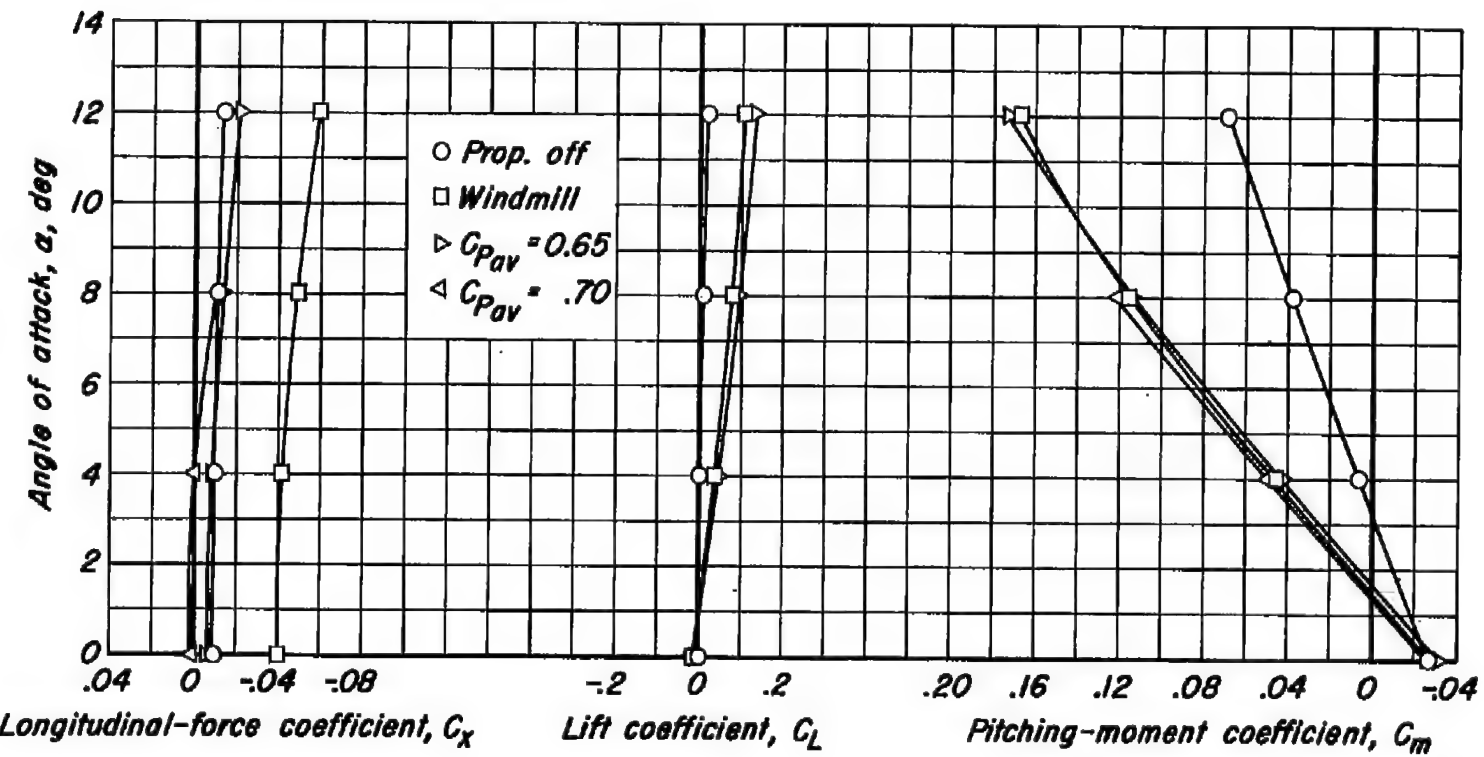
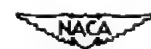
(c) $\beta_{0.75R}, 60^\circ$

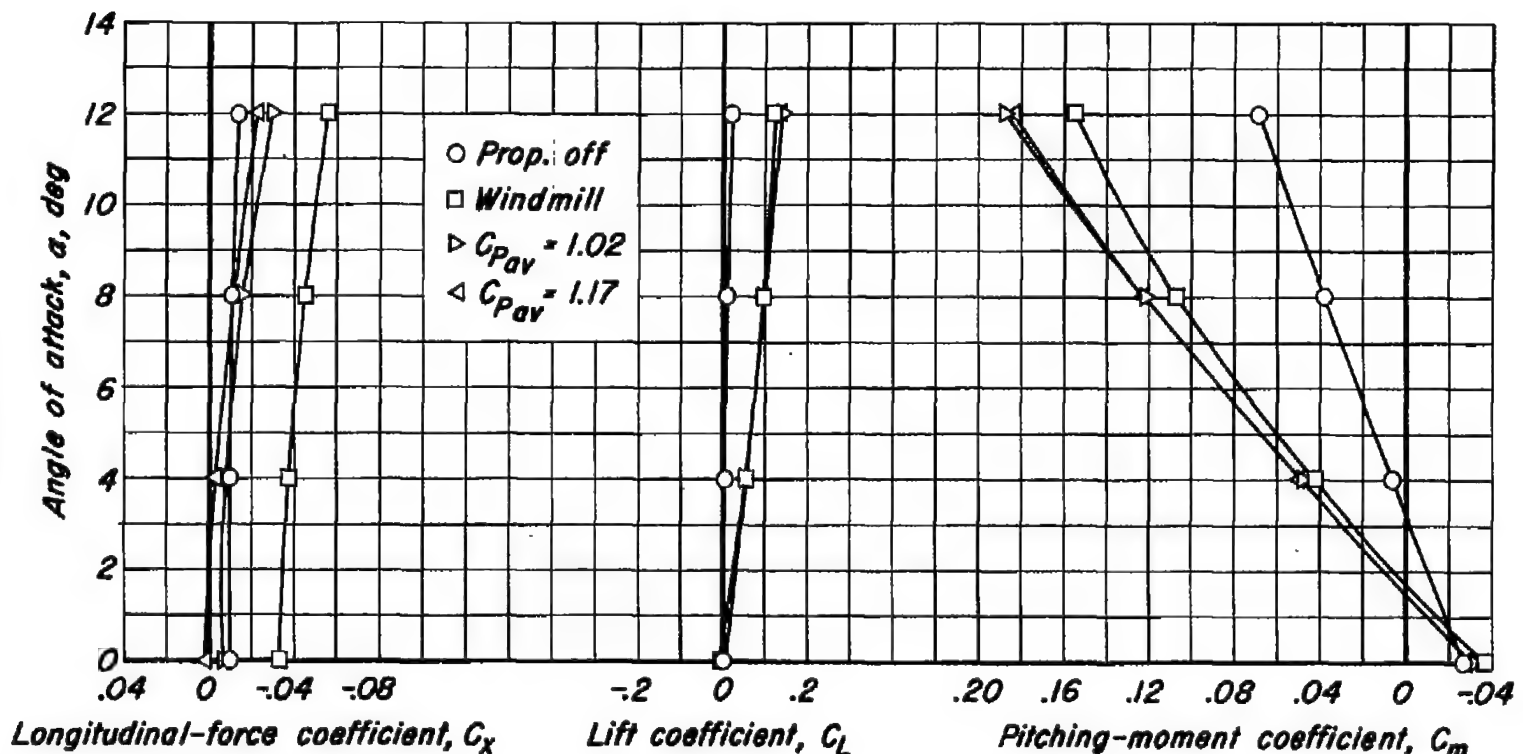
Figure 13.-Continued.



(d) $\beta_{0.75R}, 65^\circ$

Figure 13.-Concluded.

(a) $\beta_{0.75R}, 55^\circ$ Figure 14.-The effect of power on the longitudinal characteristics of the model fuselage. $M, 0.85$.



(b) $\beta_{0.75R}, 60^\circ$

Figure 14.-Continued.

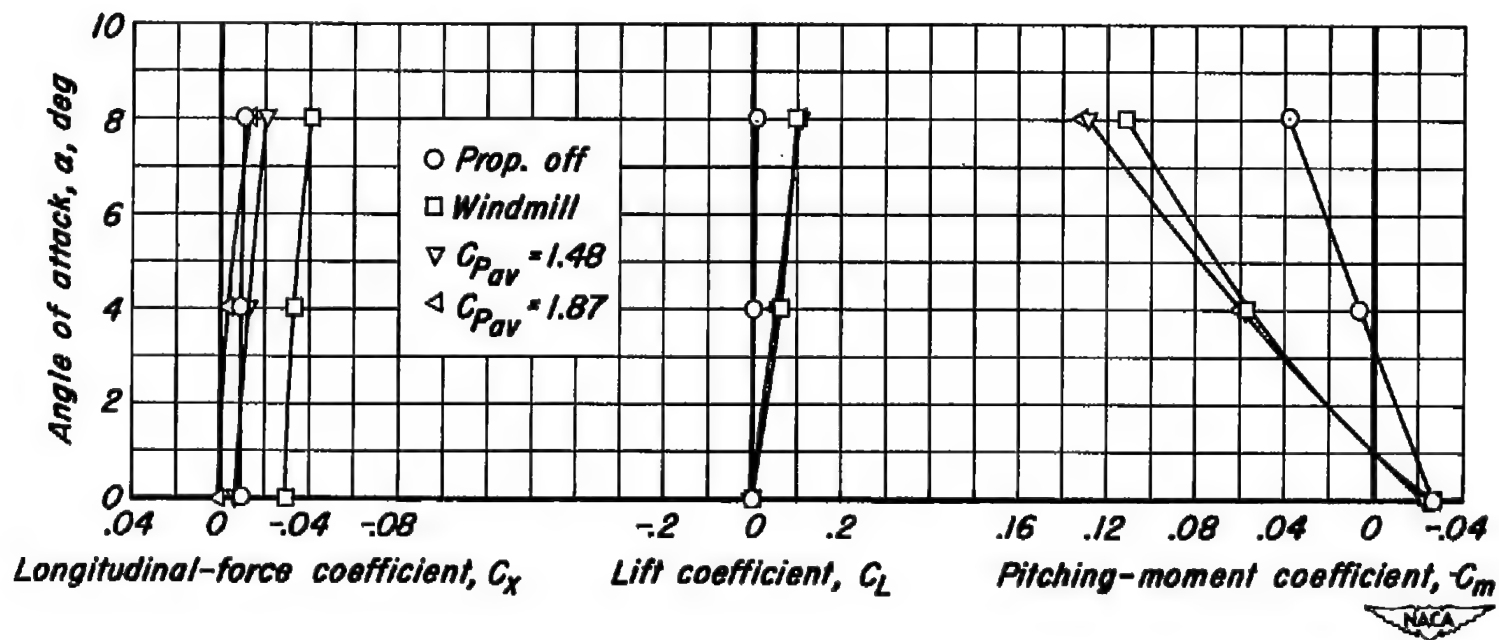
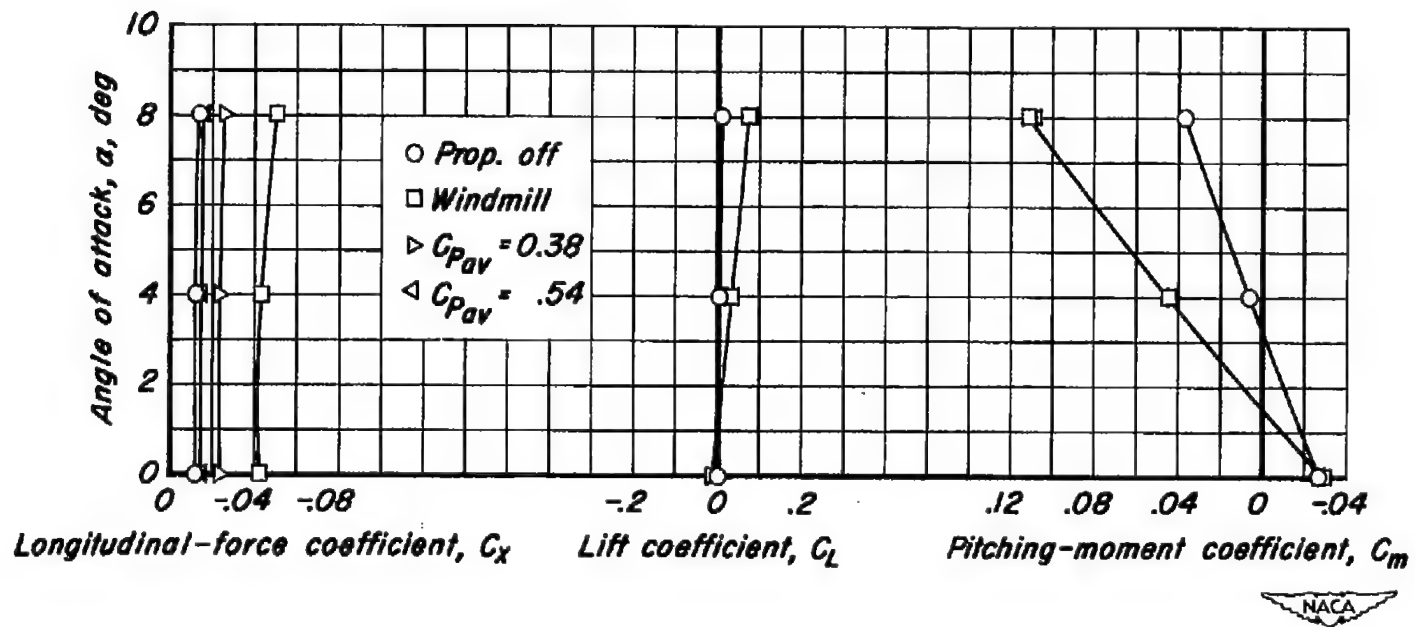
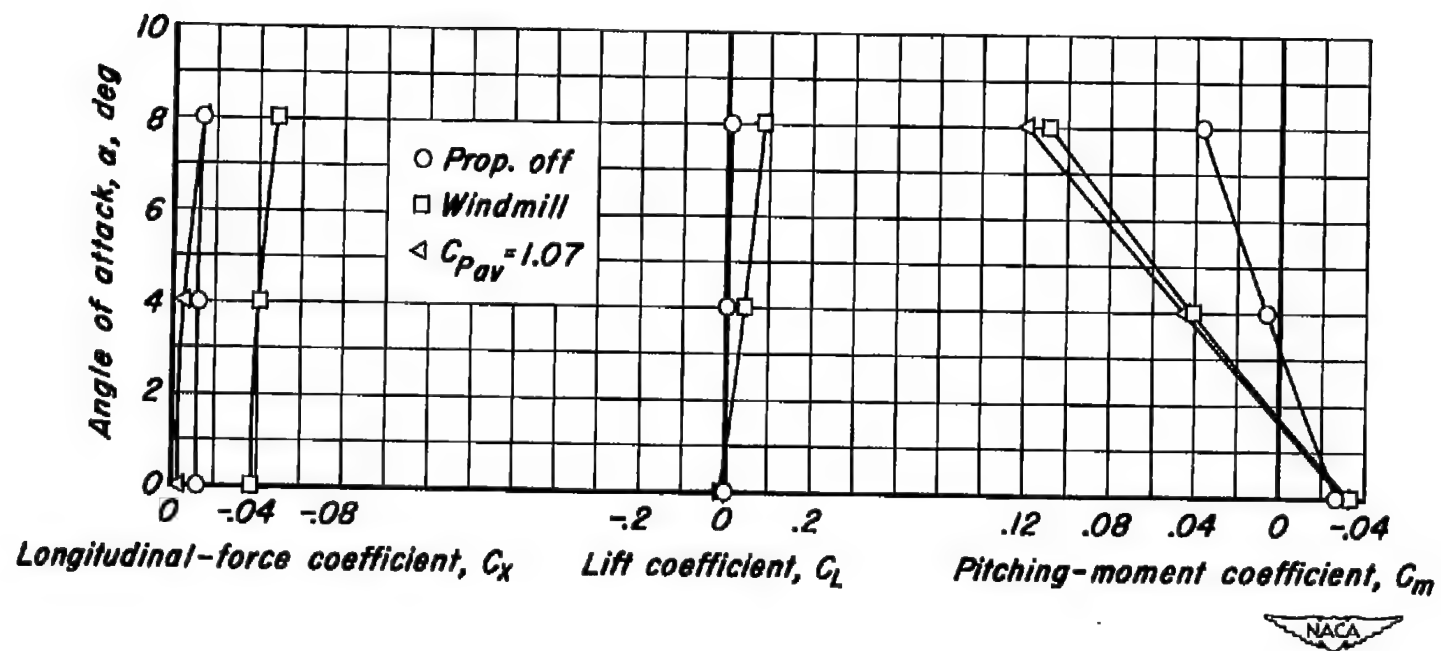
(c) $\beta_{0.75R}, 65^\circ$

Figure 14.-Concluded.



(a) $\beta_{0.75R}, 55^\circ$

Figure 15.-The effect of power on the longitudinal characteristics of the model fuselage. $M, 0.90$.



(b) $\beta_{0.75R}, 60^\circ$

Figure 15.-Continued.

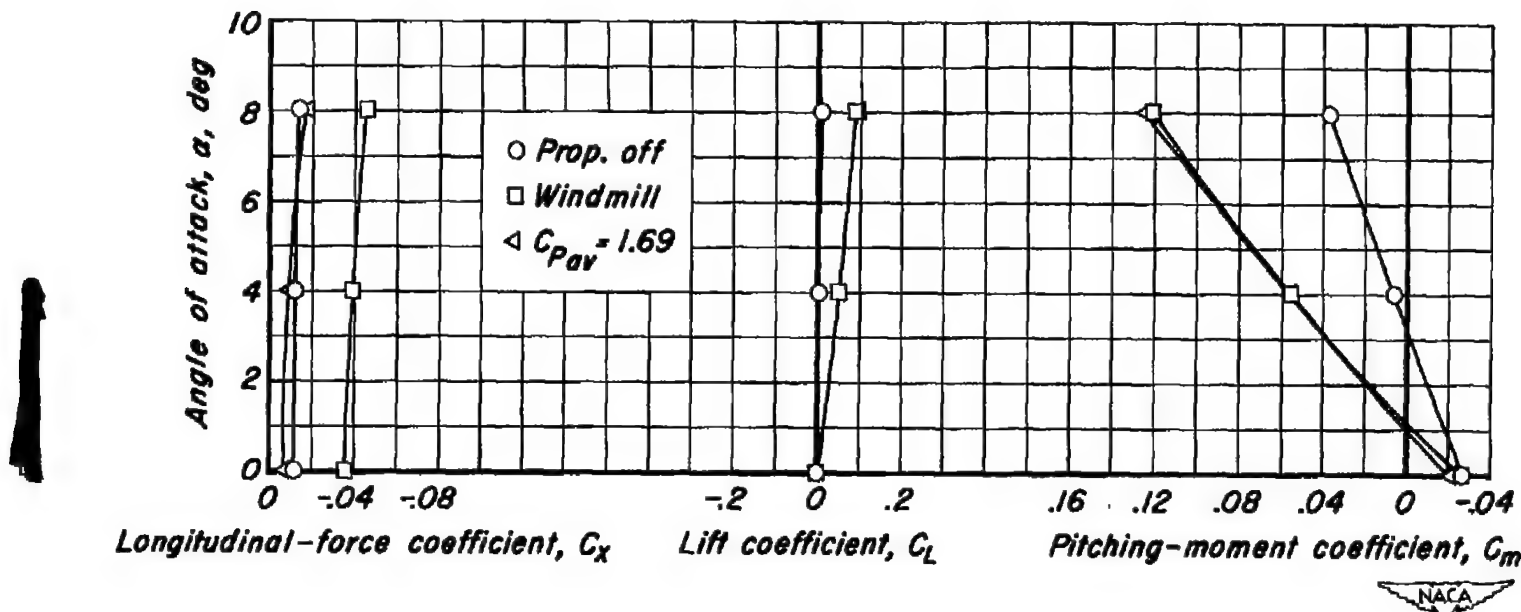
(c) $\beta_{0.75R}, 65^\circ$

Figure 15.-Concluded.

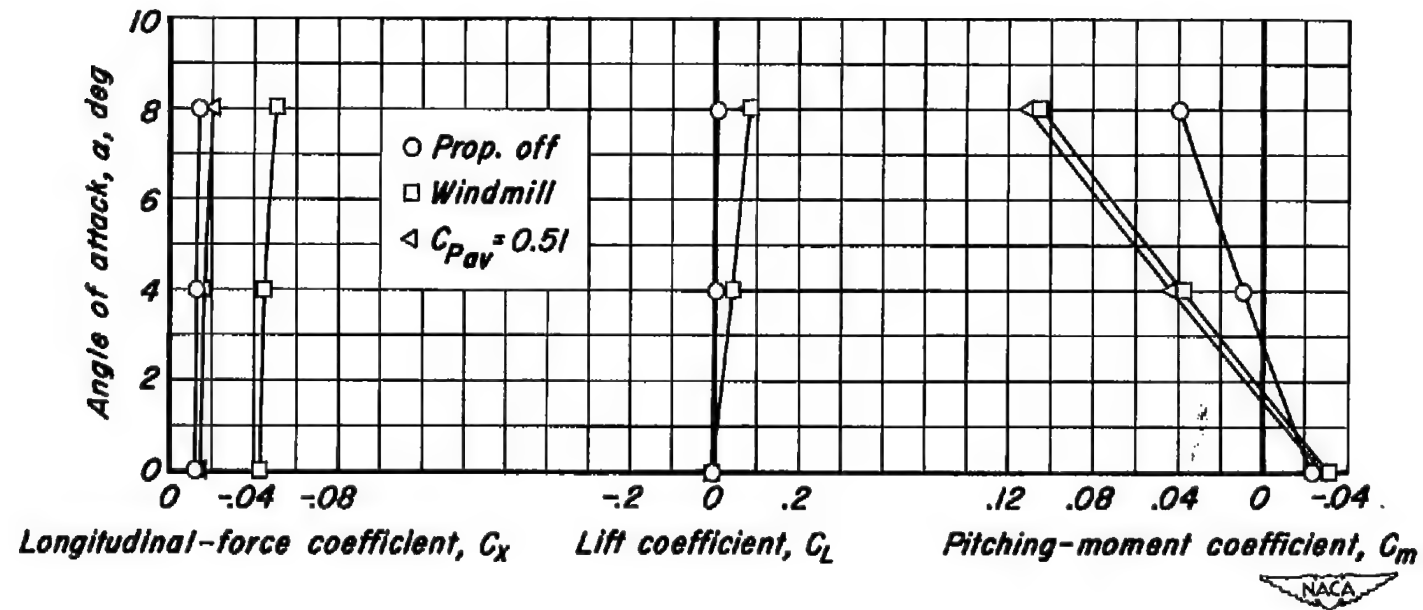
(a) $\beta_0 = 55^\circ$

Figure 16.- The effect of power on the longitudinal characteristics of the model fuselage. $M, 0.92$.

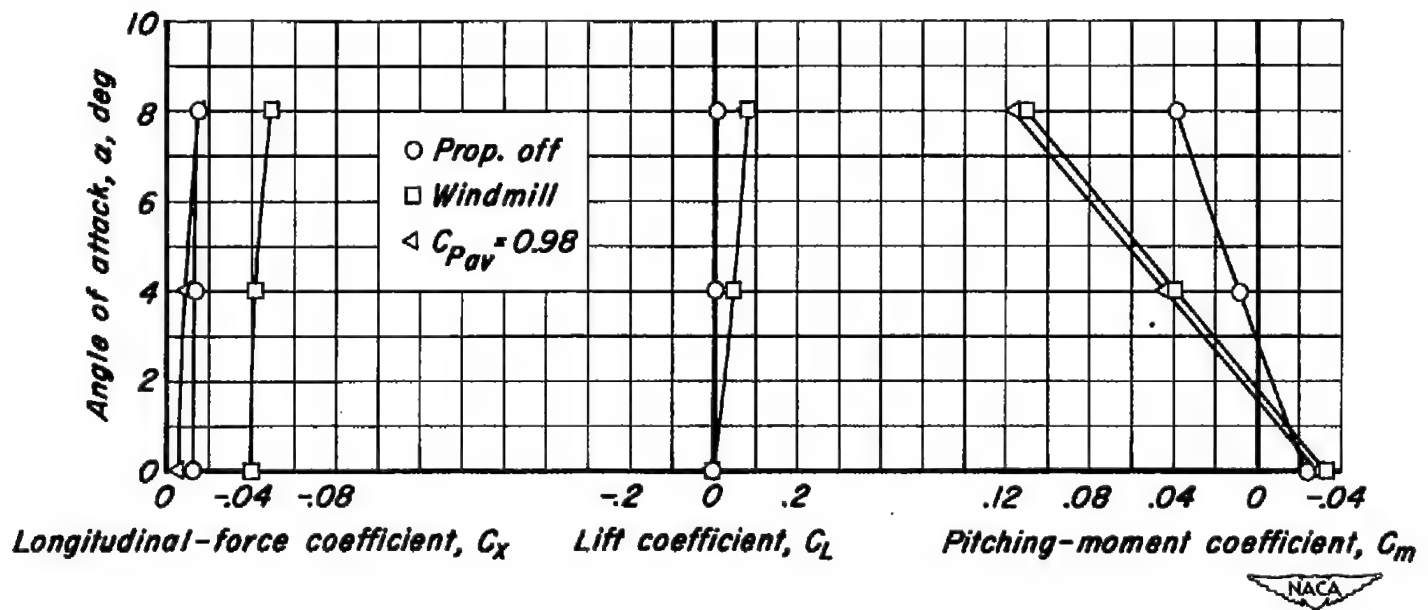
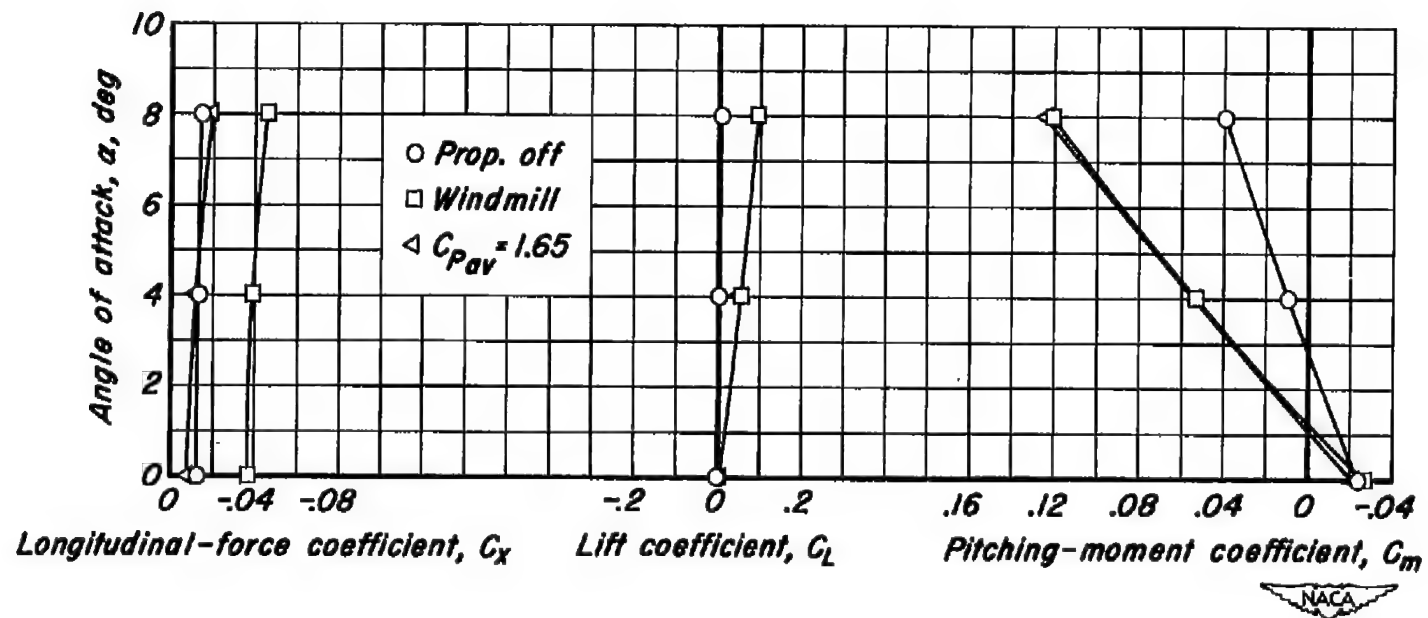
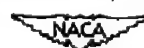
(b) $\rho_{0.75R}, 60^\circ$

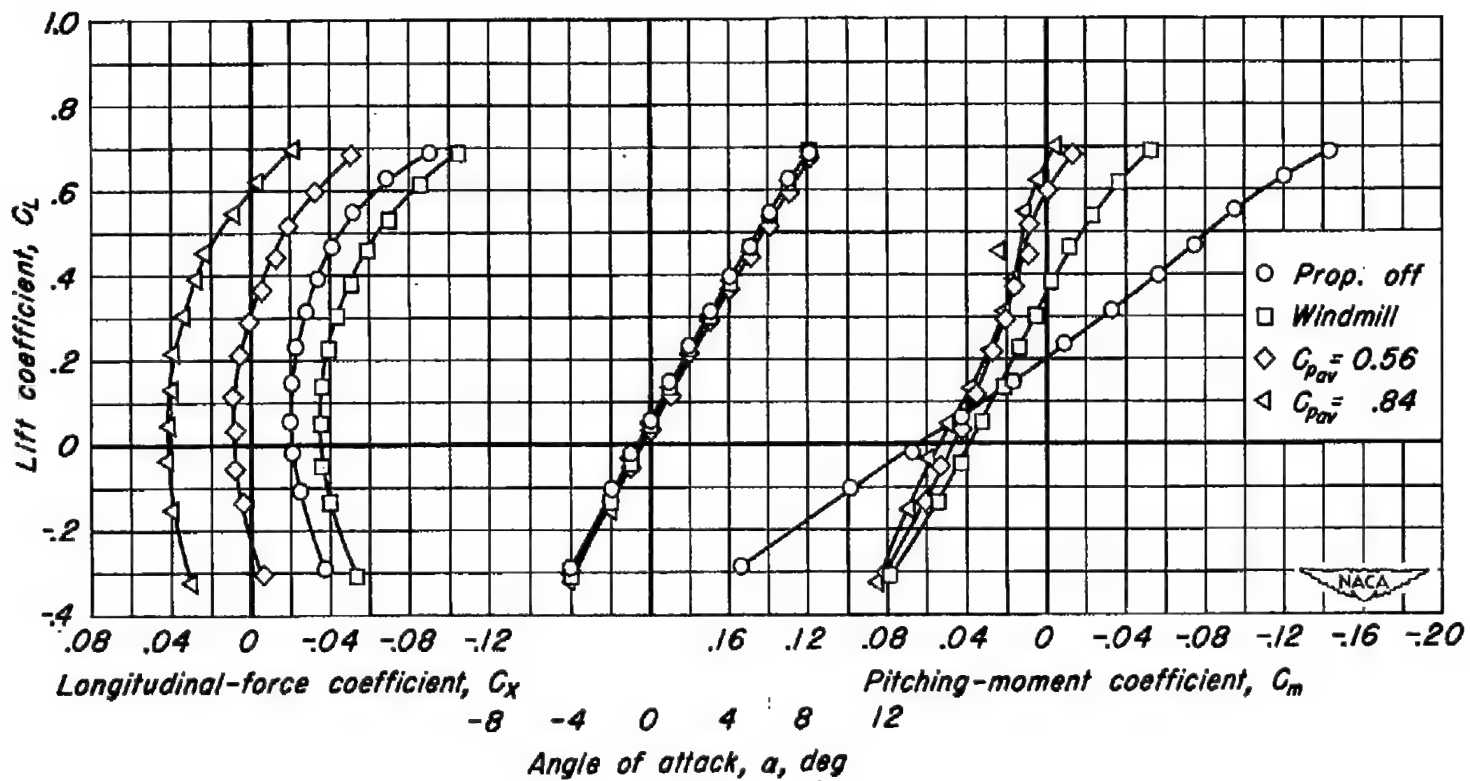
Figure 16.-Continued.



(c) $\beta_{0.75R}, 65^\circ$

Figure 16.- Concluded.



(a) $\beta_{0.75R}, 50^\circ$ Figure 17.- The effect of power on the longitudinal characteristics of the model. $M, 0.50$.

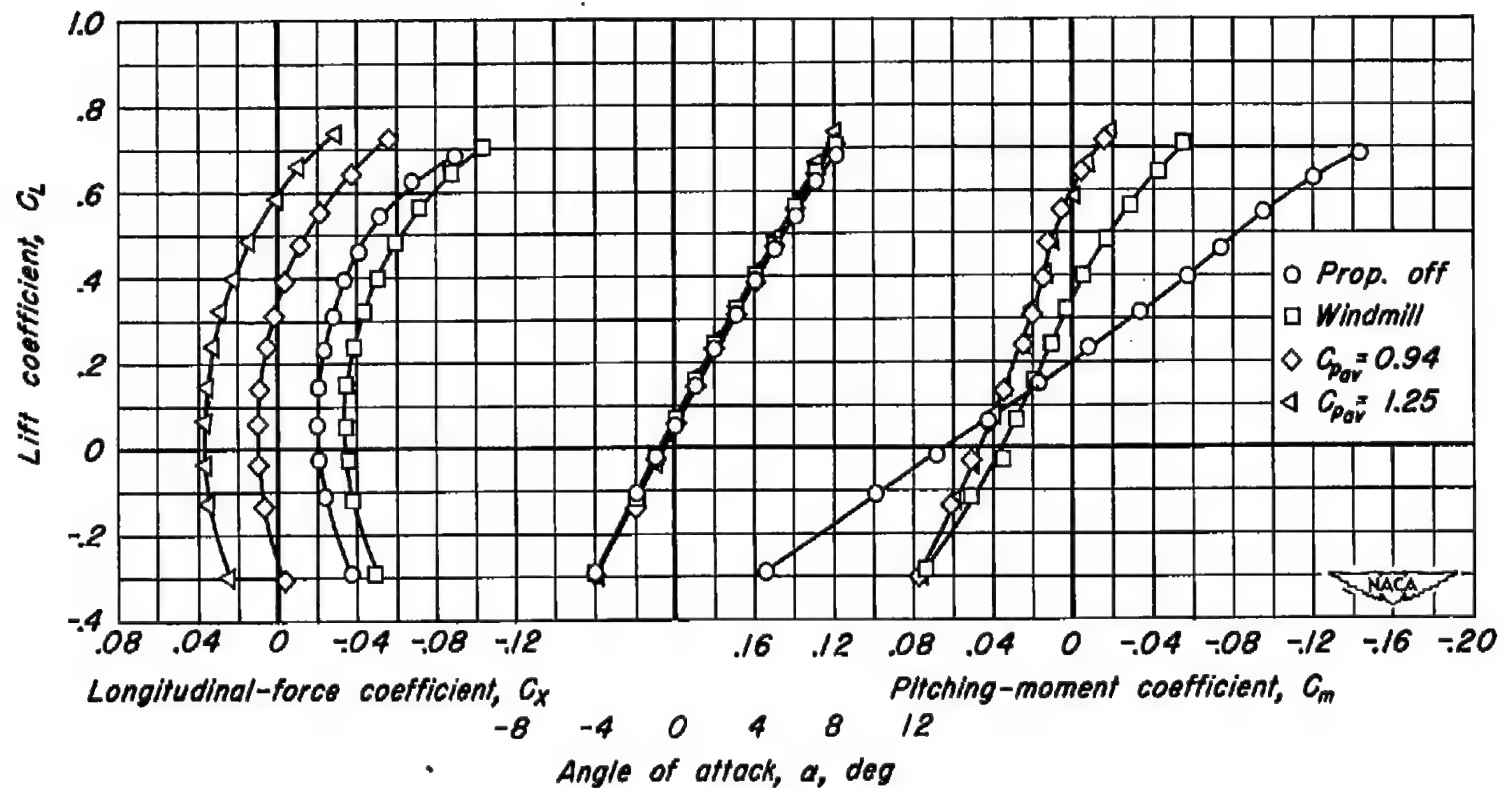
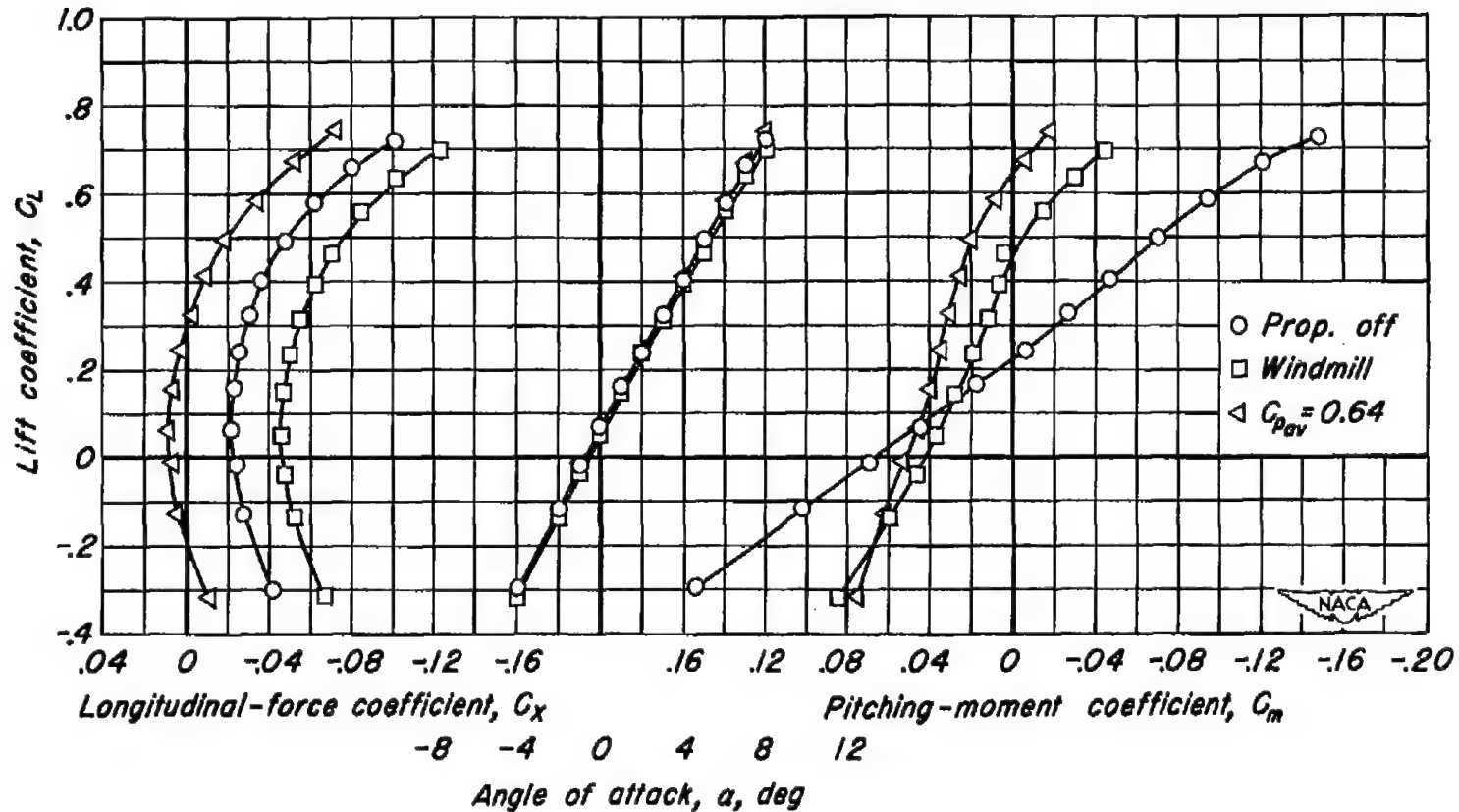
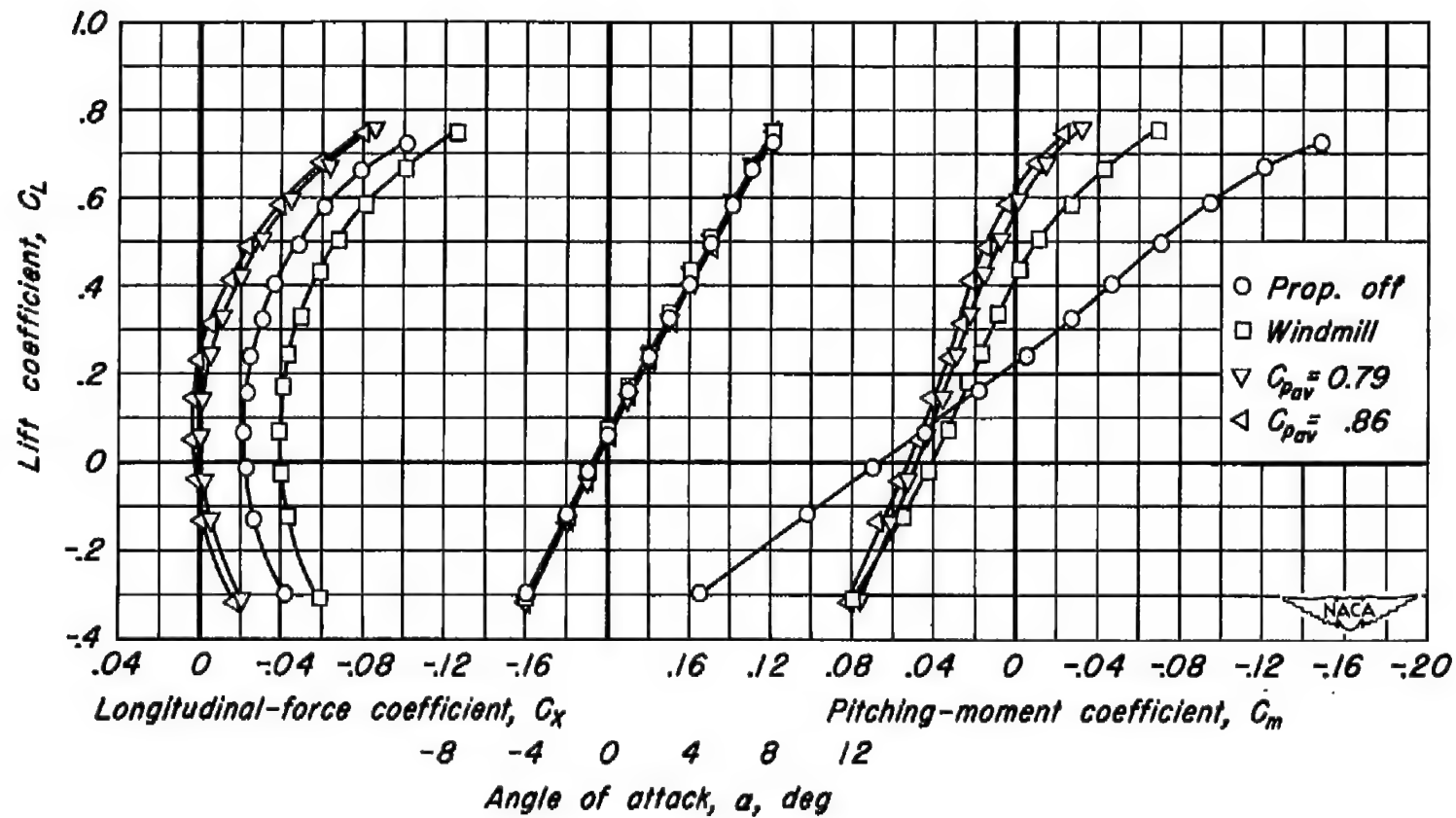
(b) $\beta_{0.75R}, 55^\circ$

Figure 17.- Concluded.



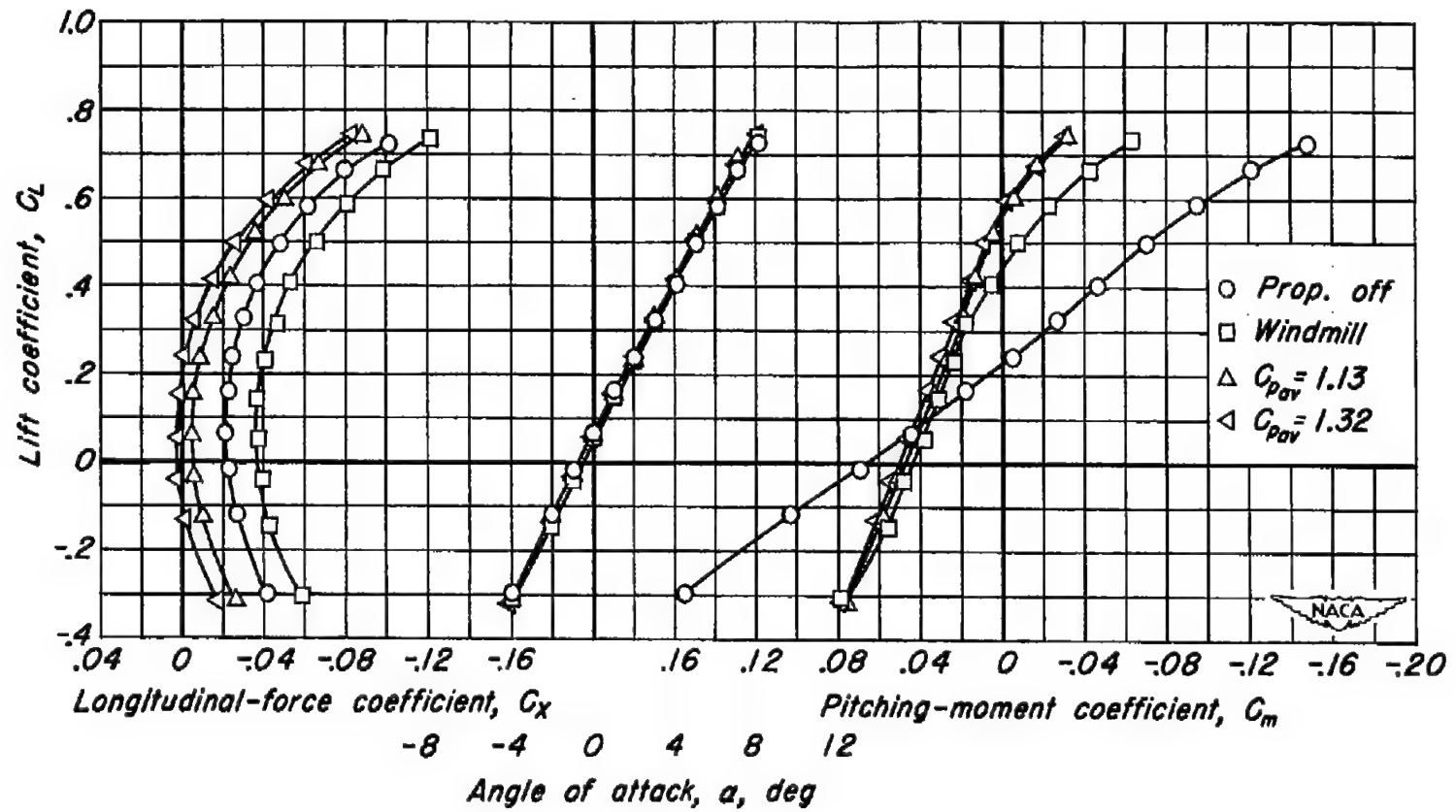
(a) $\beta_{0.75 R}, 50^\circ$

Figure 18.- The effect of power on the longitudinal characteristics of the model. $M, 0.70$.



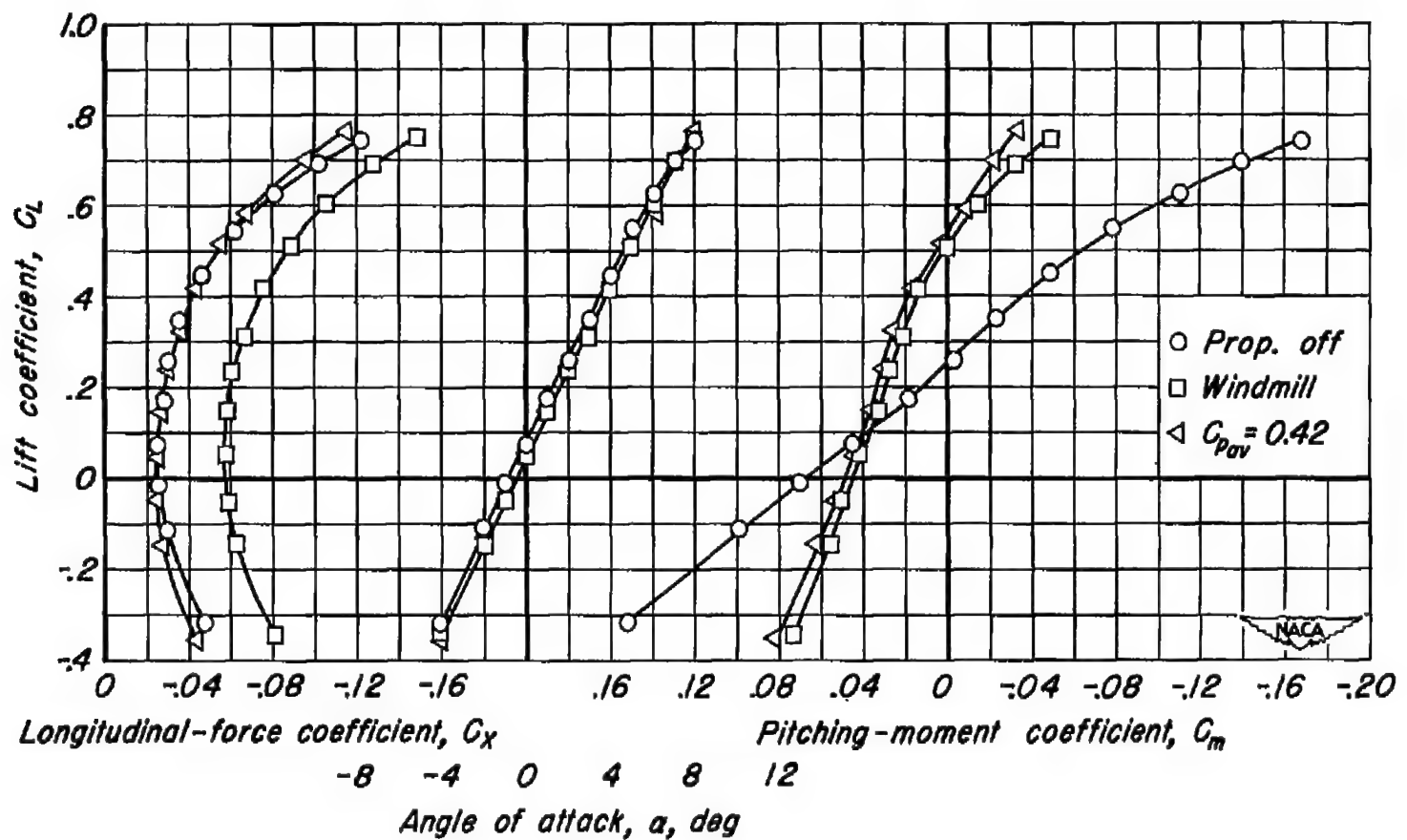
(b) $\beta_{0.75R}, 55^\circ$

Figure 18.- Continued.



(c) $\beta_{0.75R}, 60^\circ$

Figure 18.- Concluded.

(a) $\beta_{0.75R}, 50^\circ$ Figure 19.- The effect of power on the longitudinal characteristics of the model. $M, 0.80$.

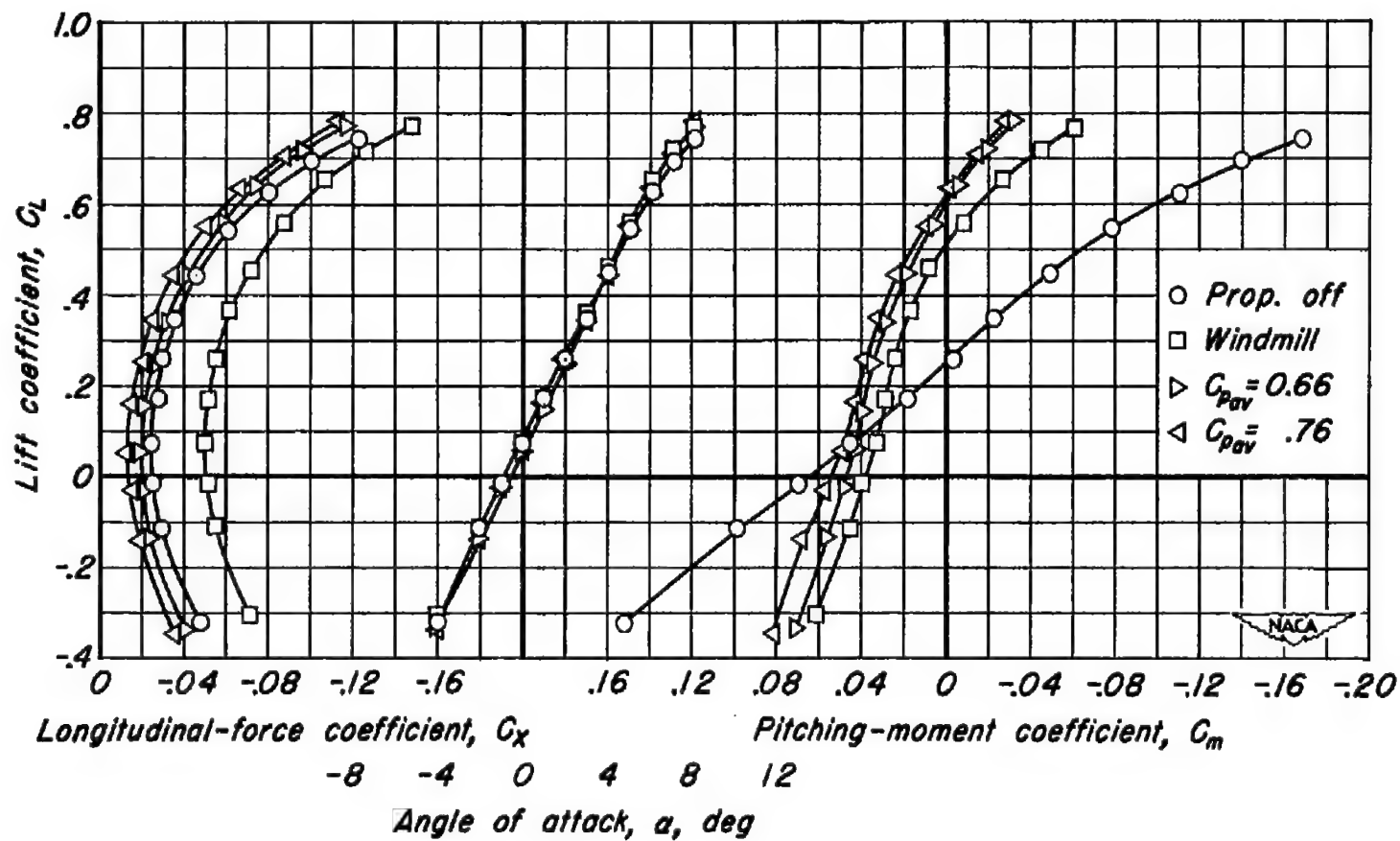
(b) $\beta_{0.75R}, 55^\circ$

Figure 19.- Continued.

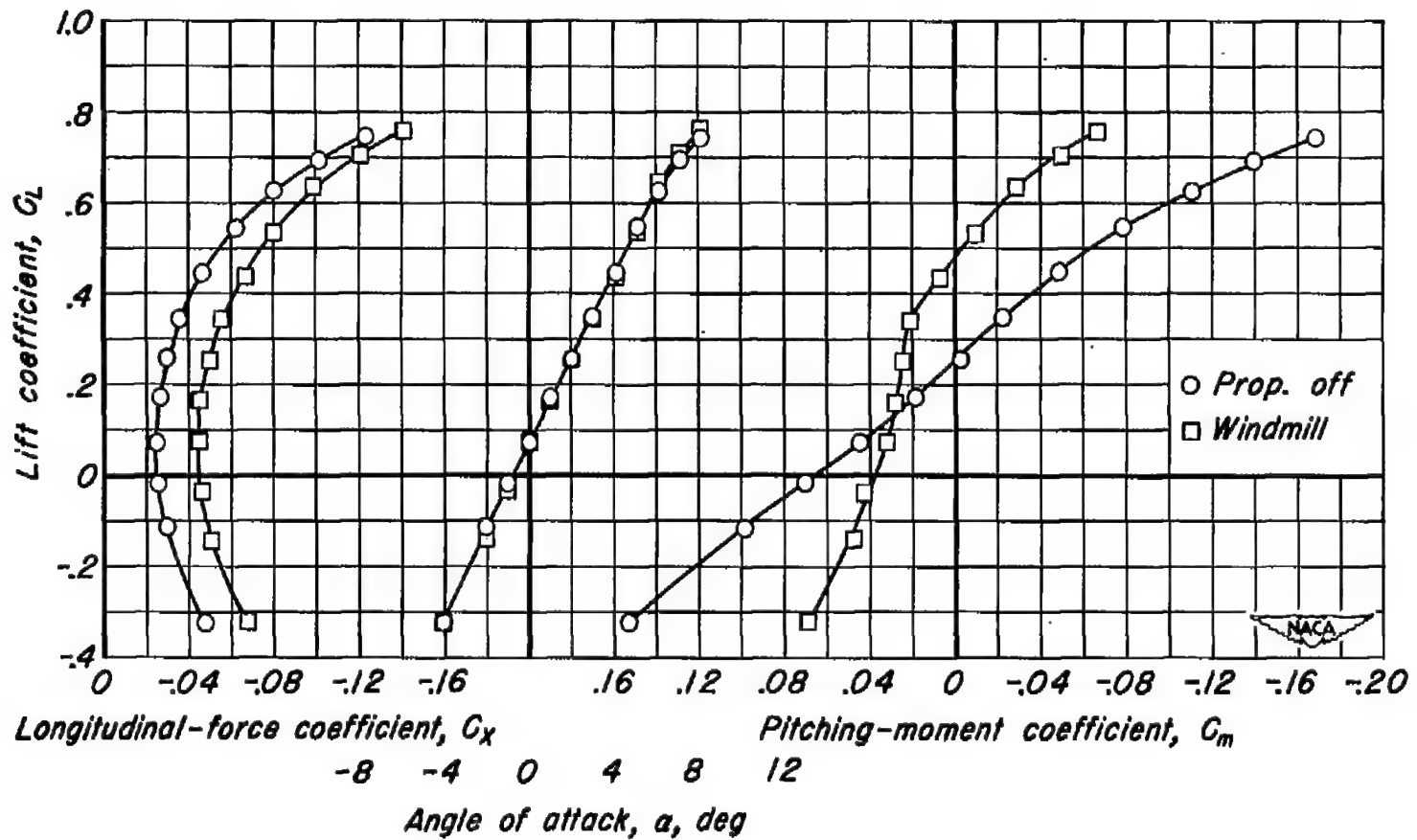
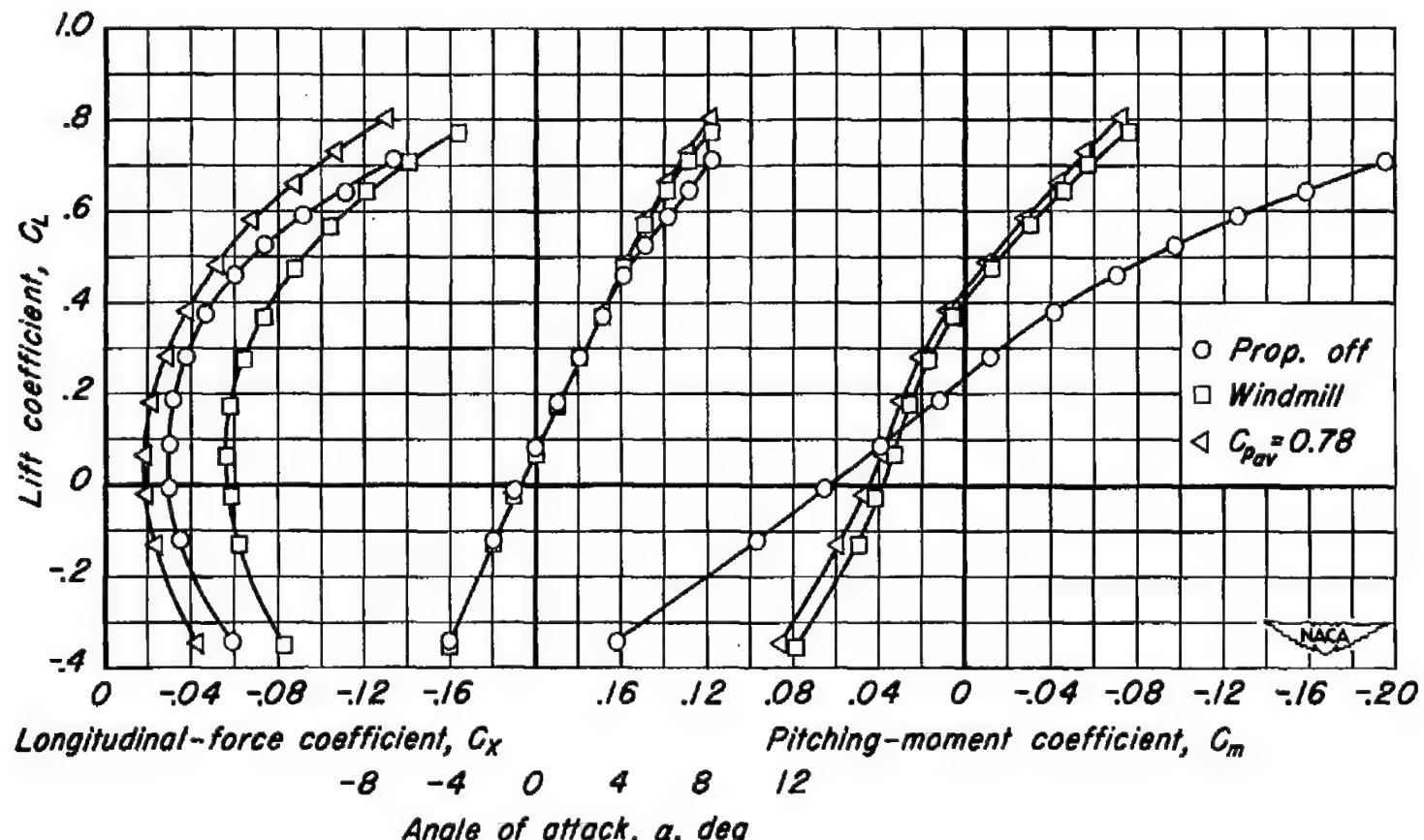
(c) $\beta_{0.75R}, 60^\circ$

Figure 19.- Concluded.



(a) $\beta_{0.75R}, 55^\circ$

Figure 20.- The effect of power on the longitudinal characteristics of the model. $M, 0.85$.

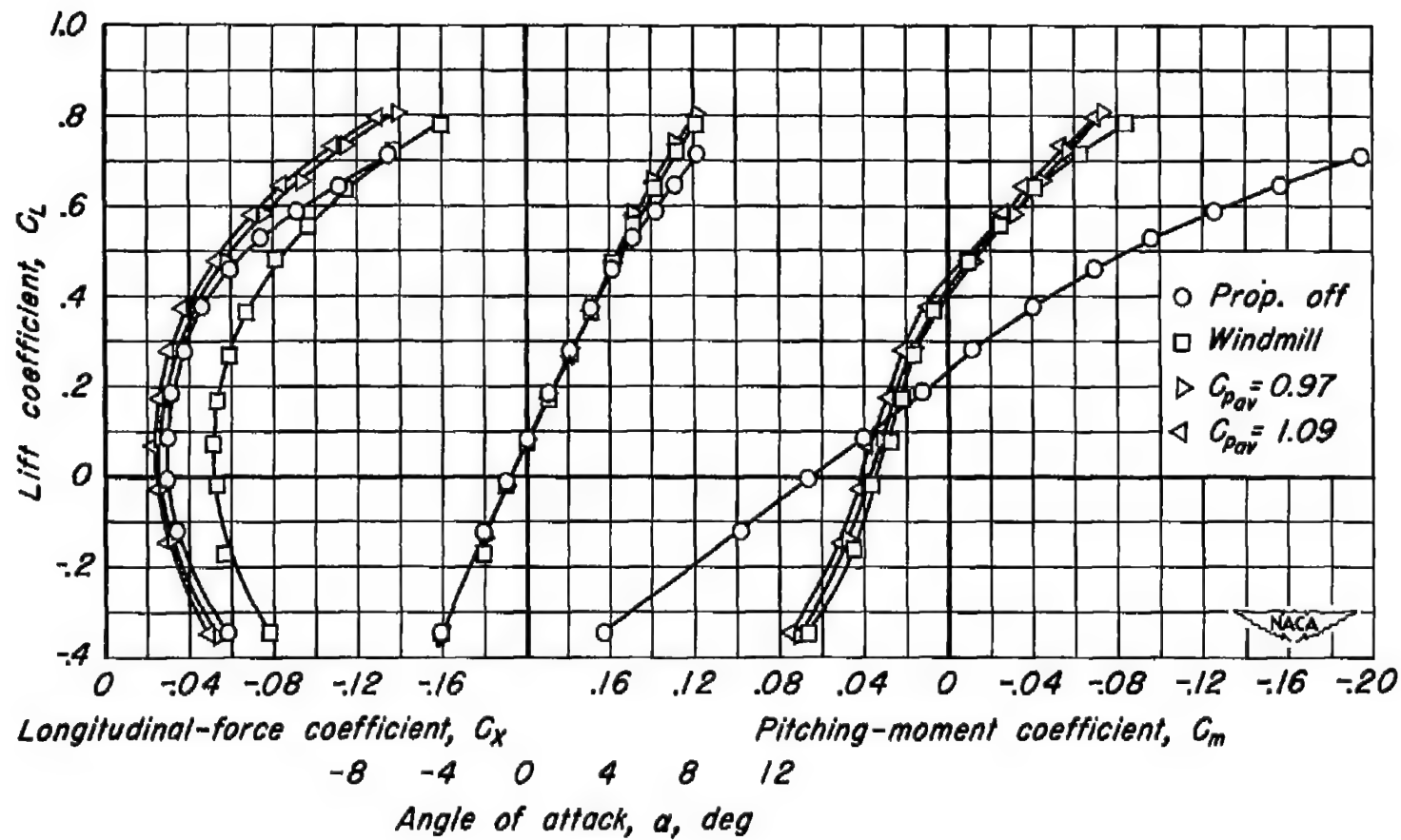
(b) $\beta_{0.75R}, 60^\circ$

Figure 20.- Concluded.

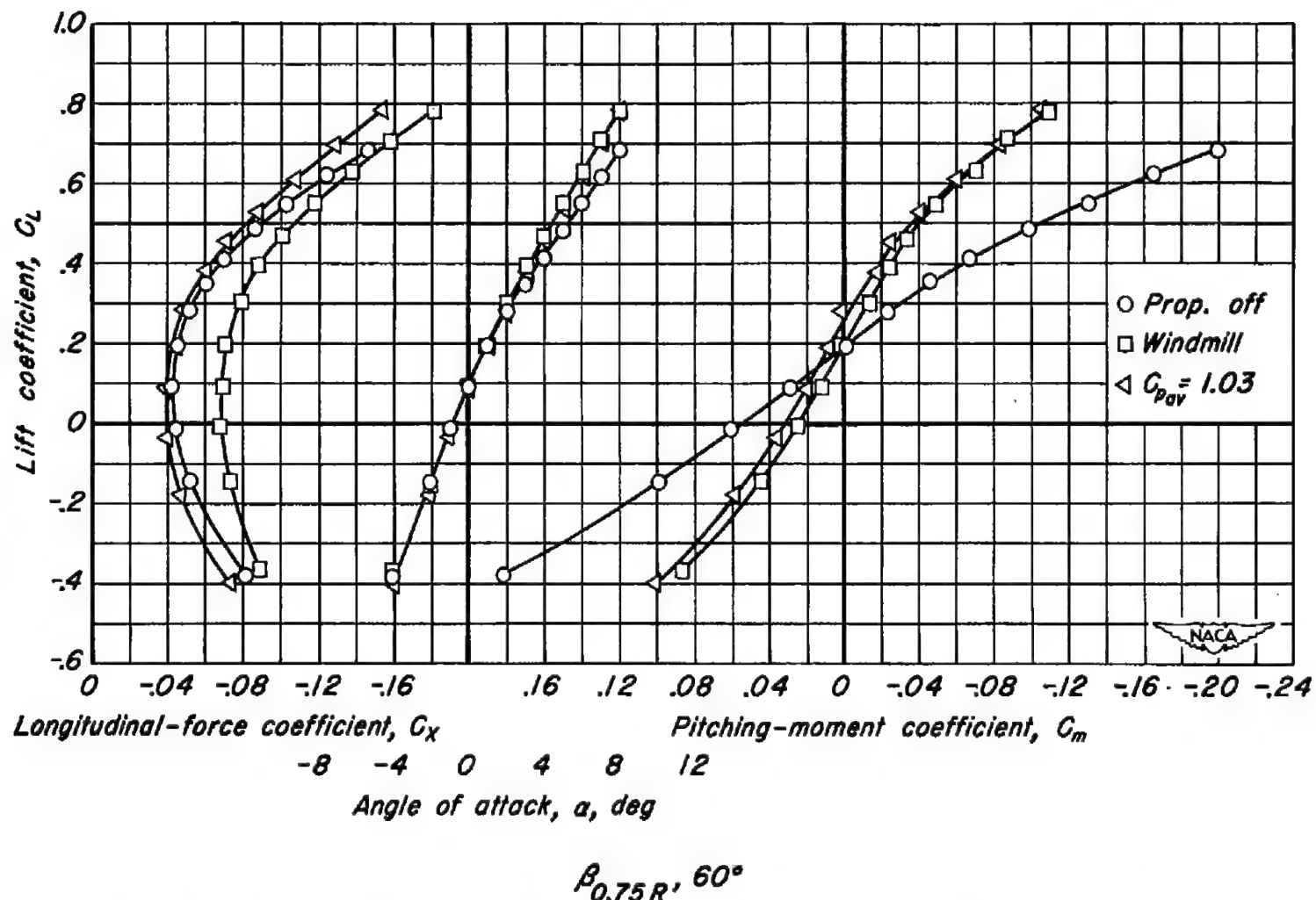


Figure 21.— The effect of power on the longitudinal characteristics of the model. $M, 0.90$.

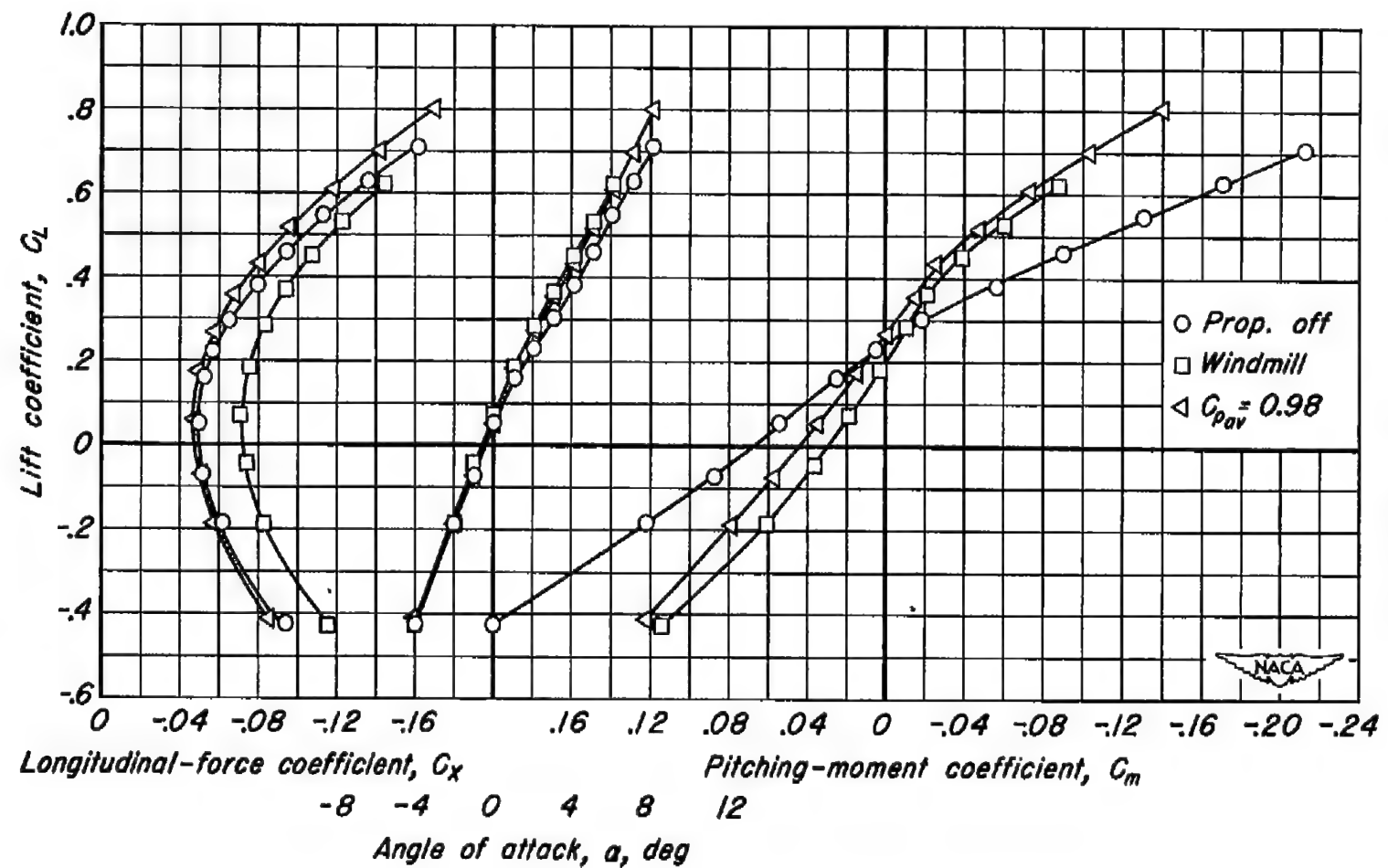


Figure 22.—The effect of power on the longitudinal characteristics of the model. $M, 0.92$.

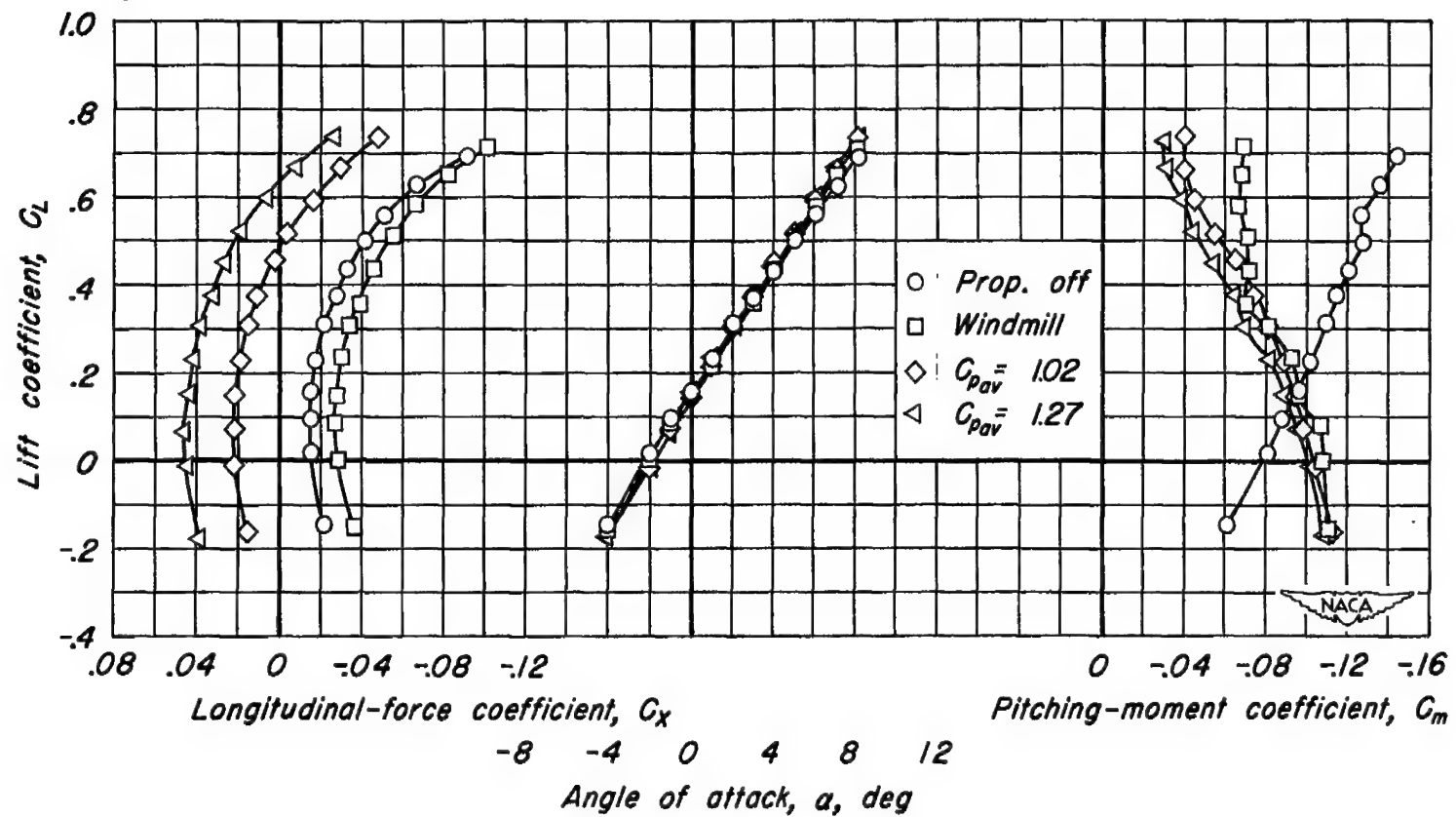
(a) $M, 0.50$

Figure 23.- The effect of power on the longitudinal characteristics of the model, tail off.

$\beta_{0.75R}, 55^\circ$

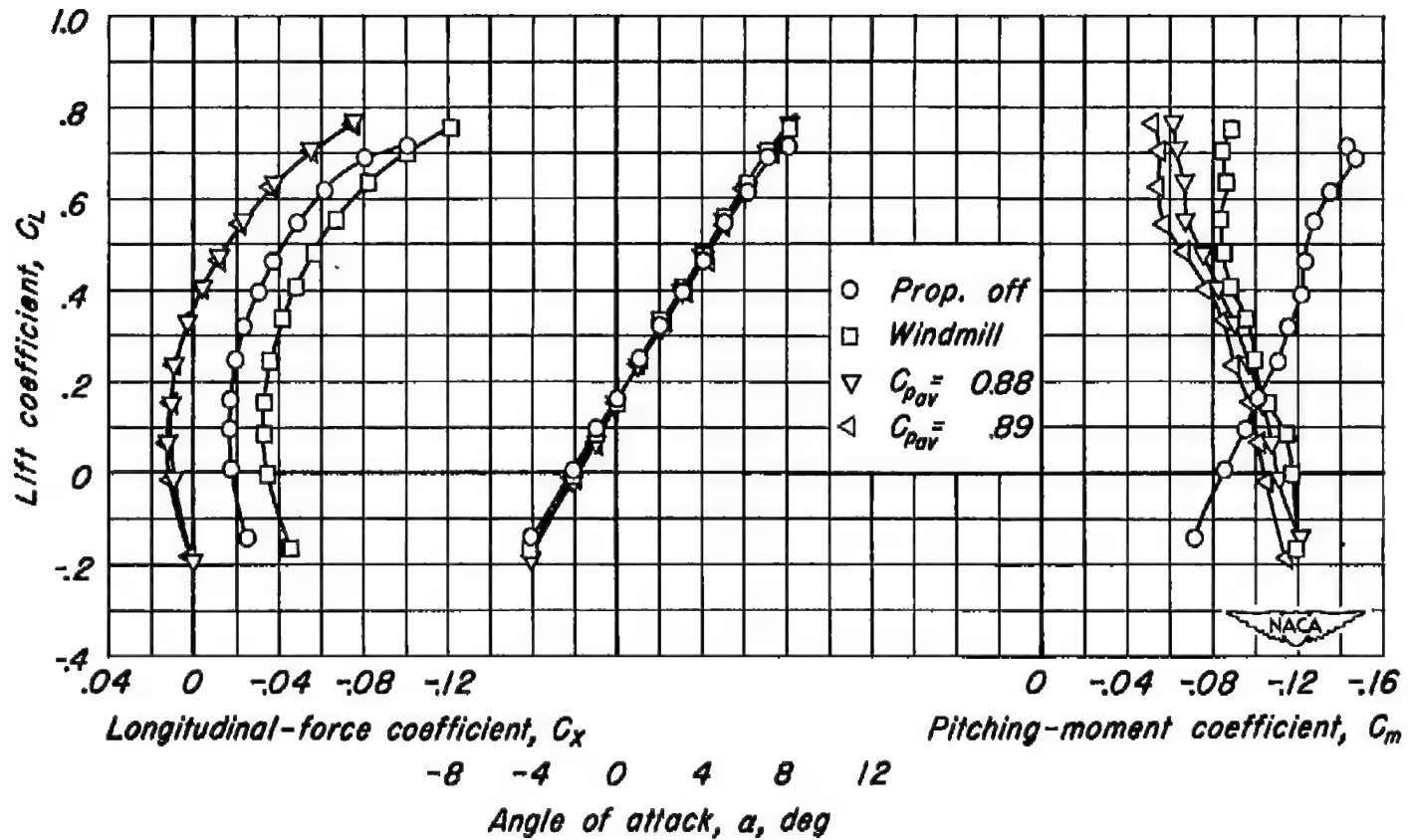
(b) $M, 0.70$

Figure 23.—Continued.

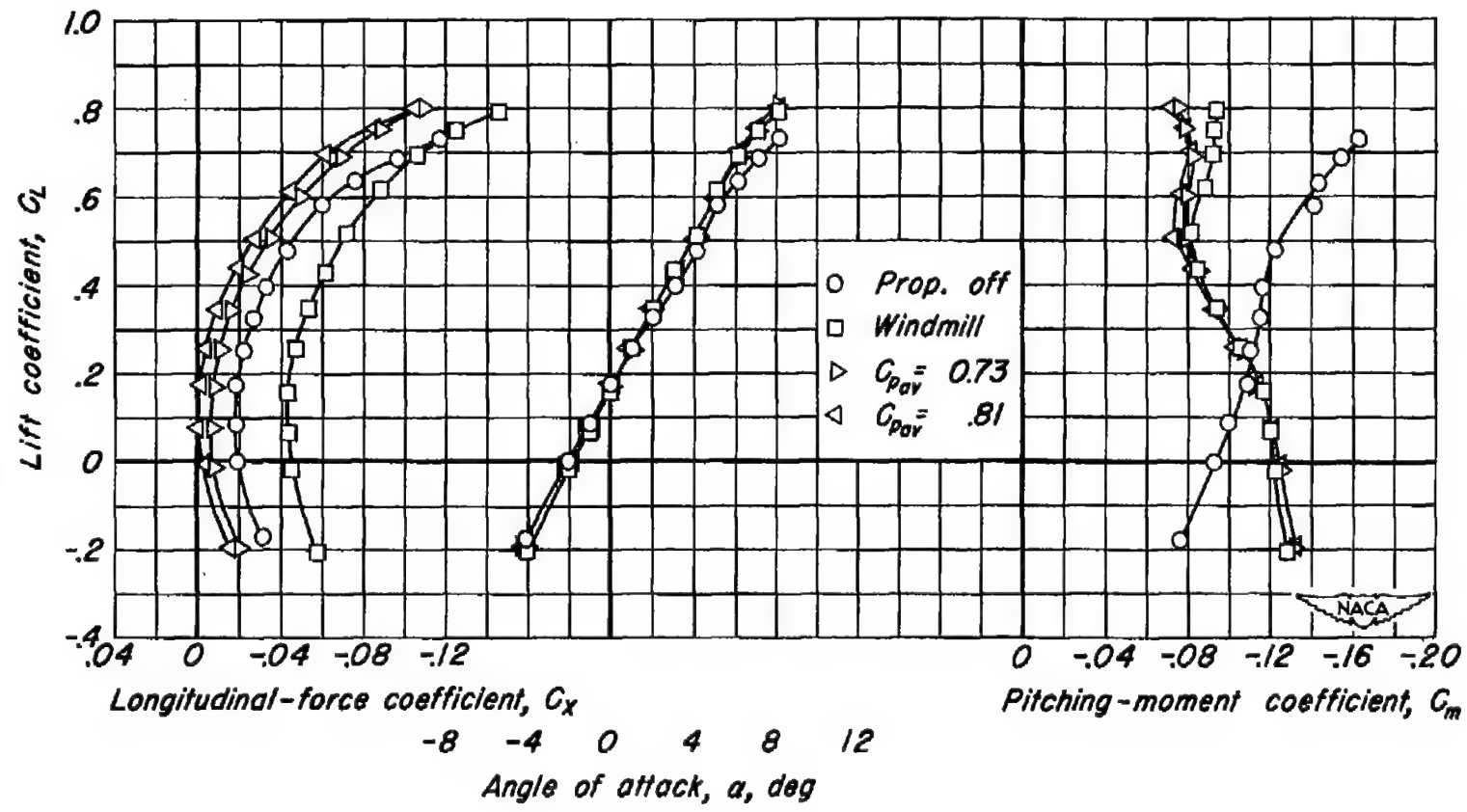
(d) $M, 0.80$

Figure 23.—Continued.

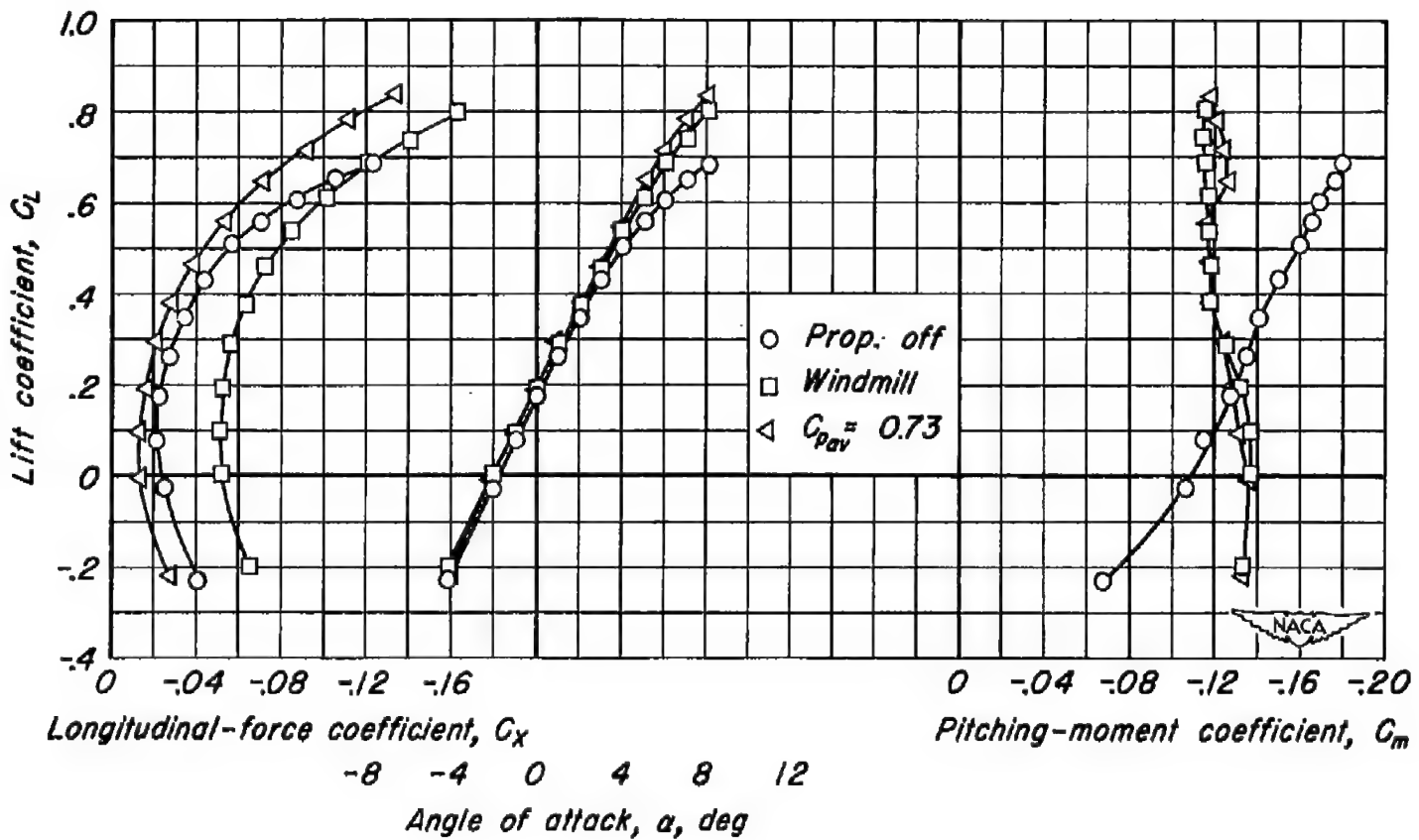
(d) $M, 0.85$

Figure 23.- Continued.

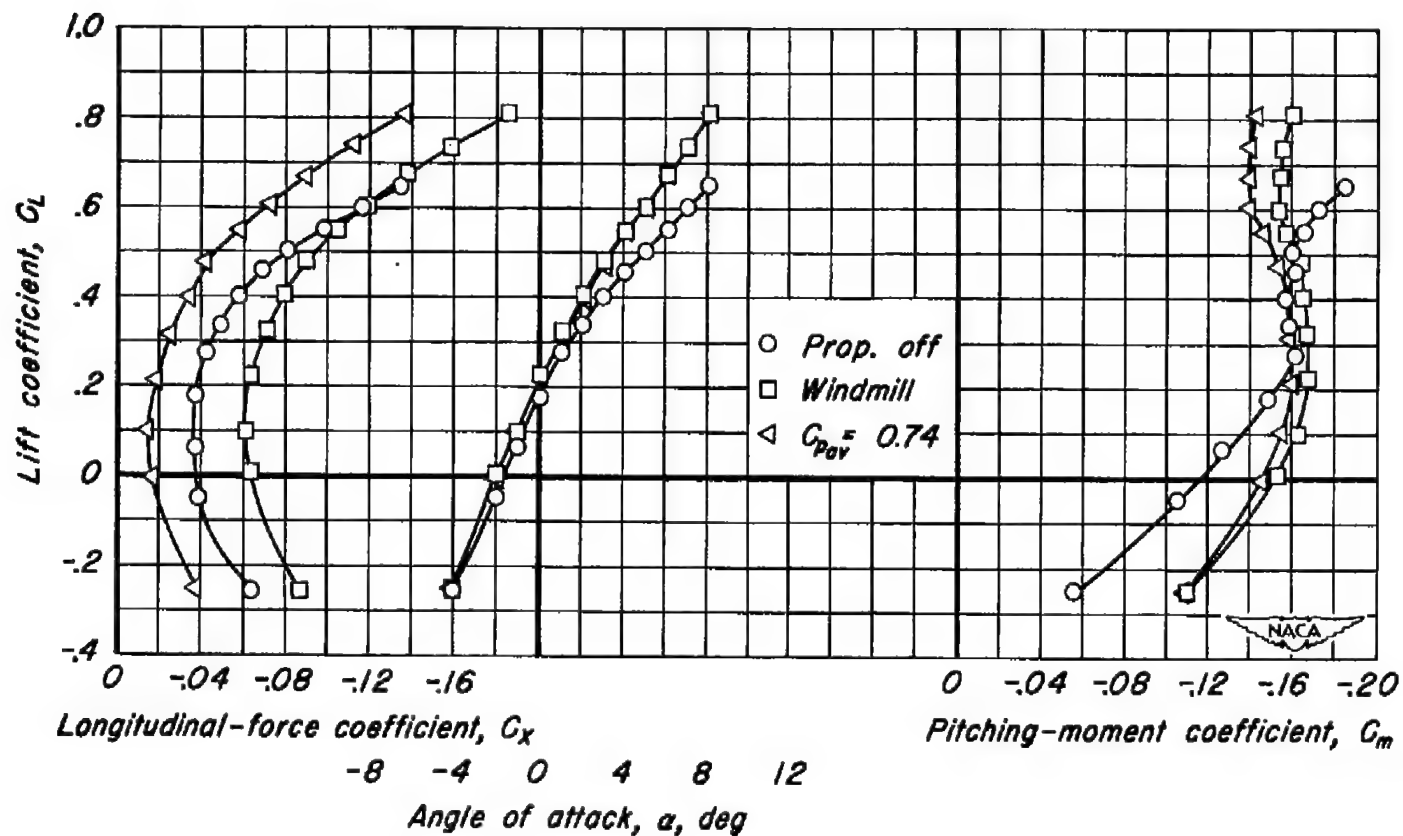
(e) $M, 0.90$

Figure 23.—Continued.

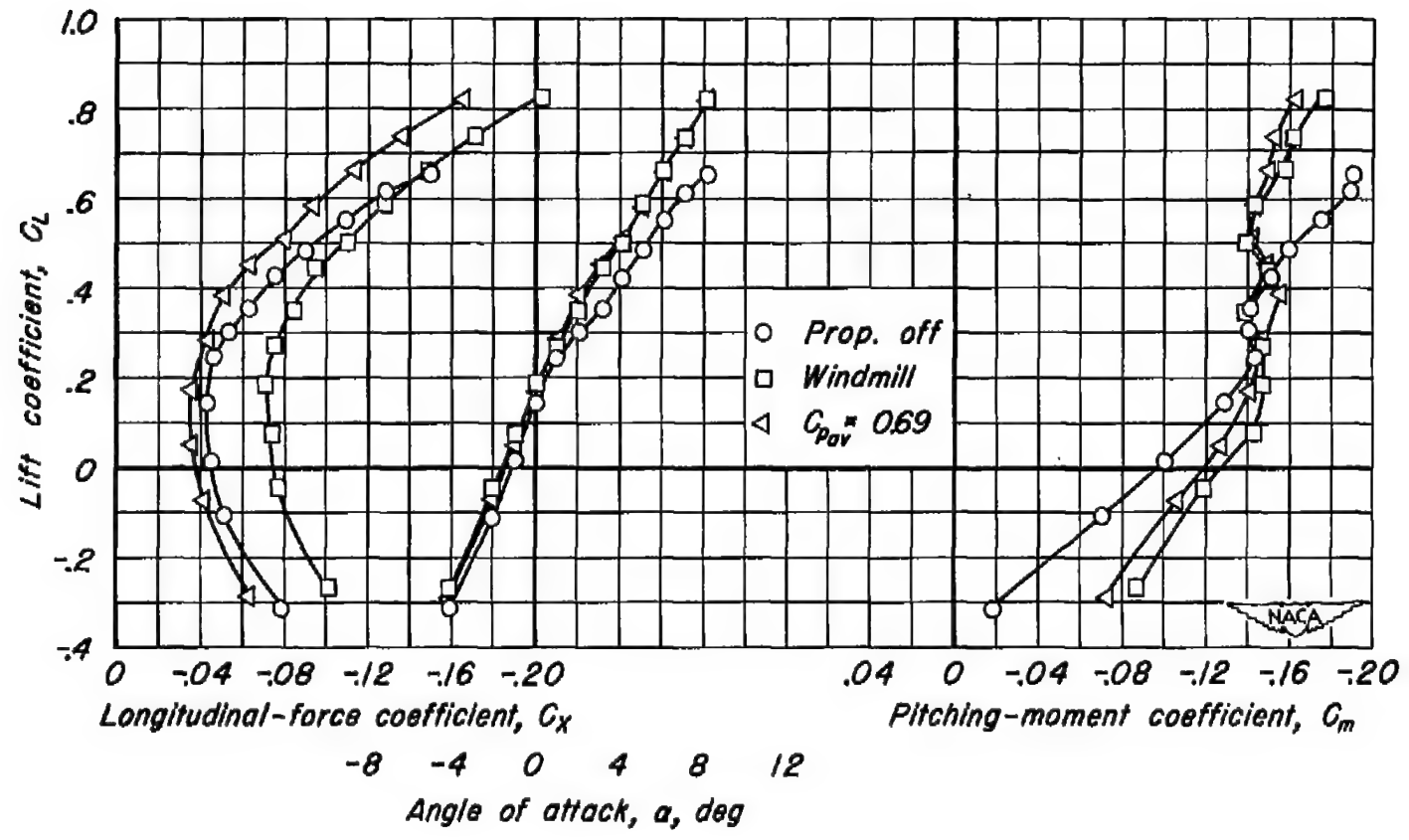
(f) $M, 0.92$

Figure 23.— Concluded.

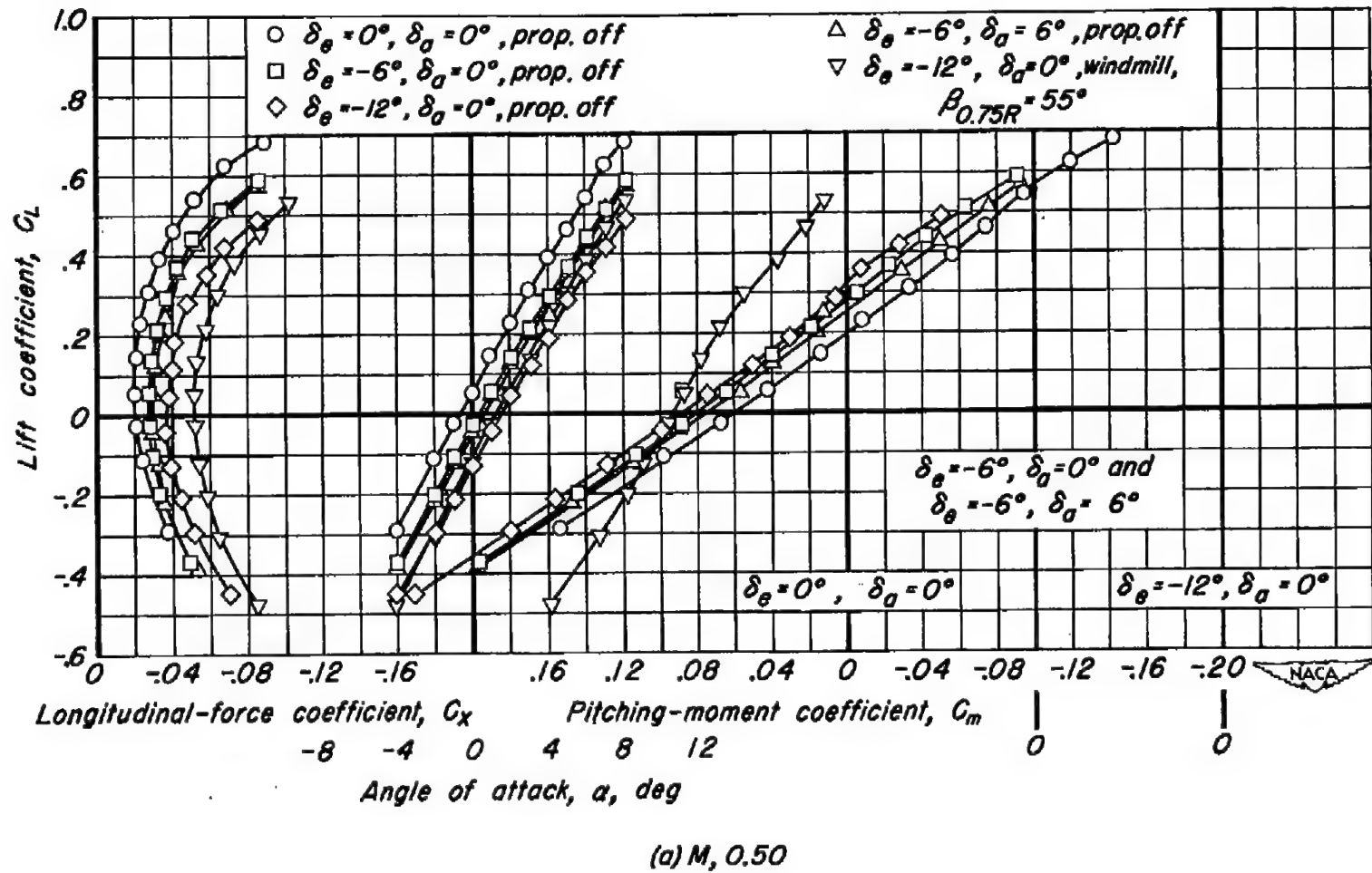
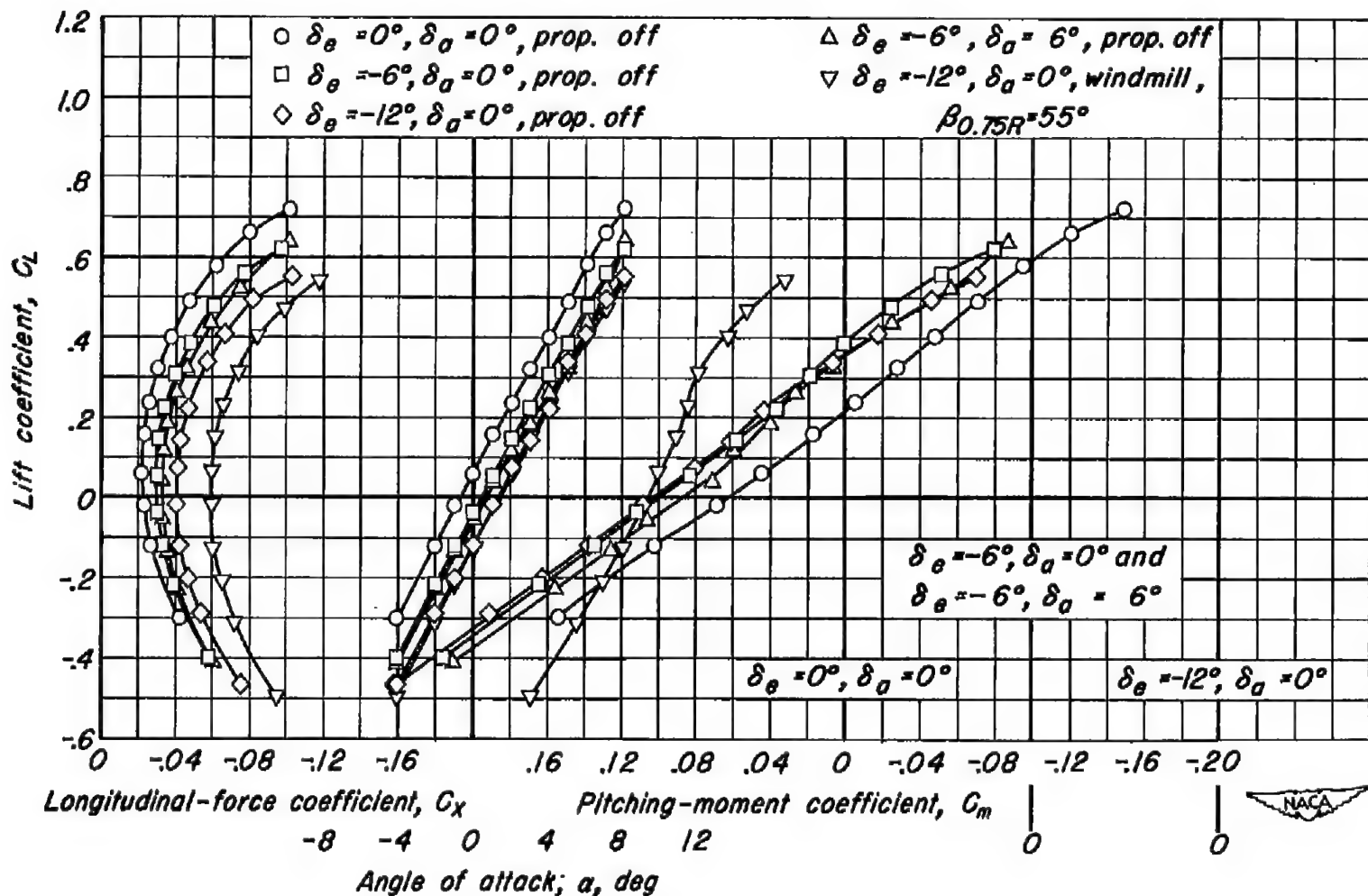


Figure 24.- Longitudinal-control characteristics of the model.



(b) $M, 0.70$
Figure 24.- Continued.

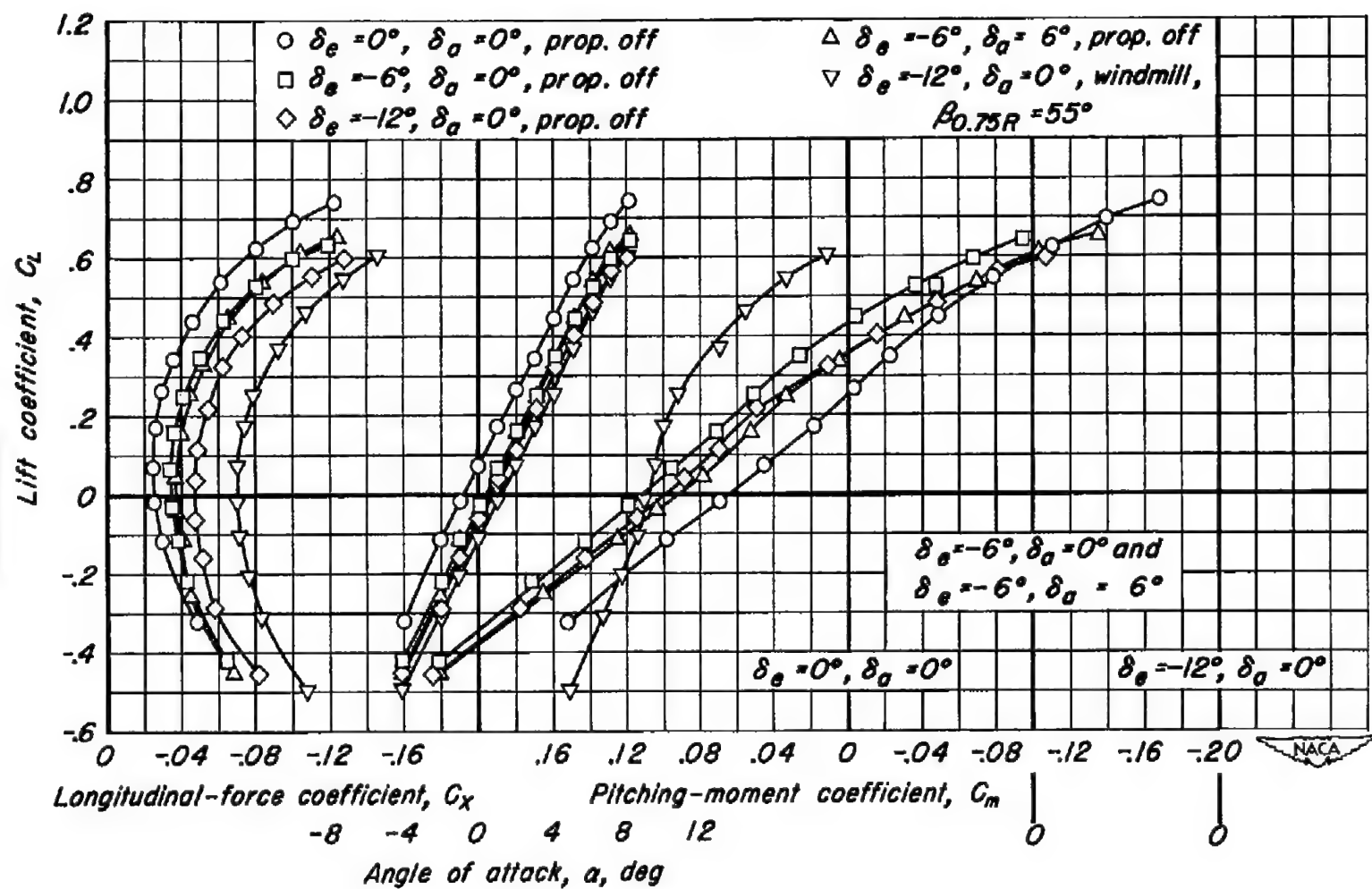
(c) $M, 0.80$

Figure 24.—Continued.

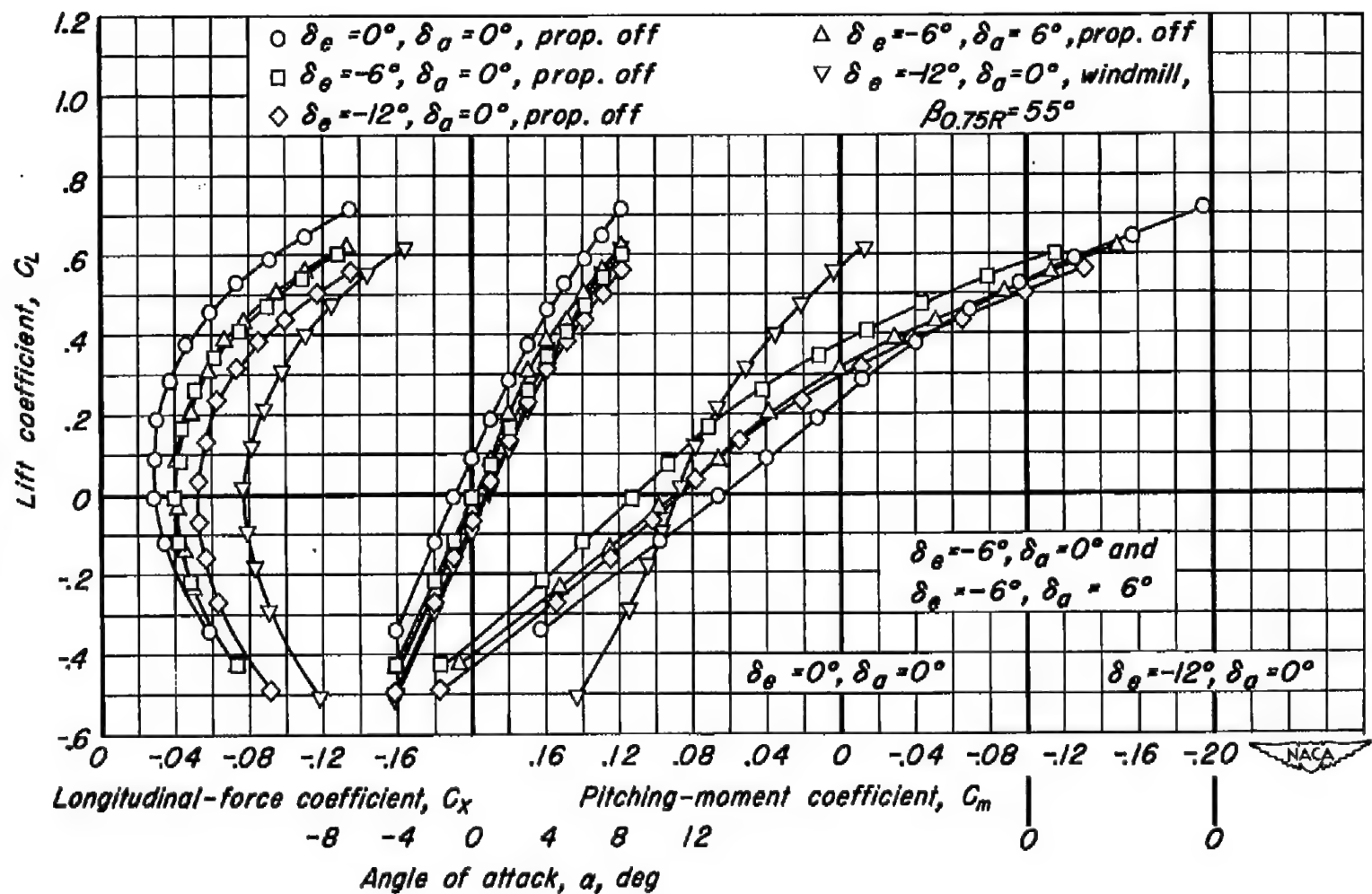
(d) $M, 0.85$

Figure 24.- Continued.

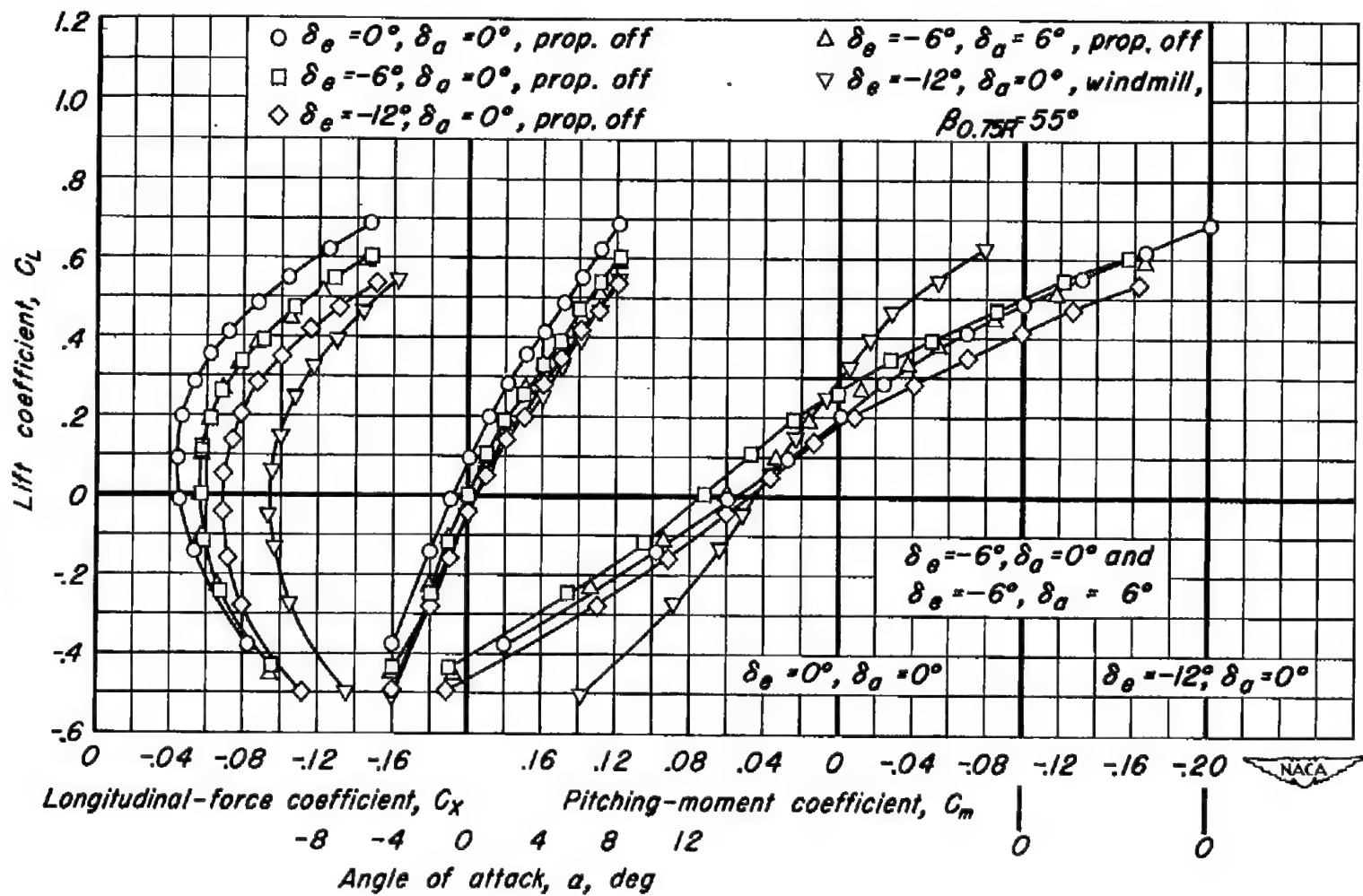
(e) $M, 0.90$

Figure 24. — Continued.

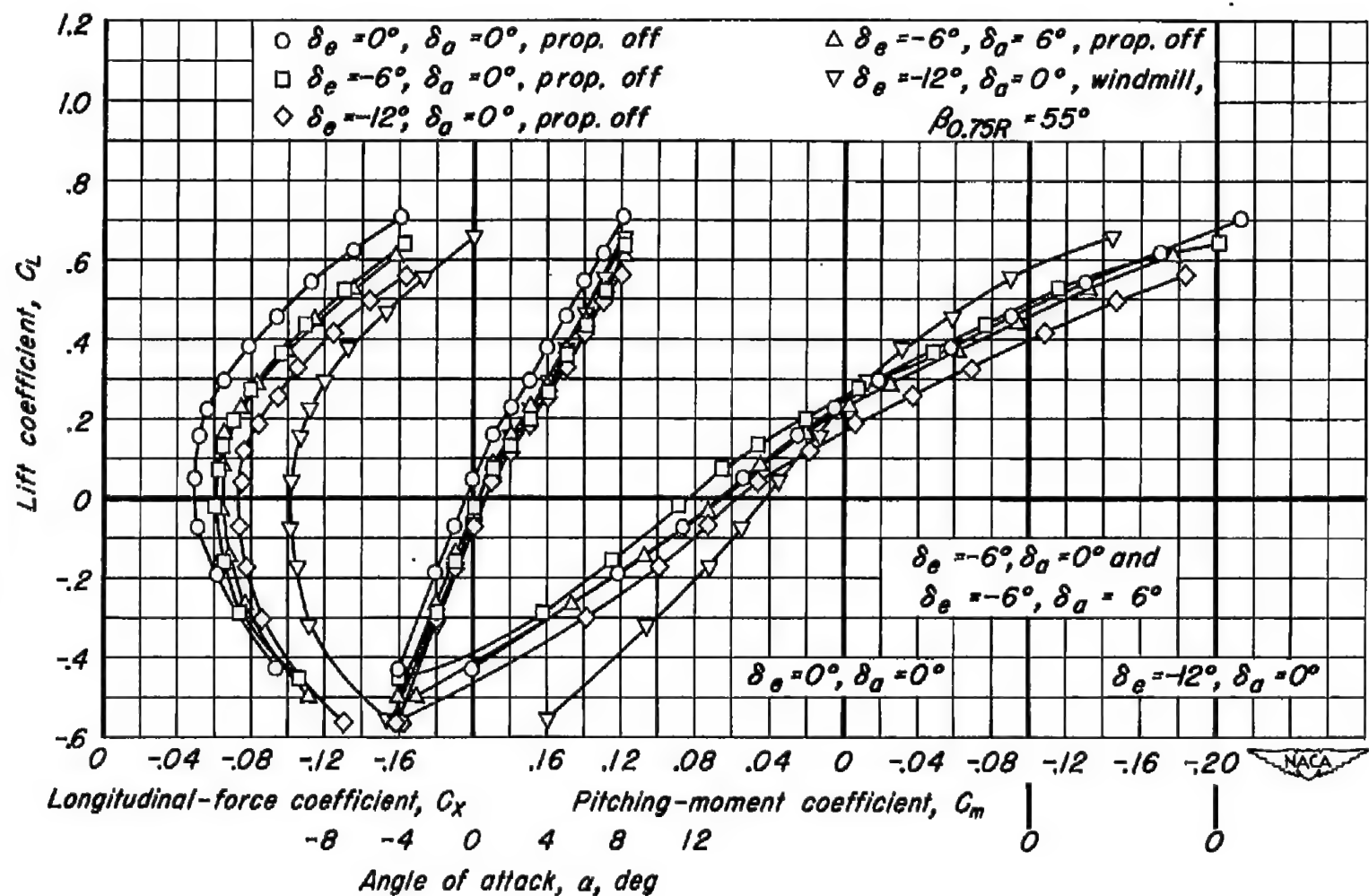
(f) $M, 0.92$

Figure 24.— Concluded.

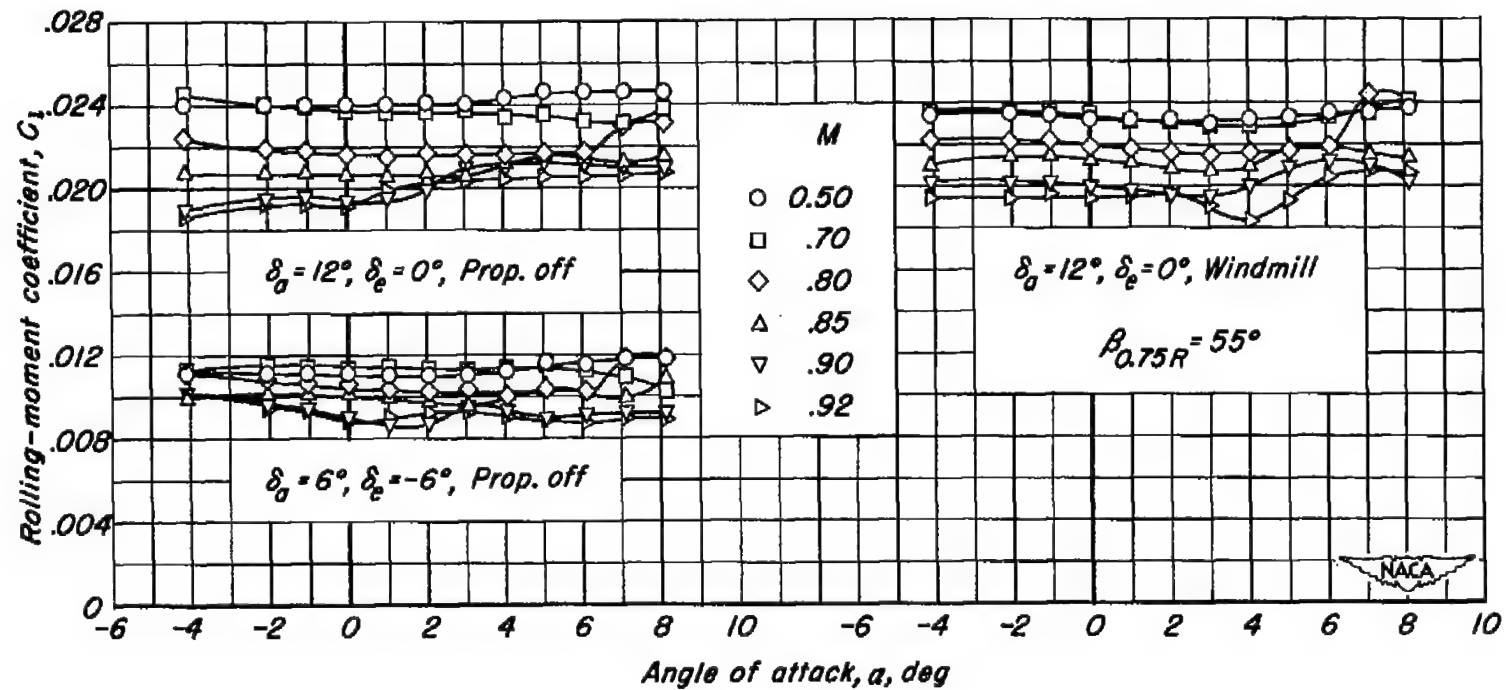


Figure 25.—Roll characteristics of the model. Angle of yaw, 0°.

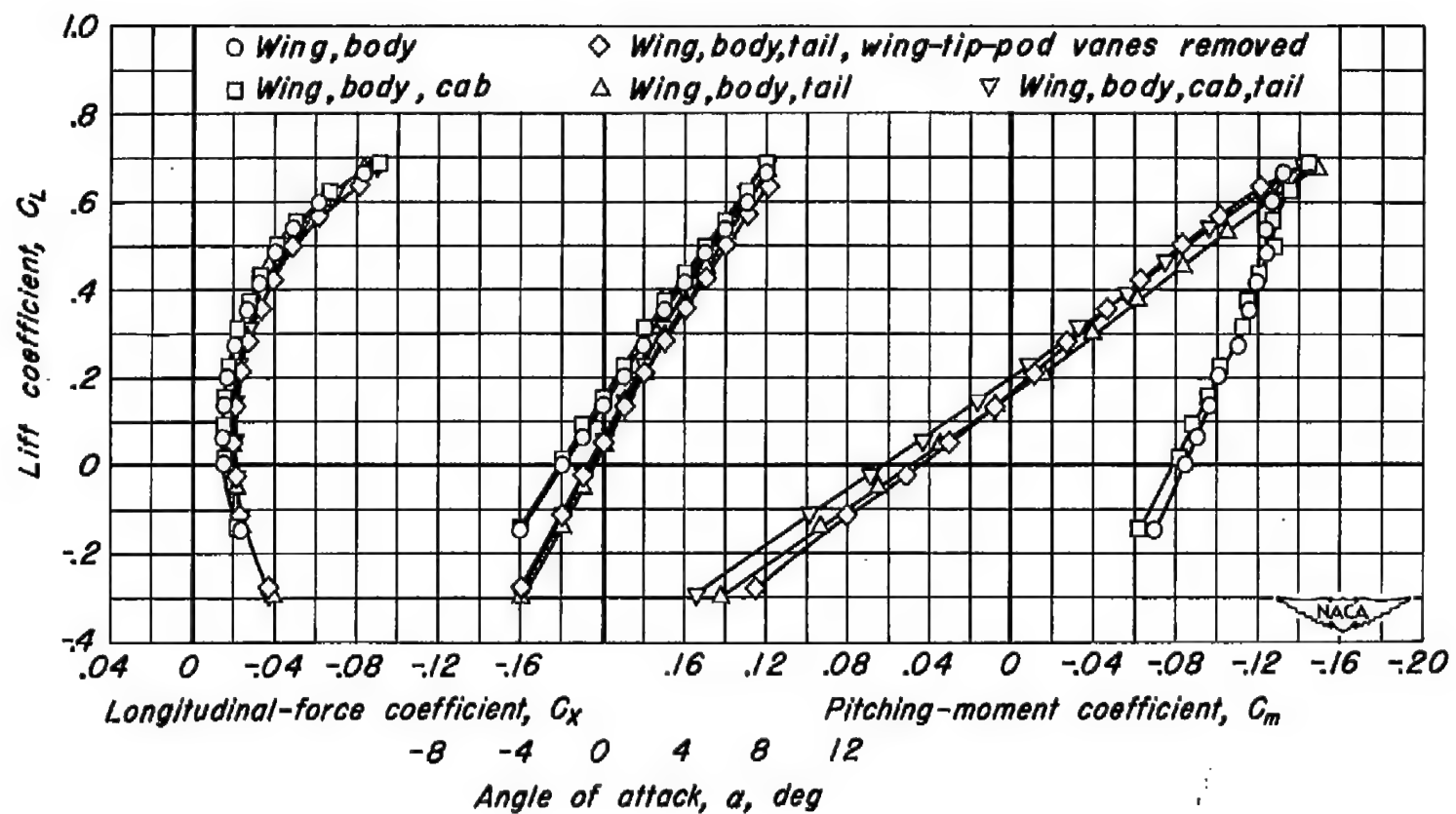


Figure 26.— The longitudinal characteristics of several combinations of model components.
Propeller removed.

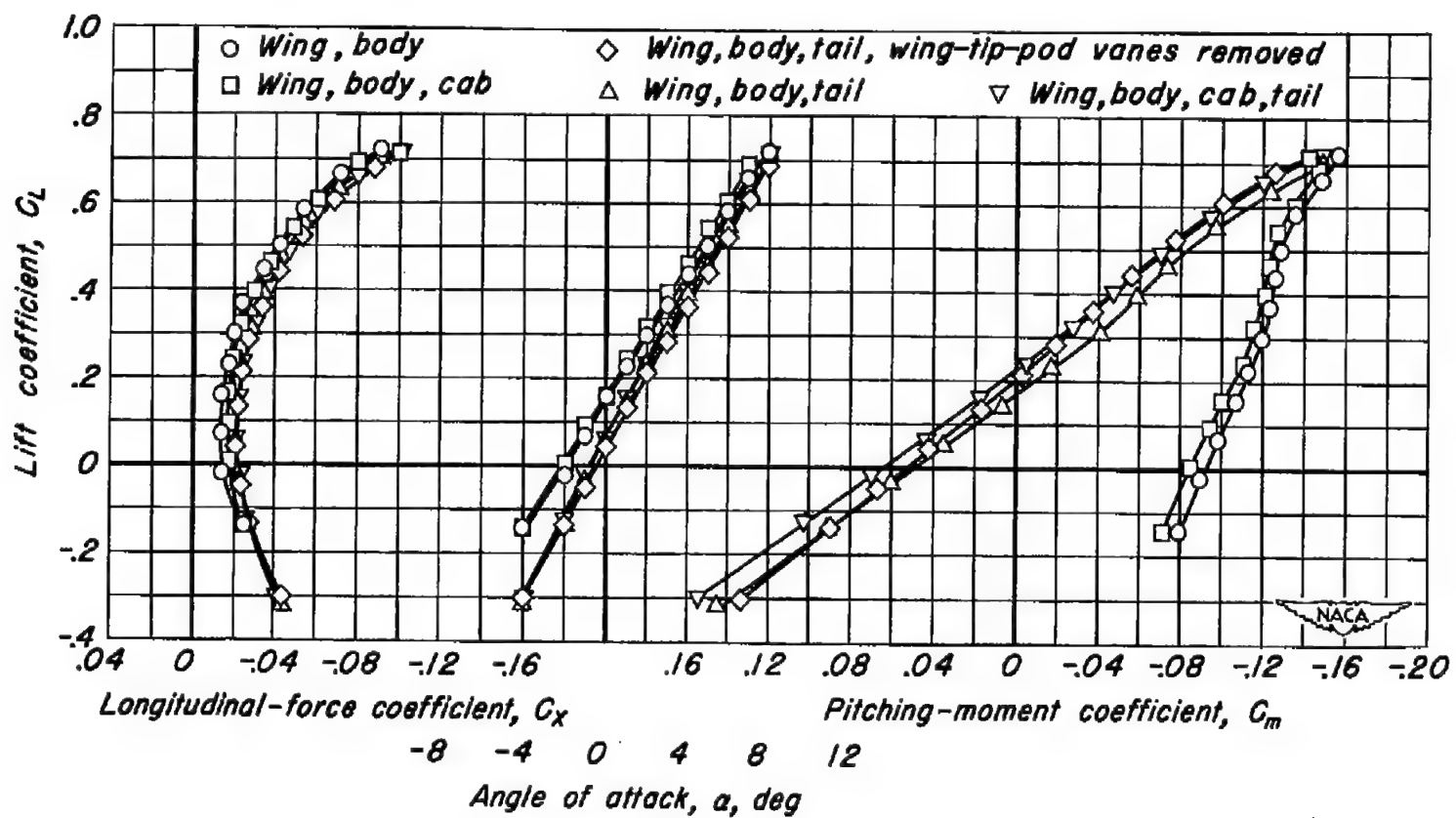
(b) $M = 0.70$

Figure 26.- Continued.

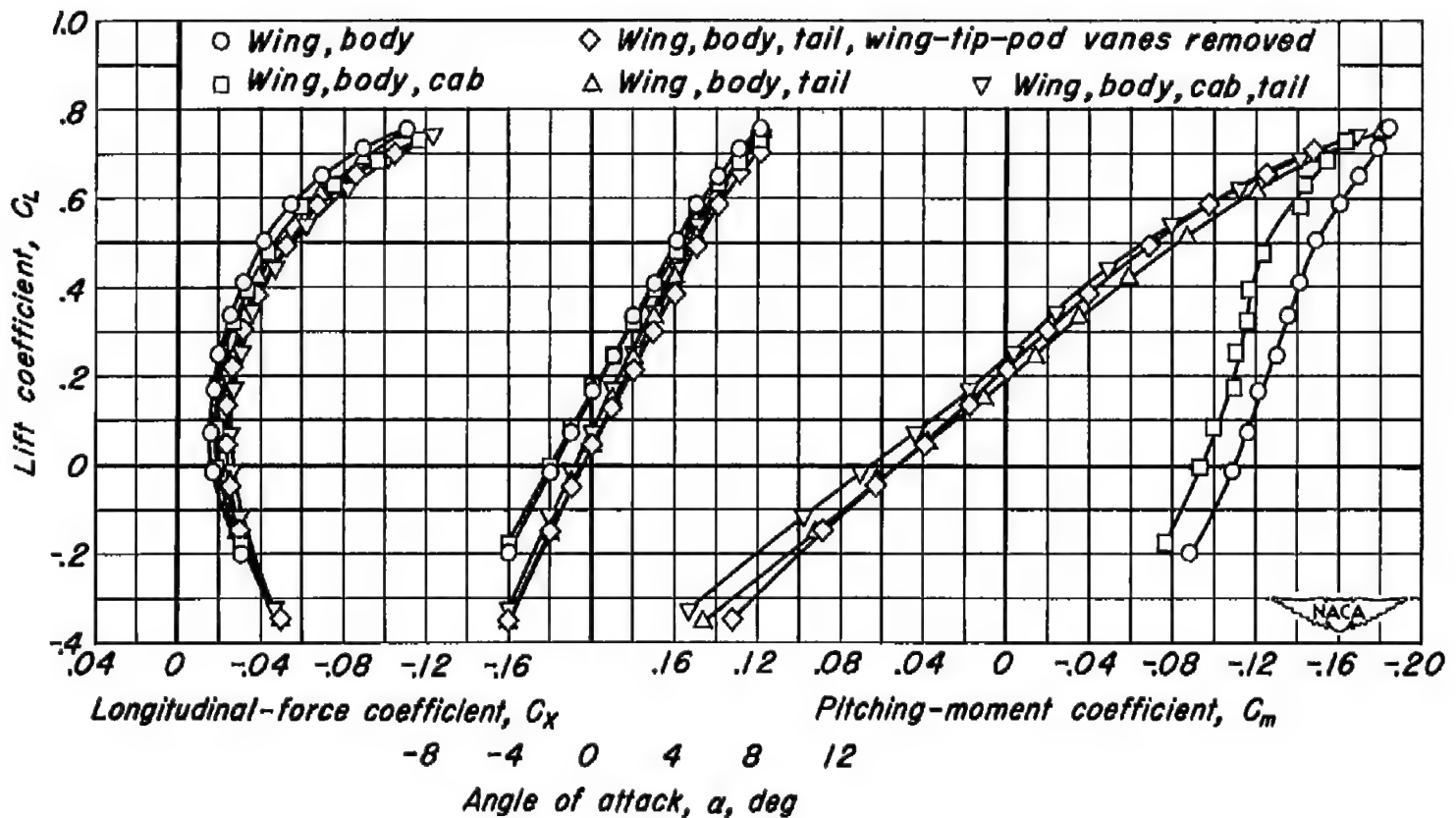


Figure 26.—Continued.

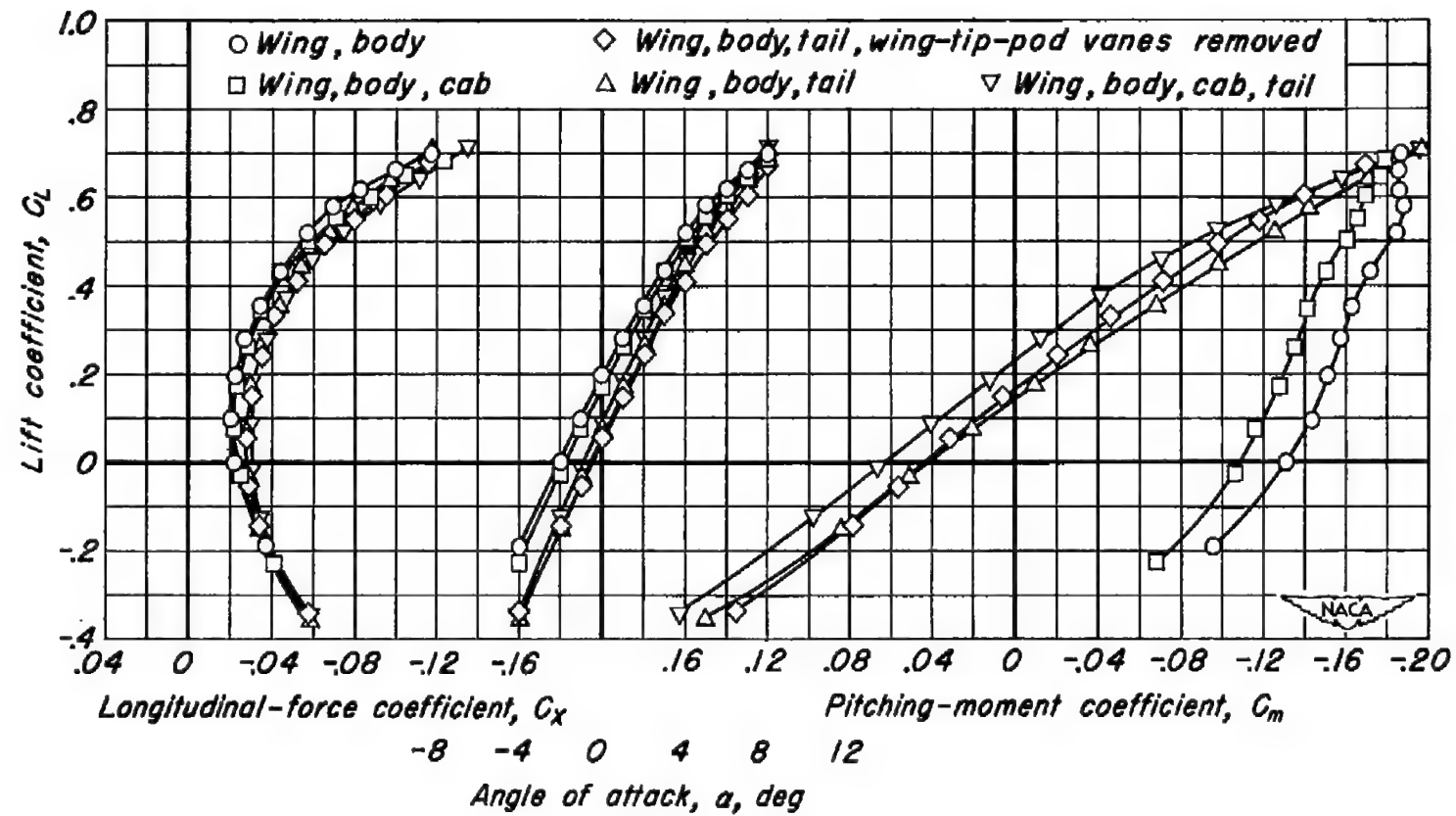
(d) $M, 0.85$

Figure 26.- Continued.

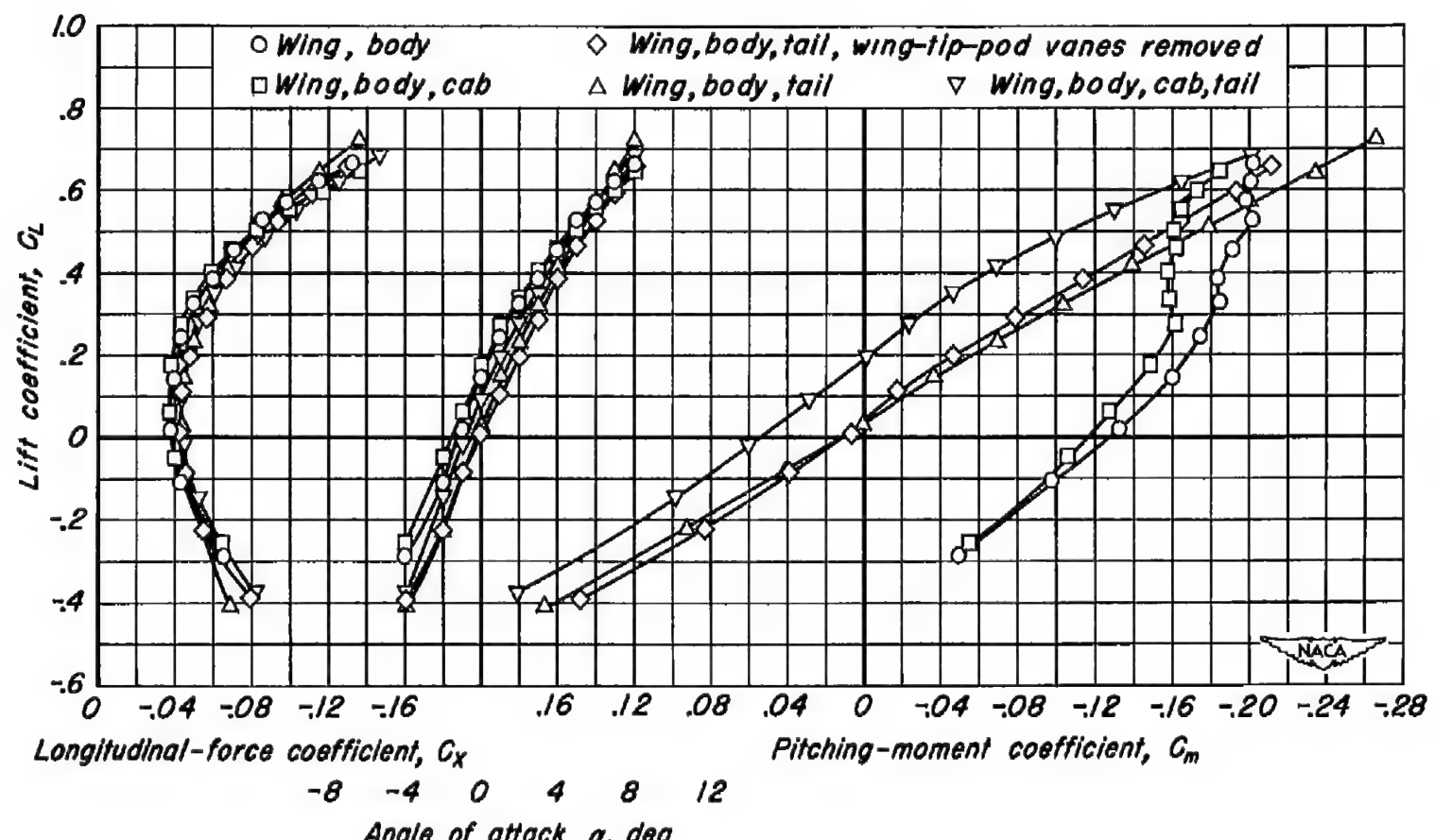
(a) $M, 0.90$

Figure 26.—Continued.

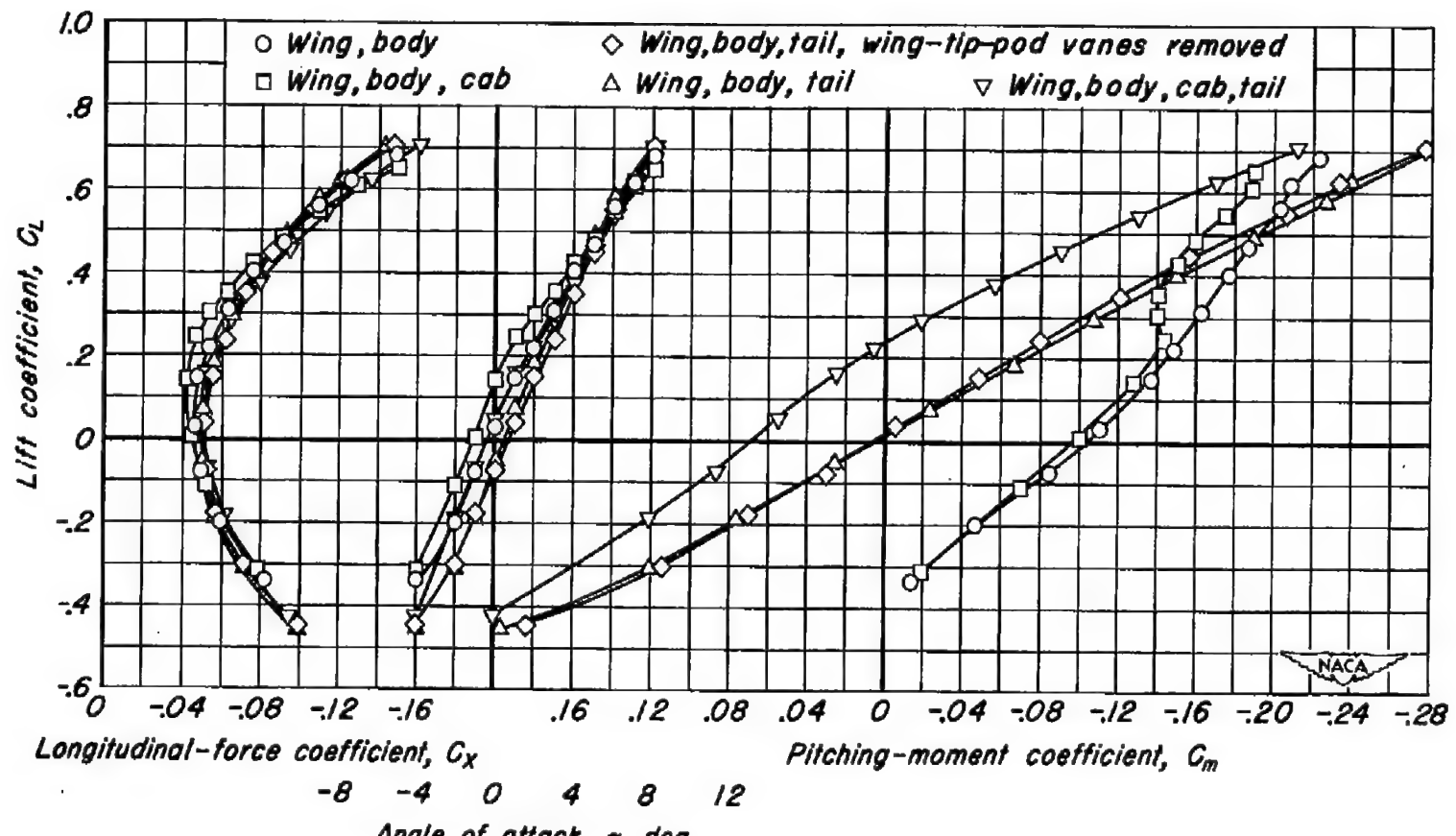
(f) $M, 0.92$

Figure 26.— Concluded.

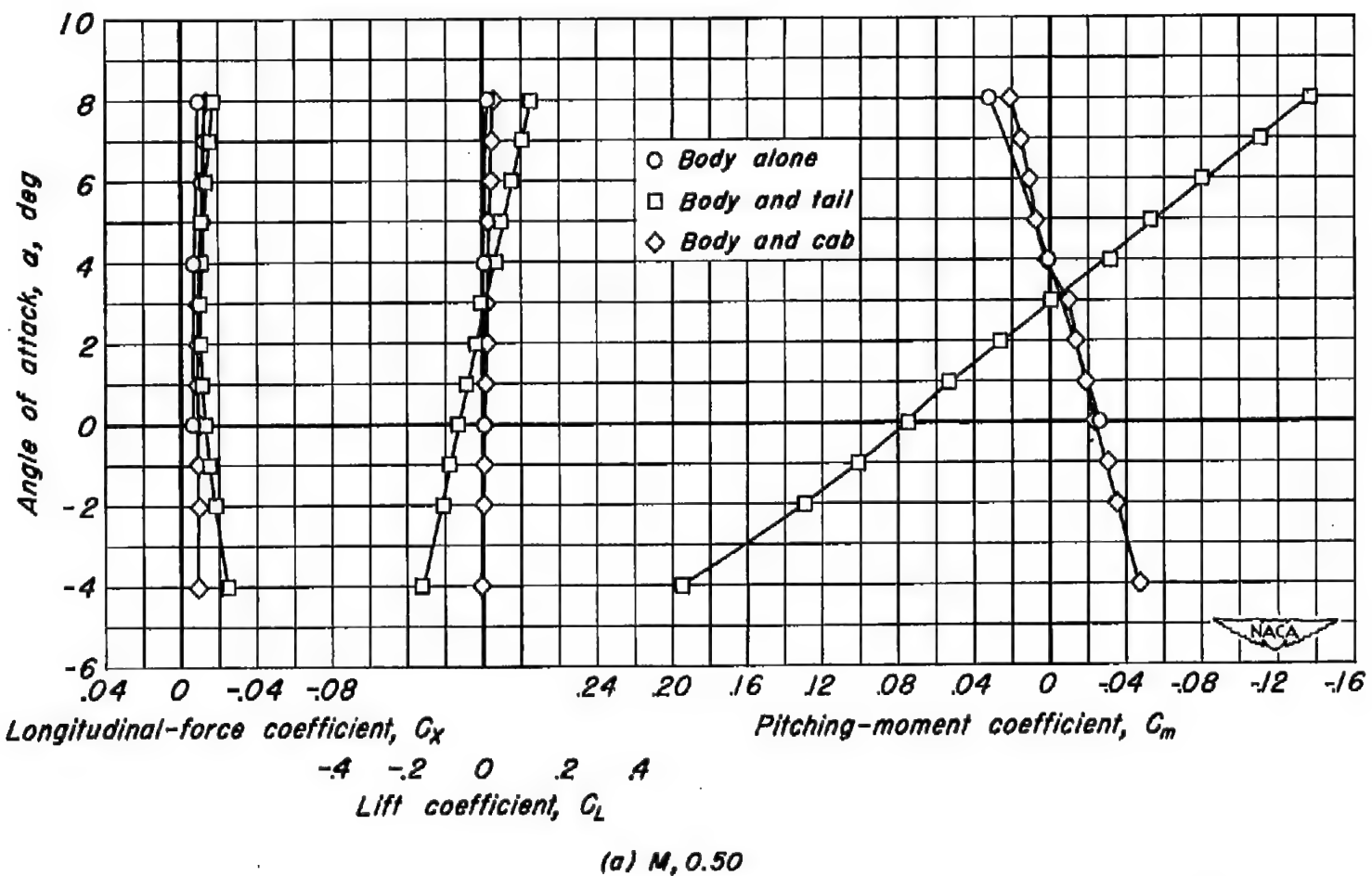


Figure 27.- The longitudinal characteristics of the body alone, the body and tail, and the body and cab. Propeller removed.

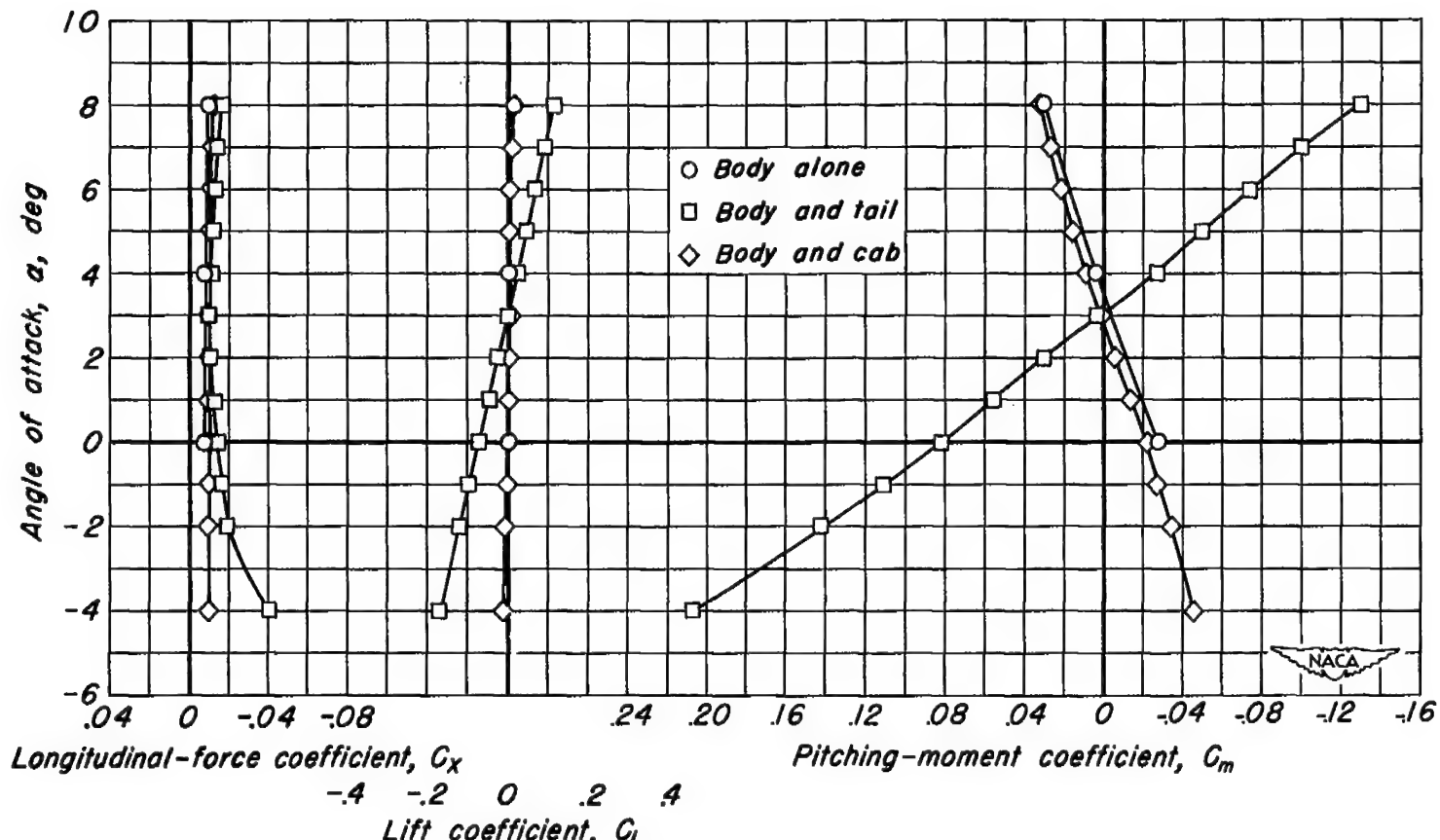
(b) $M = 0.70$

Figure 27. – Continued.

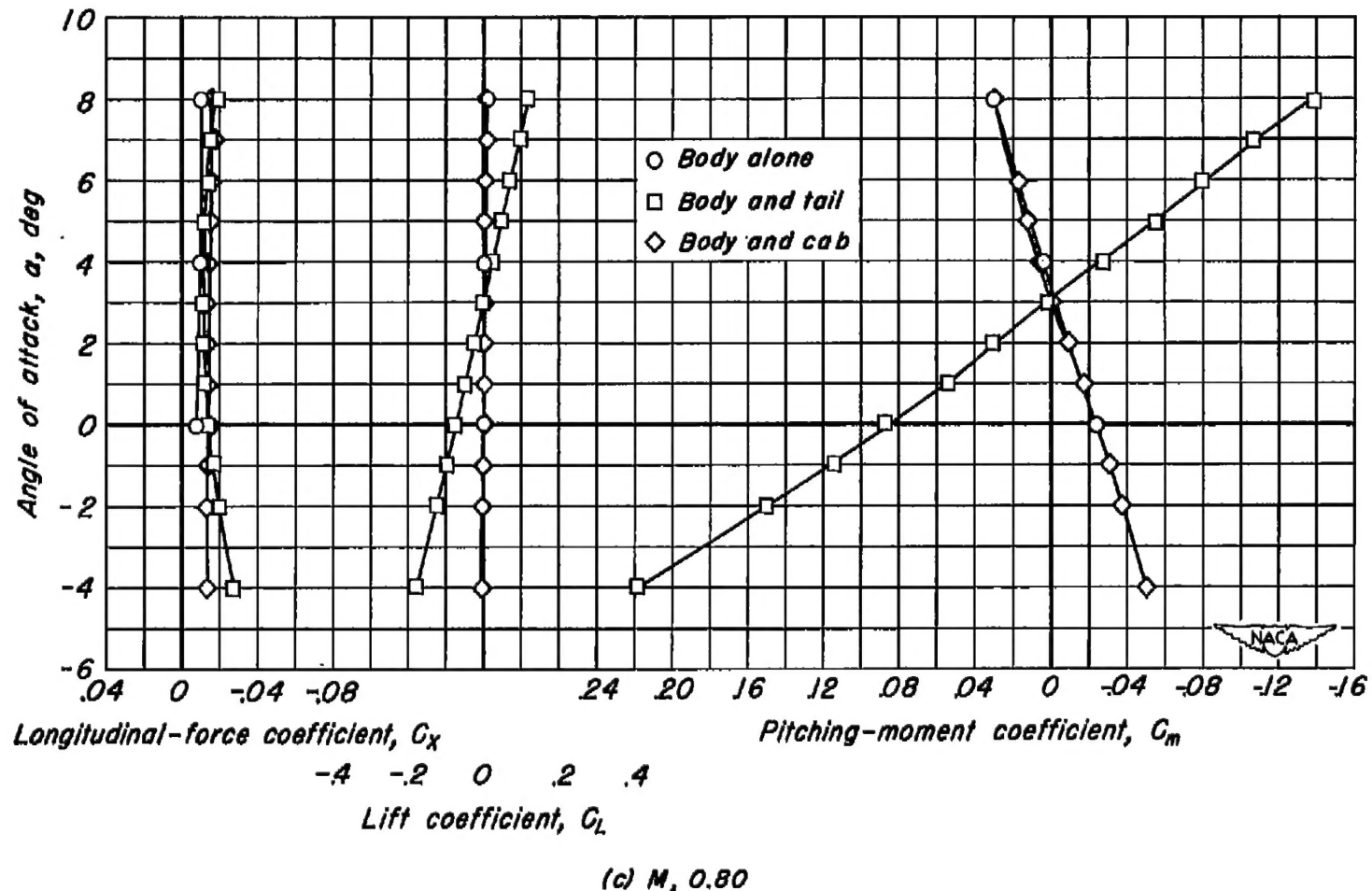


Figure 27. — Continued.

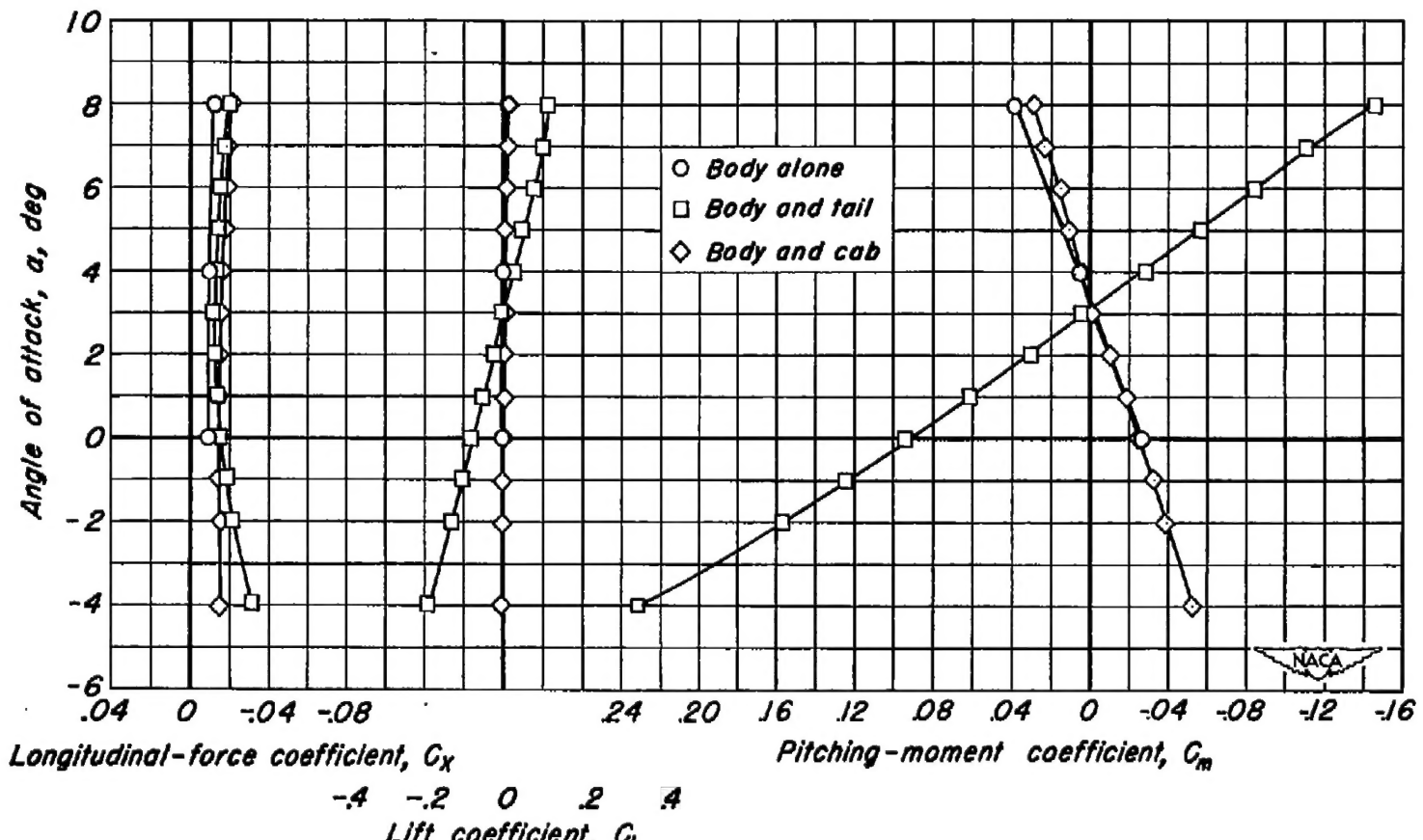
(d) $M = 0.85$

Figure 27.- Continued.

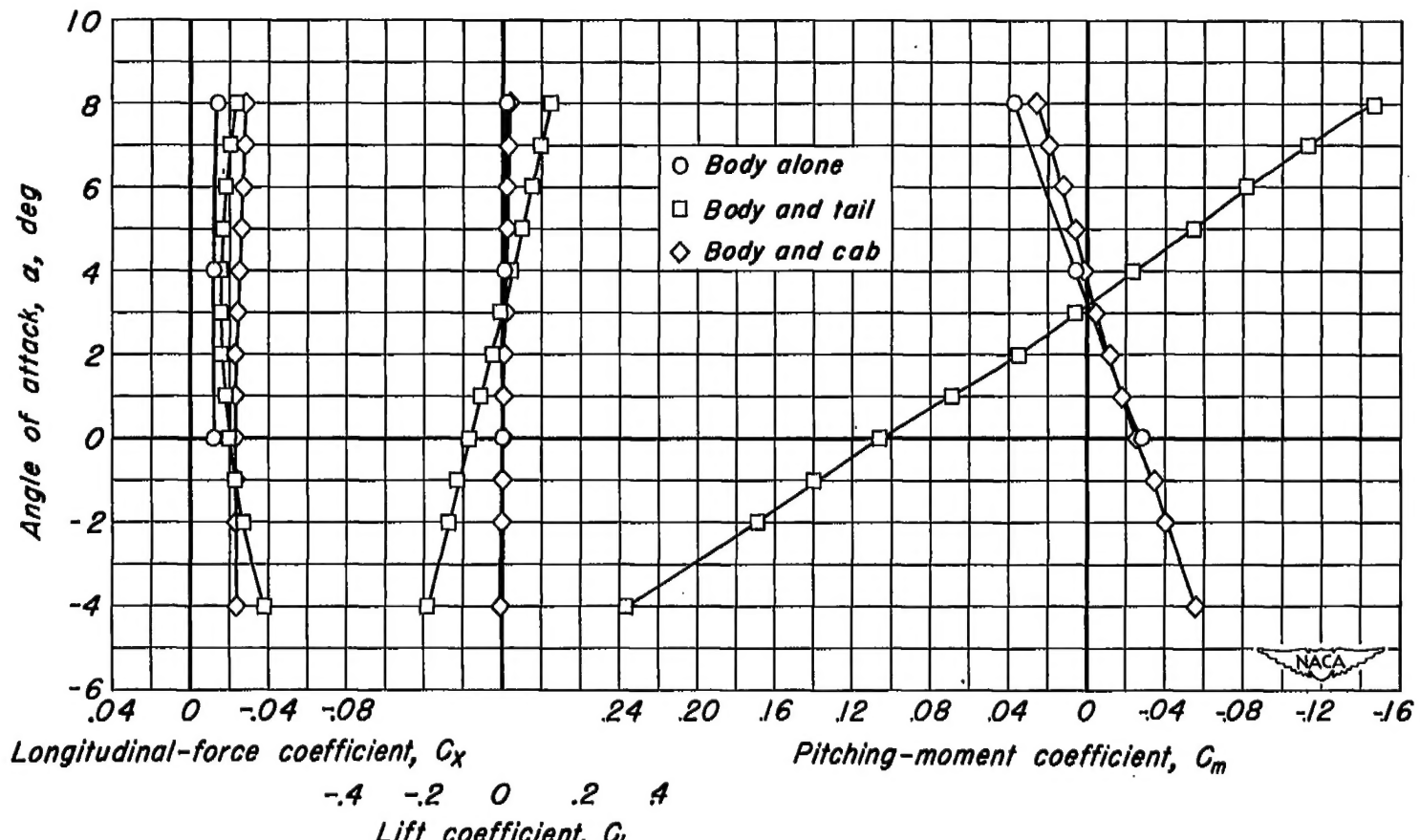
(e) $M, 0.90$

Figure 27.—Continued.

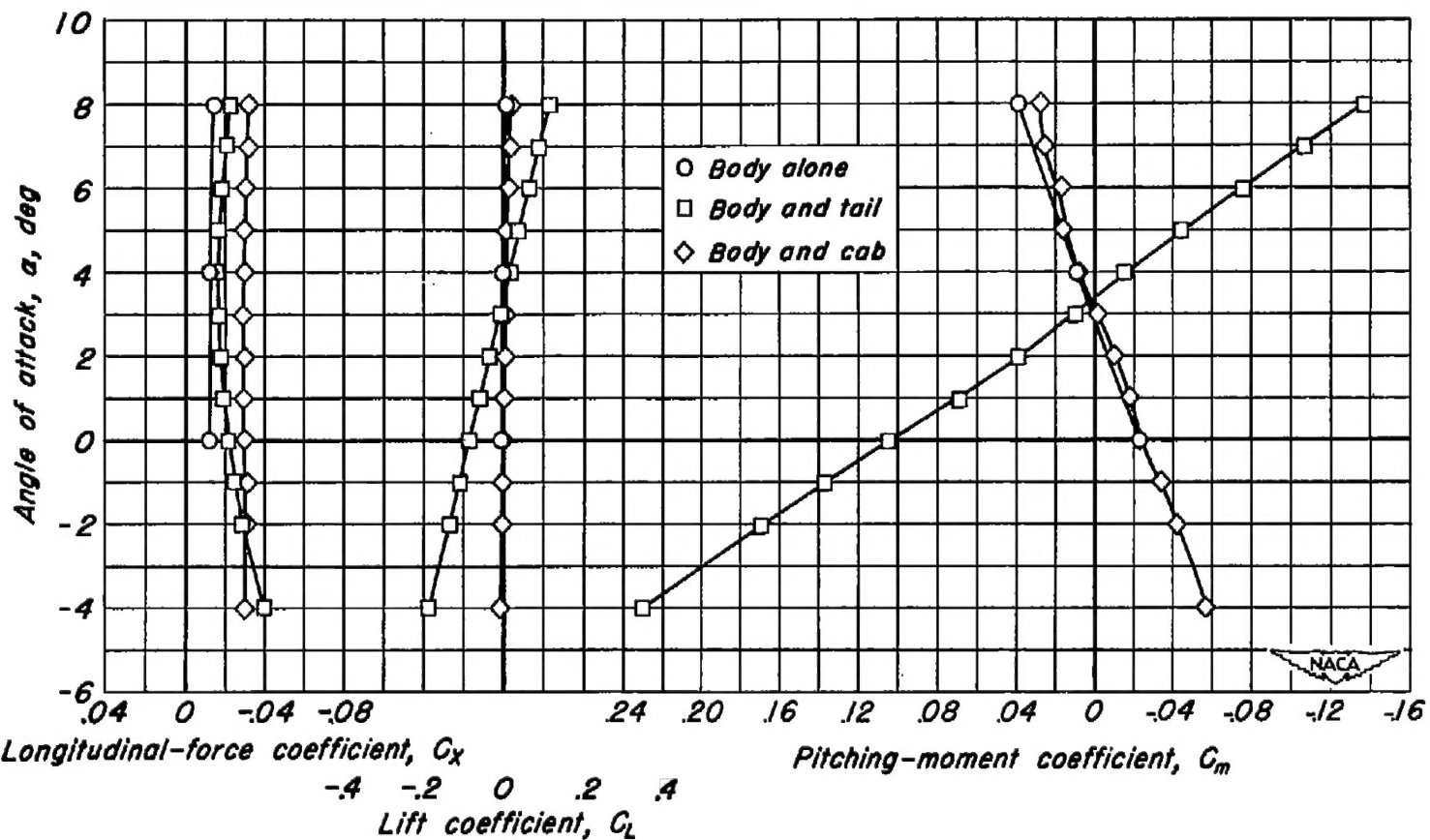
(f) $M = 0.92$

Figure 27.— Concluded.